FINAL REPORT

# DEVELOP METHODOLOGIES/PROTOCOLS TO ASSESS CRACKING POTENTIAL OF ASPHALT MIXTURES USING ACCELERATED PAVEMENT TESTING

Contract No.: BD545-49

UF Project No.: 00051675

Submitted to:

Florida Department of Transportation
605 Suwannee Street
Tallahassee, FL 32399

By


| | |
|---|---|
| Principal Investigator: | Reynaldo Roque, Professor |
| Researchers: | Alvaro Guarin, Guangming Wang,<br>Jian Zou and Helge Mork |

Department of Civil and Coastal Engineering
College of Engineering
University of Florida
365 Weil Hall
PO Box 116580
Gainesville, Florida 32611-6580
(352) 392-7575, extension 1458


UNIVERSITY OF
FLORIDA

September, 2007

## DISCLAIMER

"The opinions, findings and conclusions expressed in this publication are those of the authors and not necessarily those of the Florida Department of Transportation or the U.S. Department of Transportation.

Prepared in cooperation with the State of Florida Department of Transportation and the U.S. Department of Transportation."

# SI* (MODERN METRIC) CONVERSION FACTORS

## APPROXIMATE CONVERSIONS TO SI UNITS

| Symbol | When You Know | Multiply By | To Find | Symbol |
|---|---|---|---|---|
| | **LENGTH** | | | |
| in | inches | 25.4 | millimeters | mm |
| ft | feet | 0.305 | meters | m |
| yd | yards | 0.914 | meters | m |
| mi | miles | 1.61 | kilometers | km |
| | **AREA** | | | |
| $in^2$ | square inches | 645.2 | square millimeters | $mm^2$ |
| $ft^2$ | square feet | 0.093 | square meters | $m^2$ |
| $yd^2$ | square yards | 0.836 | square meters | $m^2$ |
| ac | acres | 0.405 | hectares | ha |
| $mi^2$ | square miles | 2.59 | square kilometers | $km^2$ |
| | **VOLUME** | | | |
| fl oz | fluid ounces | 29.57 | milliliters | ml |
| gal | gallons | 3.785 | liters | l |
| $ft^3$ | cubic feet | 0.028 | cubic meters | $m^3$ |
| $yd^3$ | cubic yards | 0.765 | cubic meters | $m^3$ |

NOTE: Volumes greater than 1000 l shall be shown in $m^3$.

| | | | | |
|---|---|---|---|---|
| | **MASS** | | | |
| oz | ounces | 28.35 | grams | g |
| lb | pounds | 0.454 | kilograms | kg |
| T | short tons (2000 lb) | 0.907 | megagrams | Mg |
| | **TEMPERATURE (exact)** | | | |
| °F | Fahrenheit temperature | 5(F-32)/9 or (F-32)/1.8 | Celcius temperature | °C |
| | **ILLUMINATION** | | | |
| fc | foot-candles | 10.76 | lux | l |
| fl | foot-Lamberts | 3.426 | candela/$m^2$ | $cd/m^2$ |
| | **FORCE and PRESSURE or STRESS** | | | |
| lbf | poundforce | 4.45 | newtons | N |
| psi | poundforce per square inch | 6.89 | kilopascals | kPa |

## APPROXIMATE CONVERSIONS FROM SI UNITS

| Symbol | When You Know | Multiply By | To Find | Symbol |
|---|---|---|---|---|
| | **LENGTH** | | | |
| mm | millimeters | 0.039 | inches | in |
| m | meters | 3.28 | feet | ft |
| m | meters | 1.09 | yards | yd |
| km | kilometers | 0.621 | miles | mi |
| | **AREA** | | | |
| $mm^2$ | square millimeters | 0.0016 | square inches | $in^2$ |
| $m^2$ | square meters | 10.764 | square feet | $ft^2$ |
| $m^2$ | square meters | 1.195 | square yards | $yd^2$ |
| ha | hectares | 2.47 | acres | ac |
| $km^2$ | square kilometers | 0.386 | square miles | $mi^2$ |
| | **VOLUME** | | | |
| ml | milliliters | 0.034 | fluid ounces | fl oz |
| l | liters | 0.264 | gallons | gal |
| $m^3$ | cubic meters | 35.71 | cubic feet | $ft^3$ |
| $m^3$ | cubic meters | 1.307 | cubic yards | $yd^3$ |

| | | | | |
|---|---|---|---|---|
| | **MASS** | | | |
| g | grams | 0.035 | ounces | oz |
| kg | kilograms | 2.202 | pounds | lb |
| Mg | megagrams | 1.103 | short tons (2000 lb) | T |
| | **TEMPERATURE (exact)** | | | |
| °C | Celcius temperature | 1.8C + 32 | Fahrenheit temperature | °F |
| | **ILLUMINATION** | | | |
| lx | lux | 0.0929 | foot-candles | fc |
| $cd/m^2$ | candela/$m^2$ | 0.2919 | foot-Lamberts | fl |
| | **FORCE and PRESSURE or STRESS** | | | |
| N | newtons | 0.225 | poundforce | lbf |
| kPa | kilopascals | 0.145 | poundforce per square inch | psi |

* SI is the symbol for the International System of Units. Appropriate rounding should be made to comply with Section 4 of ASTM E380.

(Revised August 1992)

**Technical Report Documentation Page**

| 1. Report No. | 2. Government Accession No. | 3. Recipient's Catalog No. |
|---|---|---|
| Final Report | | |

| 4. Title and Subtitle | 5. Report Date |
|---|---|
| DEVELOP METHODOLOGIES/PROTOCOLS TO ASSESS CRACKING POTENTIAL OF ASPHALT MIXTURES USING ACCELERATED PAVEMENT TESTING | September, 2007 |
| | 6. Performing Organization Code: 00051675 |
| 7. Author(s): Dr. R. Roque, A. Guarin, G. Wang, J. Zou, and Dr. H. Mork | 8. Performing Organization Report No. |
| 9. Performing Organization Name and Address: University of Florida, Department of Civil and Coastal Engineering, 365 Weil Hall P.O. Box 116580, Gainesville, FL 32611 | 10. Work Unit No. (TRAIS) |
| | 11. Contract or Grant No.: 00051675 |
| 12. Sponsoring Agency Name and Address: Florida Department of Transportation, 605 Suwannee Street, MS 42, Tallahassee, FL 32399 | 13. Type of Report and Period Covered: Final Report, Mar. 18, 2005 - Sep. 9, 2007 |
| | 14. Sponsoring Agency Code |

15. Supplementary Notes: Prepared in cooperation with the Federal Highway Administration

16. Abstract

Methodologies were identified which involved the use of the accelerated pavement aging system (APAS) to induce age-hardening of the pavement in the accelerated pavement testing (APT) facility and achieve stiffness profiles consistent with those observed in field-aged pavements, followed by loading with and without wander using the heavy vehicle simulator (HVS). These approaches would allow us to evaluate several hypotheses associated with the development and accumulation of damage and its effect on top-down cracking, as well as hypotheses associated with the energy-based cracking criteria developed in earlier FDOT research efforts.

Properties determined from FWD tests on the pavement sections and Superpave IDT tests performed on asphalt concrete cores obtained from the pavements at different aging levels have been used to predict stresses, strains, and energies due to applied wheel loads. Excellent correspondence has been observed between predicted and measured strains. strains measured using gages epoxied to the surface of the pavement are excellent tools for evaluation of pavement load response, but are not good indicators of the development of damage

Top-down cracking was achieved only when the pavement was aged beyond normal levels to reduce fracture resistance and minimize healing potential. However, in contrast with field observations, where top-down cracks are longitudinal, the cracks developed by the HVS were transverse. Theoretical analyses indicated that transverse cracks were explained by the much slower speed of the HVS load that resulted in much greater damage in the longitudinal direction than in the transverse direction. Several recommendations were made to conduct further investigations and modify the existing APT system to better simulate the mechanisms that lead to top-down cracking in the field.

| 17. Key Word | 18. Distribution Statement |
|---|---|
| HVS, APAS, aging, loading, modeling, cracking, strain, FWD, Superpave IDT, energy ratio | No restrictions. This document is available to the public through the National Technical Information Service, Springfield, VA, 22161 |

| 19. Security Classif. (of this report) | 20. Security Classif. (of this page) | 21. No. of Pages | 22. Price |
|---|---|---|---|
| Unclassified | Unclassified | 124 | |

# ACKNOWLEDGMENTS

The authors would like to acknowledge and thank the Florida Department of Transportation (FDOT) for providing technical and financial support and materials for this project. Special thanks go to engineers and technicians at the Accelerated Pavement Testing (APT) facility and the Bituminous Section of the State Materials Office for their contributions and their expert knowledge, experience, and constructive advice throughout the course of this work. This project was truly a collaborative effort that would not have been possible without the work of many individuals at FDOT's Materials Research Park.

# EXECUTIVE SUMMARY

The accelerated pavement aging system (APAS) was successfully used to induce age-hardening of the pavement in the accelerated pavement testing (APT) facility and achieve stiffness profiles consistent with those observed in field-aged pavements. Also the pavement was loaded with and without wander using the heavy vehicle simulator (HVS). These approaches allowed the evaluation of several hypotheses associated with the development and accumulation of AC damage and its effect on topdown cracking, as well as hypotheses associated with the energy-based cracking criteria developed in earlier FDOT research efforts.

Properties determined from FWD tests on the pavement sections and Superpave IDT tests performed on asphalt concrete cores obtained from the pavements at different aging levels were used to predict stresses, strains, and energies due to applied wheel loads. Excellent correspondence was observed between predicted and measured strains, thereby establishing the validity of the analytical models used as well as the tests used to obtain material properties. This resulted in greater confidence in stresses and energies predicted by the models used. Analyses also led to the following findings: 1) strains measured using gages epoxied to the surface of the pavement are excellent tools for evaluation of pavement load response, but are not good indicators of the development of damage in the asphalt pavement and are of limited use in detection of crack initiation unless the gage happens to be located immediately on the crack at the time of initiation; 2) the pavement available for testing for this project was unlikely to crack unless significant damage developed, accumulated, and did not heal during the course of continued HVS loading because the mixture had excellent fracture resistance, the base

course was very stiff, and temperatures were generally not low enough for significant non-healable damage to develop.

Several systems were identified as potential candidates to detect age-hardening and cracking in the APT facility, including impact-echo, SASW, and electrical resistivity. Initial tests with SASW indicated that existing measurement techniques and interpretation methods were not optimized for purposes of detecting the near-surface changes resulting either from age-hardening or damage. Also, the system was rather cumbersome in its current state and required high level technical expertise to perform and interpret the tests at this time. More extensive evaluations were conducted using impact echo, but it was eventually determined that the system is not sensitive enough to reliably detect stiffness changes associated with age-hardening, damage, or the presence of a surface crack. Electrical resistivity tests performed on cores in the laboratory indicated that this approach does have potential for crack and damage detection. However, the system would have to be developed and evaluated for use on full-scale pavements.

Aging with the APAS and loading with the HVS was performed on three pavement sections (A, B, and C) on lane 1 of the APT. Section C was the first section tested and extensive work was done to evaluate the APAS system and to establish the aging protocols needed to induce appropriate stiffness gradients. Experience was also obtained with strain gage measurements on this section. In fact, unusual results led to an investigation of base conditions that revealed that moisture had reached the base layer on the south side of the APT facility. This was caused by a high water table resulting from extensive rains from hurricanes in 2004 and 2005. Section B was extensively aged to more carefully evaluate the age-hardening characteristics of the APAS systems, as well as to minimize healing and embrittle the pavement sufficiently to enhance the potential for cracking. More extensive strain gage measurements and analyses were performed on

section B and excellent predictions of load-induced strain profiles were obtained. A significant number of wheel load applications clearly indicated that this pavement would not crack regardless of number of load applications. This result indirectly validated the concept that a critical condition, not cumulative micro-damage, that exceeds the energy limits of the mixture is required to cause cracking, which is the basic premise of the HMA fracture model established by earlier FDOT research. The relatively mild temperatures combined with good mixture properties (even after aging) and stiff base could not induce the critical energy levels necessary to initiate cracking, regardless of load repetition, even at 18,000 lbs.

Loading tests also indicated that healing was likely playing a major role on pavement cracking performance. Therefore, section 1A was aged at least twice as much as Section 1B with the idea of completely eliminating the potential for healing and causing the pavement surface to become very brittle and unable to relax stresses. Once again, extensive strain measurements were obtained and good agreement was observed between predicted and measured strain. As with section 1B, no cracking was observed during times of relatively mild temperatures. However, transverse cracks initiated in the wheel path during periods of cold temperatures approaching freezing. Interestingly, cracks did not develop in the unaged portion of the loaded section. Crack development in Section A was carefully tracked for analysis; additional mixture tests were conducted on pavement cores to determine whether the models used can predict the observed response and distress. A heating index was used to measure the degree of aging induced. The higher the heating index, the more aged the pavement. According to this index, section 1A was the most aged section, while section 1C was the least aged section.

Initially, thermal stresses were believed to play a major role in the development of transverse cracking. However, theoretical analysis indicated that the critical load stress

for the tire load used was actually along the longitudinal wheelpath, which explained the presence of transverse cracks; these results suggest that thermal stresses appeared to play a minor role in the transverse crack development.

TABLE OF CONTENTS

# LIST OF TABLES

LIST OF FIGURES

# CHAPTER 1
# INTRODUCTION

## 1.1 Background

Evaluation of cracking potential of asphalt mixture and pavement in the field can be difficult, expensive, and time consuming. Field studies are particularly impractical for evaluating the performance of new materials because reliable results may not be available for several years. Accelerated Pavement Testing (APT) offers enormous potential for evaluation of pavement distress mechanisms and performance of asphalt mixture and pavement in relatively short periods of time. Consequently, FDOT made a strategic investment to set up an APT facility in Gainesville, Florida. The system includes a fully mobile heavy vehicle simulator (HVS), eight linear tracks (150 ft. long by 12 ft. wide), and two additional tracks that allow for changes in the water table.

As with most of the other systems of this kind located throughout the world, experimental work to evaluate pavement performance has focused primarily on controlled temperature testing. In addition, there has been no success in inducing cracking in asphalt pavement in a realistic manner using the APT. The following issues have been identified as impediments to success in this area: 1) the fact that long-term environmental effects that cause asphalt mixture and pavement to become stiffer and more brittle through age-hardening are not typically replicated in APT experiments. 2) Temperature changes that induce tensile stresses and cause significant stiffness gradients and changes in stress distributions to develop within the asphalt layer are typically not replicated. Both of these issues have been determined to play a significant role in the

development of top-down cracking, which is the most prevalent form of cracking in flexible pavement in Florida.

In an effort to simulate age-hardening of in-service pavement, FDOT has acquired a unit called Accelerated Pavement Aging System (APAS) which allows for artificial aging of asphalt pavement test sections in the APT facility. This unit may be the first of its kind in the world; it offers unparalleled opportunities to create the appropriate conditions necessary to create realistic mechanisms to induce and evaluate cracking potential of asphalt mixture and pavement in the APT. However, methodologies and protocols need to be developed to address artificial aging of asphalt pavement using the new unit. Also, appropriate APT experiments need to be designed to assess cracking potential of asphalt mixture and pavement subjected to realistic mechanisms involving relevant environmental effects and loading configurations. Successful experiments of this type offer great potential to improve pavement durability through improved understanding of the mechanisms of cracking in asphalt pavement.

## 1.2 Objectives

The primary objective of this work was to identify and recommend practical methodologies for a realistic investigation of cracking potential of asphalt mixtures using accelerated pavement testing for Florida conditions. The following five tasks were identified to meet this objective:

1) Identify candidate methodologies for detailed evaluation.
2) Conduct analysis for experiment design.
3) Evaluate existing measurement and detection systems for age-hardening and cracking.
4) Conduct APT and laboratory experiments to evaluate candidate methodologies.

5) Document methodologies for APT cracking experiments on asphalt pavement.

### 1.3 Scope

Given that the primary objective was to develop methodologies for aging and loading a pavement to induce top-down cracking and not to conduct a top-down cracking evaluation of different pavement systems, the efforts in this project focused on a single pavement. This lane was composed of one dense-graded mixture on limestone base and sand subgrade. The lane was divided into three test sections that were subjected to different aging and loading and measurement procedures to help identify the best methodologies for future evaluation of cracking at the APT.

# CHAPTER 2
# PROJECT DESCRIPTION

## 2.1 Overview

Lane 1 of the APT test area at the FDOT State Materials Research Park was used as the HVS testing track in this study. The lane was divided into three sections, namely Section 1A, Section 1B and Section 1C. The purpose of each section is described as follows:

1) Section 1C was the first section tested to evaluate the accelerated pavement aging system (APAS) and to establish the aging protocols needed to induce appropriate stiffness gradients. The 1C section involved three phases. Phase I was used to test the performance and ability of surface strain gages to capture pavement response under HVS loading, while Phase II and III were used to detect surface cracking and evaluate models.
2) Section 1B was the second section for HVS testing. This section was designed with the idea of extensive aging by APAS to induce stiffness gradients, minimize healing properties of the asphalt material and embrittle the pavement sufficiently to enhance the potential for cracking. Also, HVS loading would be carried out with wander to test the idea of whether strain gages could be survived directly under wheel.
3) Section 1A was the last section tested. The section was divided into two parts, namely aged part and un-aged part. The main purpose of this section was to employ what was learned from sections 1B and 1C and crack the pavement.

The test section layout is shown in Figure 2.1.

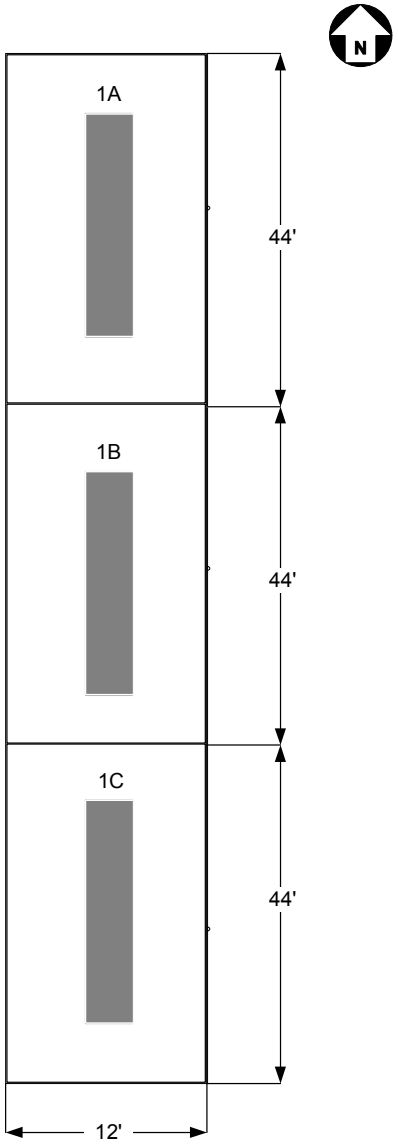


Figure 2.1 Test Sections Layout

## 2.2 Materials

The three sections evaluated in this project (1A, 1B, and 1C) were constructed with the same asphalt mixture. Georgia granite aggregate was used in the research; the source of aggregates is shown in Table 2.1. Binder PG 67-22, which is commonly used in Florida, was selected.

Table 2.1 Aggregate Sources

| Source | Type | FDOT code | Pit No. | Producer |
|---|---|---|---|---|
| GA Granite | # 78 Stone | 43 | GA-553 | Junction City Mining |
| | # 89 Stone | 51 | GA-553 | Junction City Mining |
| | W-10 Screenings | 20 | GA-553 | Junction City Mining |

## 2.3 Gradations

At the APT site, three lanes were paved with a fine-graded Superpave mixture. Each lane consists of three test sections that can independently be subjected to traffic using the Heavy Vehicle Simulator (HVS); each lane was constructed with two lifts of the same 12.5 mm NMAS (Nominal Maximum Aggregate Size) mixture.

Table 2.2 presents the mixture design properties and in-place gradations for the top and bottom lifts (the JMF was the same for both lifts). Figures 2.2 and 2.3 show the in-place gradations of each lift compared to the JMF. It is interesting to note that in every case the in-place gradation was coarser than JMF.

Table 2.2 Mixture Design Properties for the Top Lift

| | | Top Lift | | | Bottom lift | | |
|---|---|---|---|---|---|---|---|
| Section | | 1A | 1B | 1C | 1A | 1B | 1C |
| $G_{mm}$ | 2.579 | 2.594 | 2.594 | 2.590 | 2.585 | 2.585 | 2.578 |
| $G_{mb}$ | 2.475 | 2.493 | 2.493 | 2.487 | 2.487 | 2.487 | 2.493 |
| % AC | 4.6 | 4.4 | 4.4 | 4.3 | 4.1 | 4.1 | 4.6 |
| Air Voids | 4.0 | 3.9 | 3.9 | 4.0 | 3.8 | 3.8 | 3.3 |
| VMA | 14.7 | 14.2 | 14.2 | 14.3 | 13.9 | 13.9 | 14.1 |
| VFA | 73 | 73 | 73 | 72 | 73 | 73 | 77 |
| $P_{be}$ | 4.5 | 4.3 | 4.3 | 4.3 | 4.1 | 4.1 | 4.5 |
| Dust Ratio | 1.1 | 1.2 | 1.2 | 1.0 | 1.0 | 1.0 | 1.0 |
| 3/4" | 100.0 | 100.0 | 100.0 | 100.0 | 100.0 | 100.0 | 100.0 |
| 1/2" | 98.0 | 97.7 | 97.7 | 96.8 | 97.6 | 97.6 | 98.6 |
| 3/8" | 90.0 | 88.5 | 88.5 | 85.4 | 86.8 | 86.8 | 90.0 |
| #4 | 68.0 | 61.6 | 61.6 | 58.9 | 54.7 | 54.7 | 63.4 |
| #8 | 48.0 | 44.5 | 44.5 | 42.5 | 38.3 | 38.3 | 44.7 |
| #16 | 34.0 | 34.1 | 34.1 | 32.7 | 29.5 | 29.5 | 32.9 |
| #30 | 25.0 | 27.3 | 27.3 | 26.2 | 23.6 | 23.6 | 26.0 |
| #50 | 16.0 | 17.5 | 17.5 | 16.5 | 15.3 | 15.3 | 16.2 |
| #100 | 8.0 | 8.2 | 8.2 | 7.6 | 6.8 | 6.8 | 7.6 |
| #200 | 4.9 | 4.9 | 4.9 | 4.4 | 4.1 | 4.1 | 4.7 |
| Density | 93.0 | 92.8 | 92.1 | 92.6 | 93.1 | 92.8 | 93.3 |

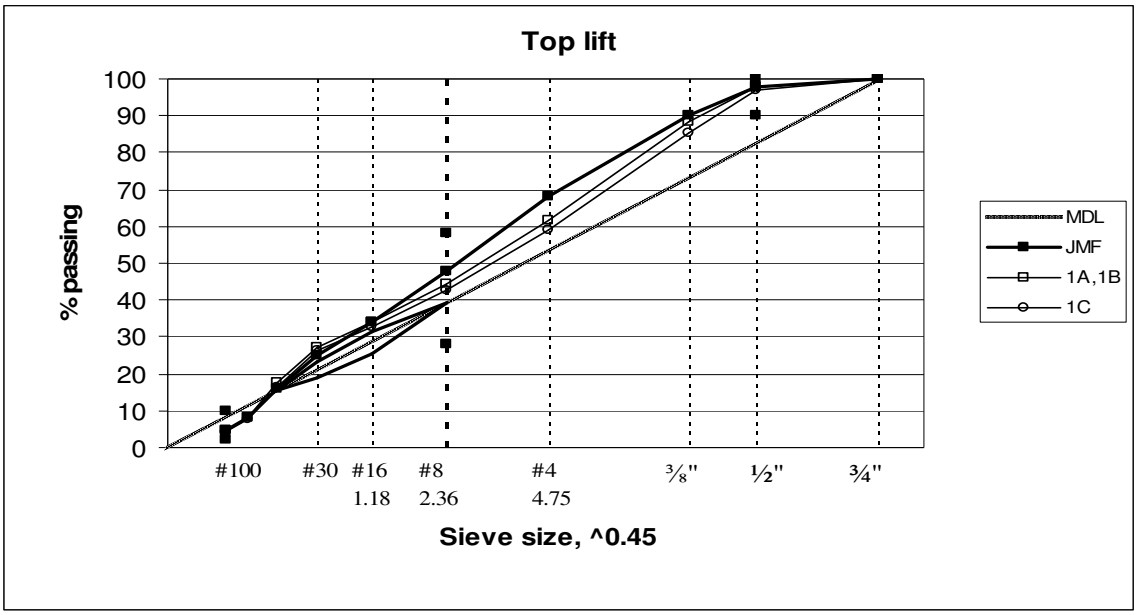


Figure 2.2 Top lift gradations

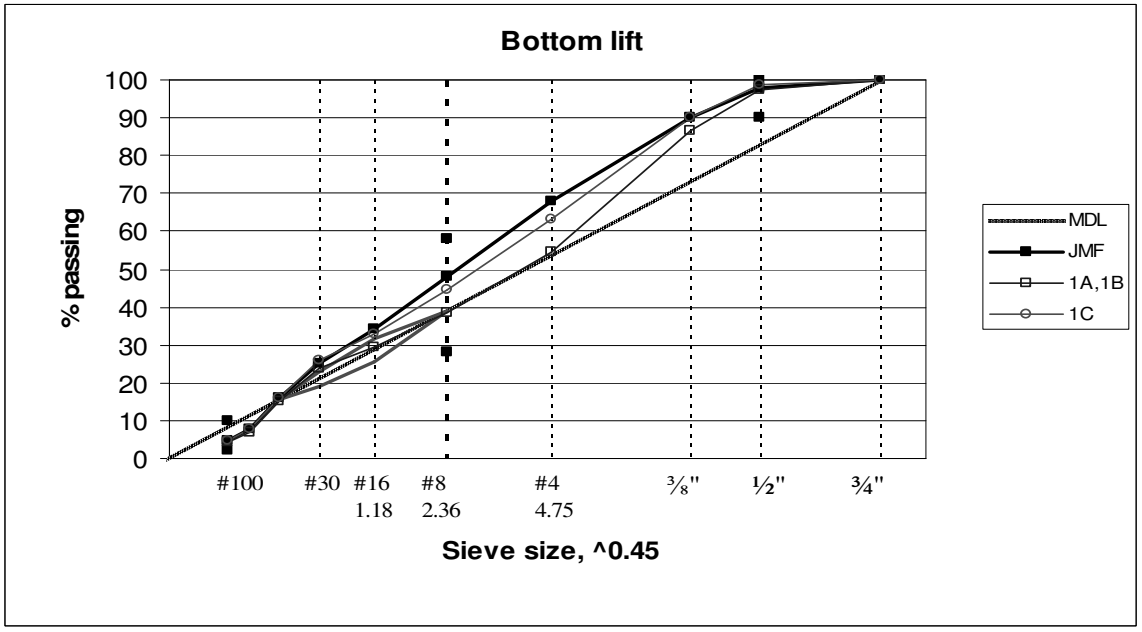


Figure 2.3 Bottom lift gradations

All gradations were evaluated by using the DASR concept and porosity criterion (Roque et al, 2006); according to this system, DASR porosity greater than 50% or gradations marginally interactive could result in poor rutting and possibly poor cracking performance.

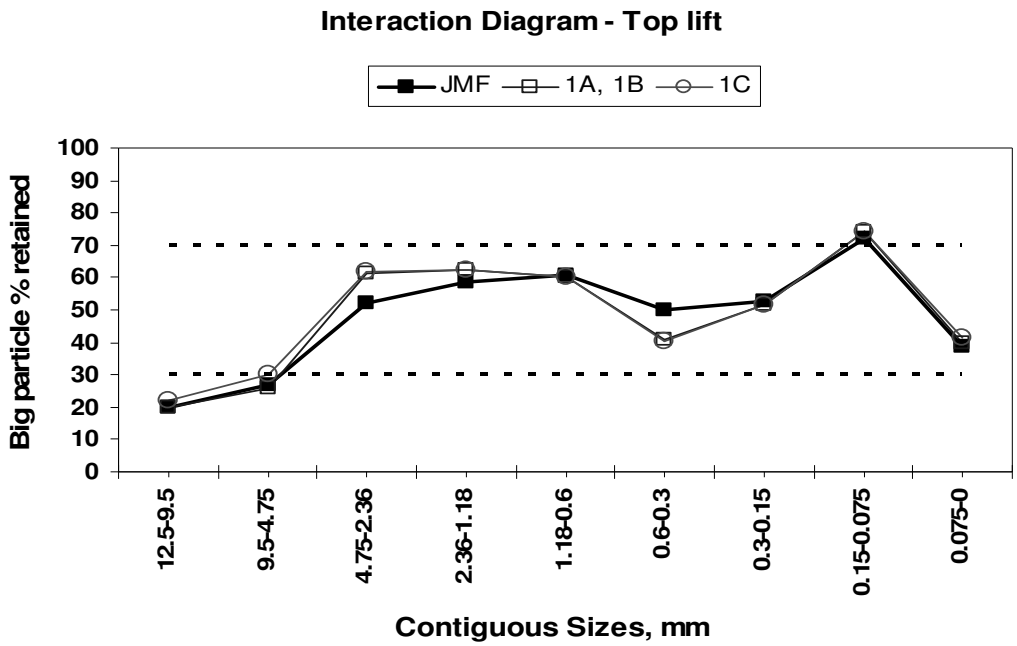


Figure 2.4 Interaction Diagram for top lift.

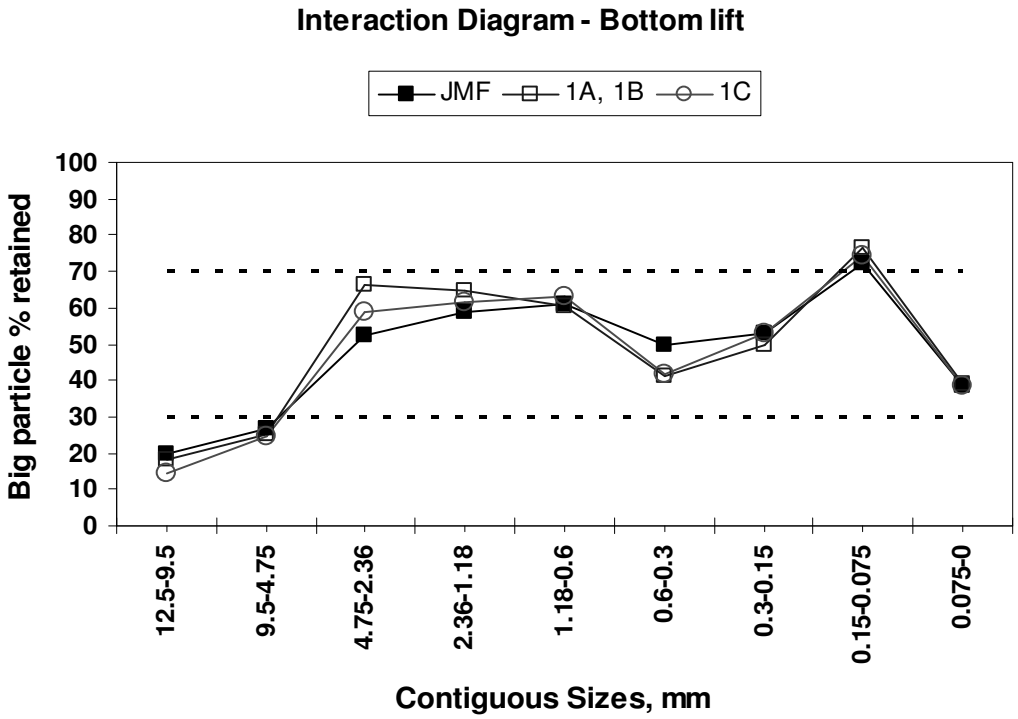


Figure 2.5 Interaction Diagram for bottom lift

Interaction diagrams determined from the in-place gradations and JMF for the top and bottom lifts are presented in Figures 2.4 and 2.5. Interaction diagrams show little

difference between the top and bottom lifts; these diagrams indicate that aggregate sizes between 4.75 mm and 1.18 mm are clearly interactive; in the 1C top lift mix the 9.5 mm size appears to be marginally interactive with a relative proportion between the 9.5/4.75 mm sizes right at 70/30. Therefore, the dominant aggregate size range (DASR) of the 1C top lift is either from 9.5 mm to 1.18 mm, or from 4.75 mm and 1.18 mm, depending on whether or not the 9.5 mm size is considered interactive. If 9.5mm size is considered interactive, 1C top lift DASR porosity is 43.3%; if 9.5mm is not interactive, its porosity is 48.2%; in either case, DASR porosity is lower than 50%, indicating a potentially good performing mixture.

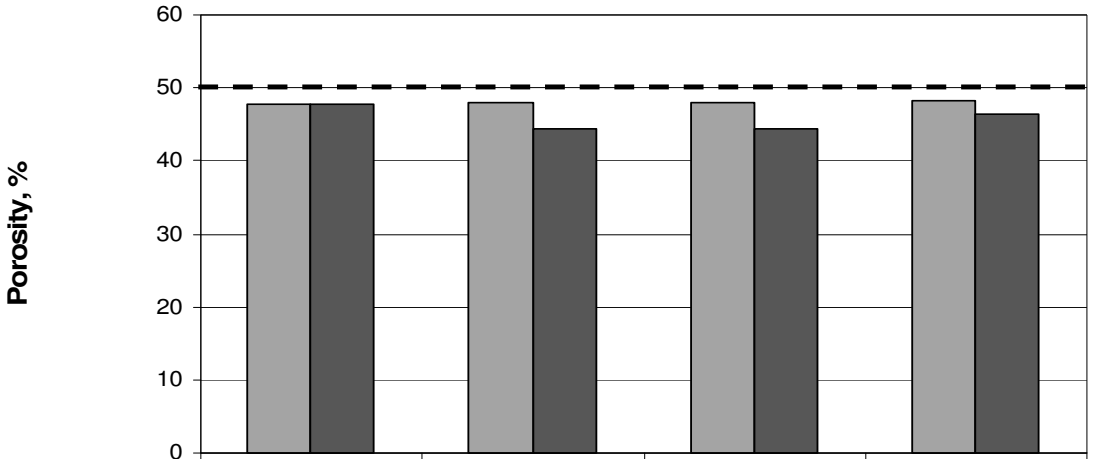


| | JMF | 1A | 1B | 1C |
|---|---|---|---|---|
| Top Lift | 47.8 | 48.1 | 48.1 | 48.2 |
| Bottom Lift | 47.8 | 44.3 | 44.3 | 46.4 |

Figure 2.6 DASR Porosity (top and bottom lifts)

Figure 2.6 shows DASR porosity for all sections and lifts. As shown in the figure, in all cases the DASR porosity was less than 50%. This means that good field rutting and possibly good cracking performance should be expected from these mixtures. Some researchers suggest that good rutting performance of the mix could be linked to good cracking performance in the field.

# CHAPTER 3
# ACCELERATED PAVEMENT AGING SYSTEM (APAS)

Top-down cracking is a mechanism believed to be strongly affected by changes in material properties in the near-surface part of asphalt pavements, which in Florida are highly exposed to age-hardening and embrittlement from abundant sunshine. To accelerate the aging processing and thus to create stiffness gradients in the test sections, an Accelerated Pavement Aging System (APAS) was developed at the APT facility of FDOT. This system is considered the first of its kind in the world; it offers unparalleled opportunities to create the appropriate conditions necessary to create realistic mechanisms to induce and evaluate cracking potential of asphalt mixture and pavement in the APT. The APAS equipment has been successfully evaluated and calibrated at the APT facility. The following sections will summarize the APAS aging activities throughout the project.

The artificial aging at Section 1 started at the southern Section 1C and the middle Section 1B by December 2005. Although somewhat different, all the aging at both southern sections was performed prior to HVS testing. The original project plan was to use the experience from these sections to develop a final procedure for aging and HVS loading to better replicate field conditions at the northern Section 1A. However, the aging at Section 1A was also carried out in full without any traffic loads involved. By November 2006, Section 1A had been exposed to slightly more than double the artificial aging effort applied on Section 1B.

It should be noted that artificial aging, which was carried out over a limited period of time, can not directly replicate natural aging, which takes place over several years involving other processes, some of them not well known or understood. As binder oxidation, a process known to be a substantial part of aging, is heavily influenced by temperature, the APAS equipment developed at FDOT uses heat as the driving force for accelerated aging, while other effects such as UV radiation, and the combined effect of traffic loads, debris, shrinkage, and precipitation are not taken into account, at least not directly.

Another important goal of the APAS testing was to create an aging or stiffness gradient through the asphalt concrete layer, which is known to exist in the field. This was achieved by maintaining a temperature gradient through the asphalt layer by not keeping the APAS heaters on for so long so that the bottom temperature was always significantly lower than the surface. Consequently, heating cycles were applied and repeated to achieve the intended effects regarding stiffness and brittleness. Temperature control therefore turned out to be a crucial part of the aging procedure.

The temperatures during aging were monitored by two different systems, one system connected to the APAS itself, and one auxiliary system. For each of the twelve transverse APAS heaters there are two thermocouples; one at the surface and another one at 2” depth, each of them with a temperature resolution of 1 ºC, and all of them mounted within one foot of the midpoint of the heaters. This system has been unchanged throughout the aging process. Prior evaluation of the APAS by FDOT personnel indicated that the system resulted in a uniform temperature distribution within the area.

### 3.1 Section 1C

The artificial aging at Section 1C was conducted in the first half of June 2005, with a start-up at 3:30 pm May 31. It was carried out in two cycles; each one included three consecutive days of heating with the APAS, in such a way that the surface temperature after a heat-up period was kept constant at 90 ºC. Between the heating cycles, the APAS was removed and the pavement was allowed to cool down for seven days. During the heating-cooling-heating process, the temperature was monitored with both the APAS and the auxiliary temperature systems. Figure 3.1 shows some of the measured temperatures during the first three-day cycle (there are no data for the auxiliary temperature system until around 9 AM June 1, and due to a minor reference error the surface temperature for June 2 is from heater #7 instead of heater #6). Figure 3.2 shows the corresponding temperatures for the second heating cycle.

The total aging procedure at Section 1C is summed up in table 3.1 The length of the cycle is determined from start-up until the APAS heaters are switched off and the temperature starts to drop. In order to compare different heating cycles, a surface heating index $\Sigma(t \bullet \Delta T)$ was calculated, where $\Delta T = T_i^{surface} - T_{start}^{ambient}$, until the heaters are switched off. This index provides a parameter that can be used to compare the amount of aging imposed, considering the effects of both temperature and time.

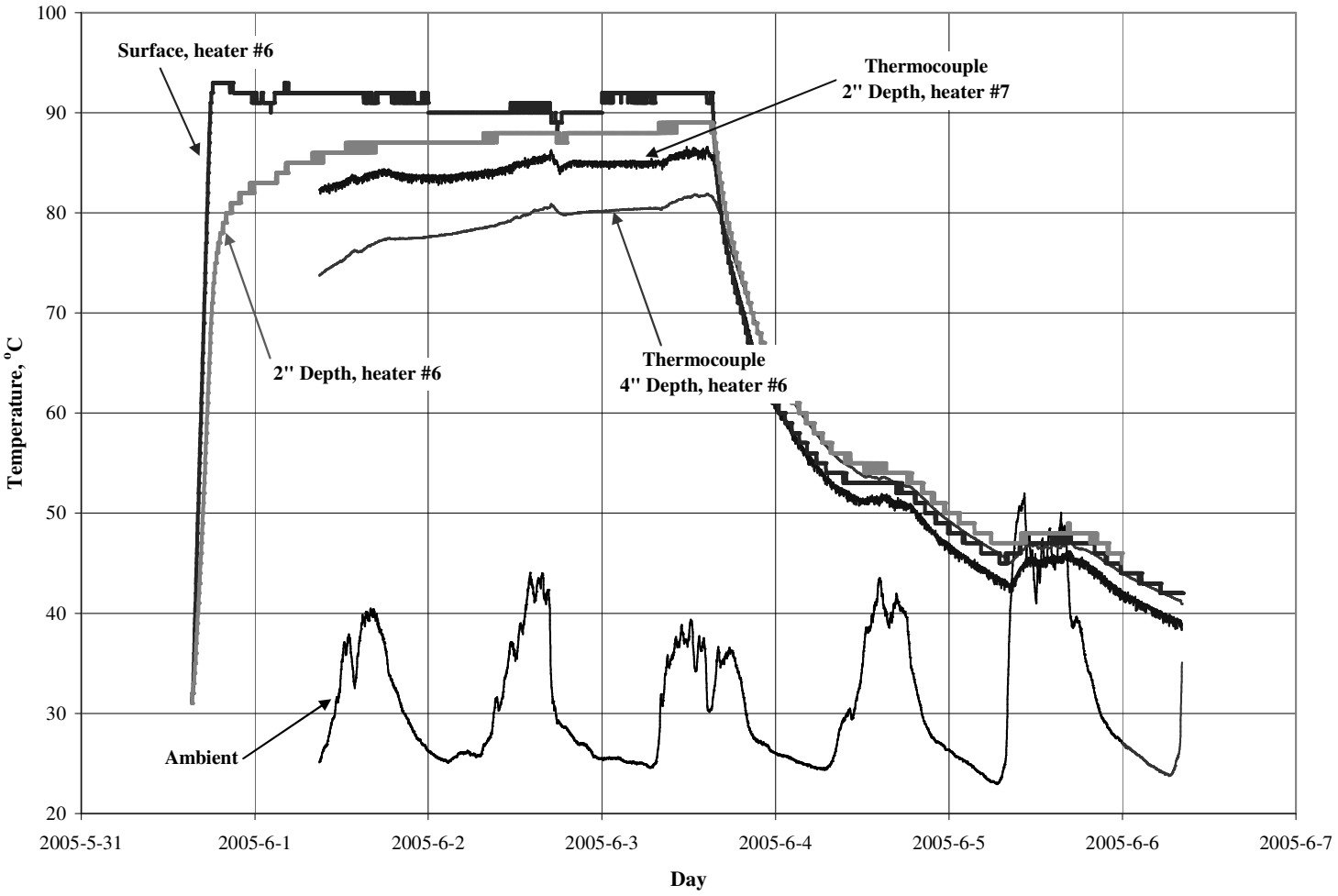


Figure 3.1 Temperatures during 1st Heating Cycle at Section 1C

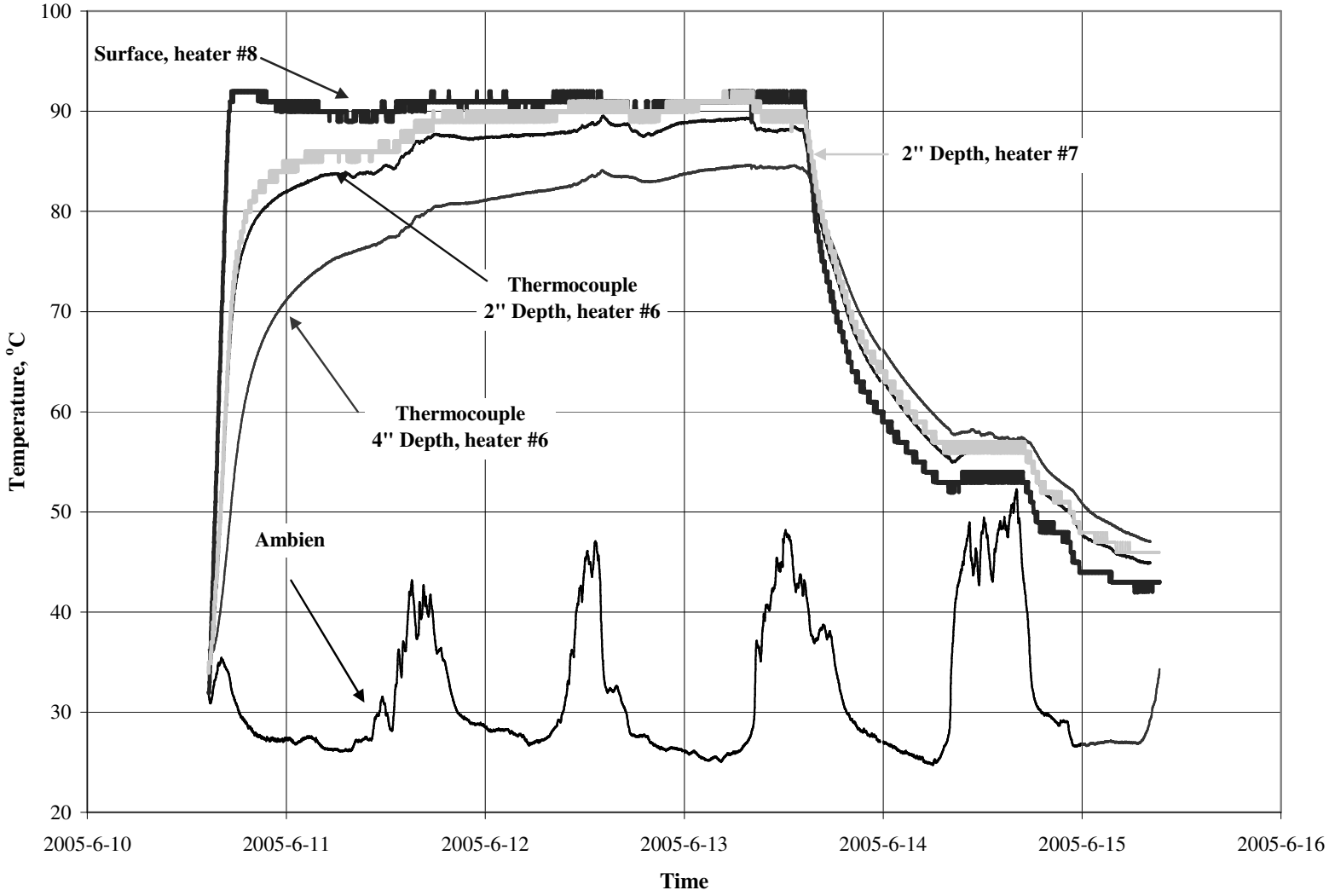


Figure 3.2 Temperatures during 2nd Heating Cycle at Section 1C

Table 3.1 Characteristics for Section 1C heating procedure

| Cycle | Start time | Length of cycle until shut-off | Time from shut-off until next cycle | Surface heating index [h ºC]* |
|---|---|---|---|---|
| 1 | 05/31/2005 3:28 PM | 3 days (72 hours) | 6 days 23 h 24 min | 4215.5 |
| 2 | 06/10/2005 2:42 PM | 3 days (72 hours) | | 4156.3 |

* Calculated as $\Sigma(t \bullet \Delta T)$, where $\Delta T = T_i^{surface} - T_{start}^{surface}$, until heater is switched off

Based on these initial aging experiments, it was concluded that the APAS was able to maintain a steady pavement temperature with varying ambient temperature. Also the thermocouples at 2" depth were showing fairly similar values regardless of the system they were connected to, and as expected, the temperature rise time increased with the depth from the surface. The main conclusion, however, was that to maintain a steady temperature gradient over the pavement layer, the length of one heating cycle should be less than three days. On the other hand, as the 2" and 4" temperatures become fairly similar pretty soon after heating is ended, the period between aging cycles can be significantly reduced to one day or less.

### 3.1.1. Binder Testing

Figure 3.3 shows the viscosity of the recovered binder from the Section 1C specimens, taken before aging (0 Days), after the first aging cycle (3 Days) and after the second aging cycle (6 Days).

As can be seen, there is a tremendous increase in viscosity with increased aging, especially for the top part of the asphalt core, for which the viscosity is more than doubled after the second aging cycle. A similar, but not as dramatic effect is seen for DSR stiffness, shown in figure 3.4.

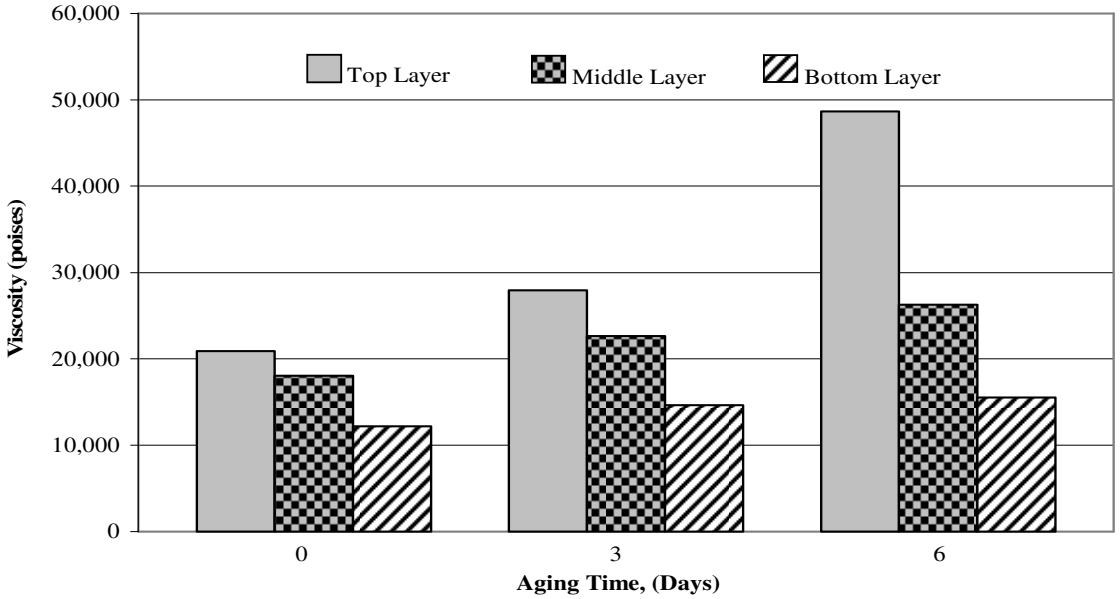


Figure 3.3 Recovered viscosity at different levels of aging at Section 1C

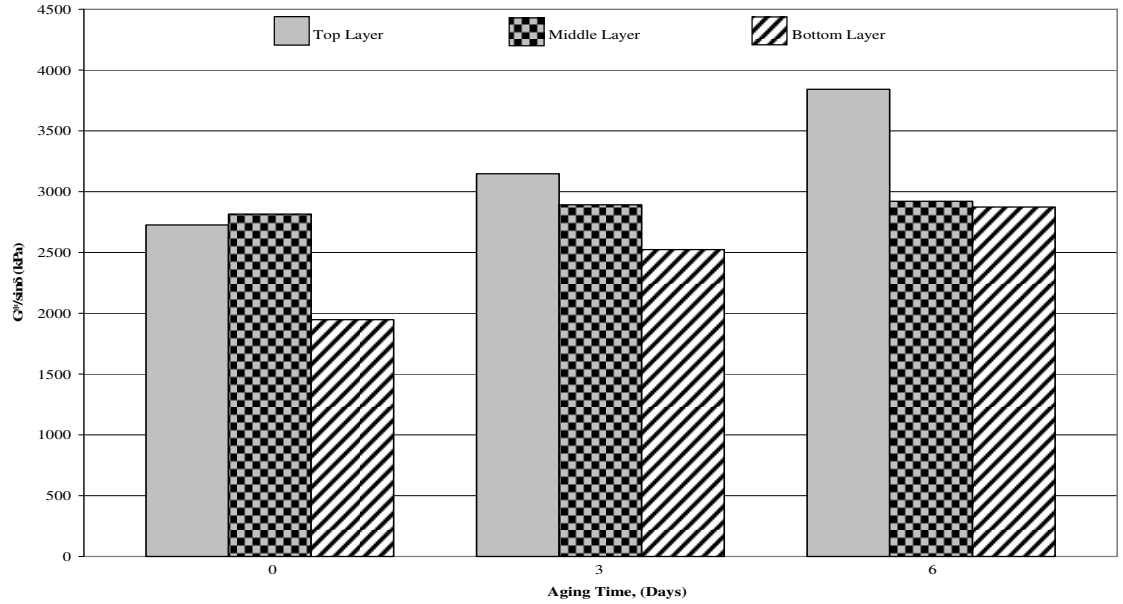


Figure 3.4 DSR stiffness for recovered binder at different levels of aging at Section 1C

As shown in table 3.2, which summarizes the binder investigation carried out for Section 1C, the penetration slightly decreases and the BBR stiffness increases with increased aging, and the effects are generally greatest for the top specimens, as expected.

Table 3.2 Binder investigation for specimens taken during aging at Section 1C

| Sample No. | Day 0 Top | Day 0 Middle | Day 0 Bottom | Day 3 Top | Day 3 Middle | Day 3 Bottom | Day 6 Top | Day 6 Middle | Day 6 Bottom |
|---|---|---|---|---|---|---|---|---|---|
| **TEST ON RECOVERED ASPHALT** | | | | | | | | | |
| Penetration @ 77 ºF | 25 | 24 | 26 | 21 | 22 | 26 | 17 | 20 | 23 |
| | | | | | | | | | |
| Absolute Viscosity @ 140 ºF 30 cm Hg. Poises | 20,900 | 18,051 | 12,192 | 27,932 | 22,652 | 14,603 | 48,641 | 26,275 | 15,512 |
| | | | | | | | | | |
| DSR G*/sinδ kPa @ 10 rad/s, @ 25 ºC | 2727 | 2817 | 1946 | 3148 | 2893 | 2525 | 3842 | 2923 | 2875 |
| | | | | | | | | | |
| BBR Creep Stiffness S, MPa @ 60s @ -12 ºC | 137 | 129 | 108 | 131 | 141 | 96.1 | 165 | 145 | 135 |
| | | | | | | | | | |
| BBR Creep Stiffness M-Value @ 60s @ -12 ºC | 0.353 | 0.354 | 0.376 | 0.345 | 0.348 | 0.341 | 0.323 | 0.337 | 0.354 |
| | | | | | | | | | |

## 3.2 Section 1B

Based on the above observations, a completely different aging procedure was used for Section 1B, for which each cycle consisted of a heating-cooling-heating sequence. The set-up for the auxiliary temperature measurement system was modified. A typical heating cycle plot for this section is shown in Figure 3.5. The measurements were very similar to those obtained on section 1C. However, it doesn't make sense that the 4" value is higher than the 2" and surface values, except for the very beginning of the heating sequences, which might indicate there is something wrong with auxiliary temperature measurement system. Therefore, for consistence purpose, only temperatures

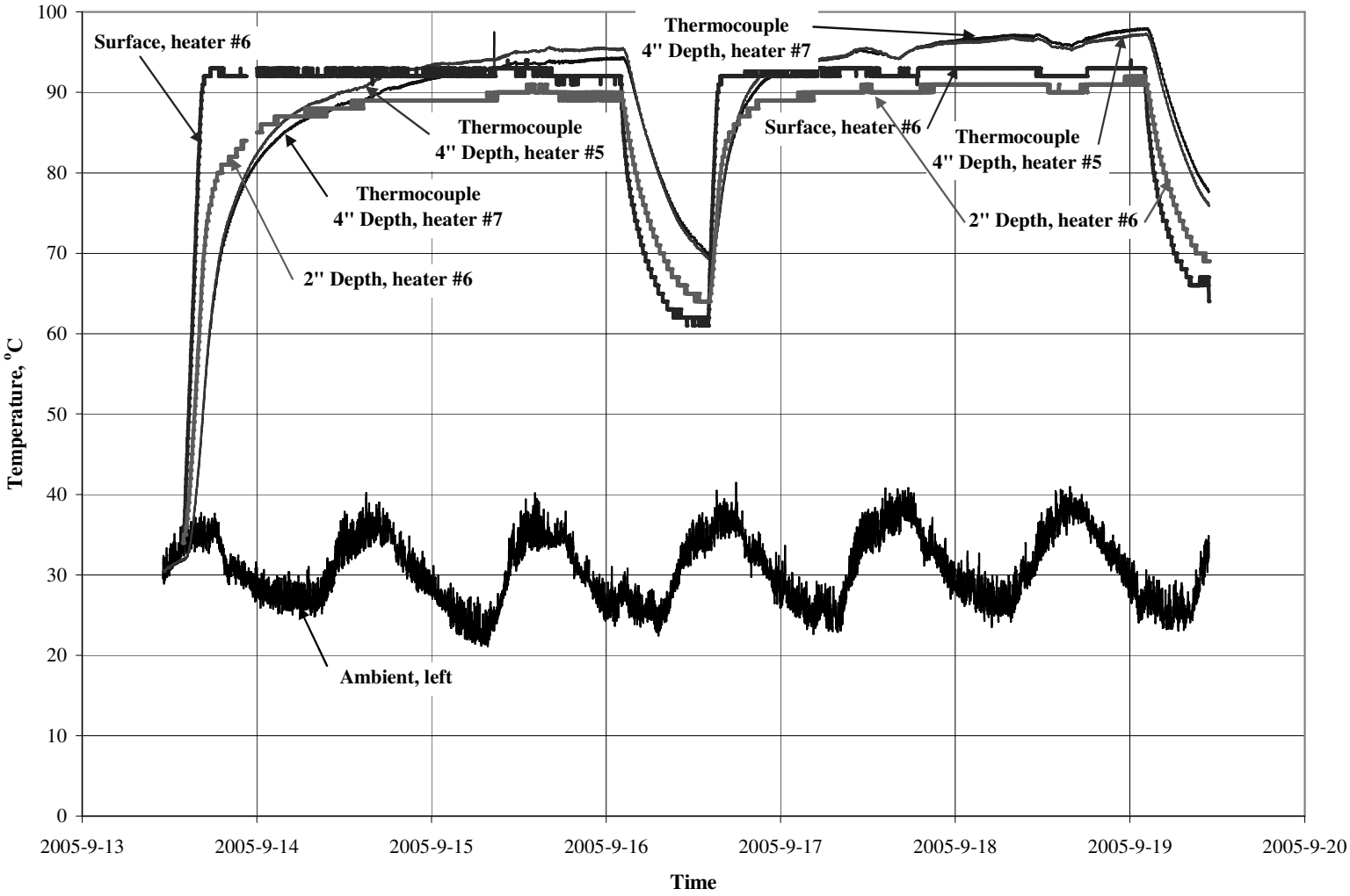


Figure 3.5 Typical Temperature plot during Heating Cycle at Section 1B

from APAS were used here.

Table 3.3 shows a summary for heating cycles at Section 1B. In this case, the surface heating index includes the fairly short shut-off time between the heating sequences. It is quite obvious that section 1B was subjected to much more severe artificial aging than section 1C.

Table 3.3 Characteristics for the Section 1B heating procedure

| Cycle # | Start time | Length of each heating sequence until shut-off | Length of shut-off period between heating sequences | Surface heating index [h ºC]* |
|---|---|---|---|---|
| 1 | 09/13/2005 1:50 PM | 60 hours | 12 hours | 7324.2 |
| 2 | 09/21/2005 3:00 PM | 60 hours | 12 hours | 7942.5** |
| 3 | 10/04/2005 2:02 PM | 48 hours | 24 hours | 7798.1 |
| 4 | 10/12/2005 4:10 PM | 48 hours | 24 hours | 8000.1 |
| 5 | 10/21/2005 3:25 PM | 48 hours | 24 hours | 7666.5 |
| | | | $\Sigma$ | 38731.4 |

* Calculated as $\Sigma(t \bullet \Delta T)$, where $\Delta T = T_i^{surface} - T_{start}^{surface}$, until heater is switched off the second time

** Because temperature acquisition system probably is switched on somewhat late, $T_{start}^{surface}$ is set to 30 ºC in this case

### 3.2.1 Binder Testing

Only viscosity measurements were carried out for the specimens from Section 1B. Figure 3.6 shows the viscosity of recovered binder from the Section 1B specimens before and during aging, with results from some additional cores taken in April ’06 before HVS loading started. For comparison, the concurrent results from Section 1C are shown in the same figure. In this figure, the results are presented with labels “0”, “1”, “2” and so on, for which the labels “1” and higher represent the aging cycles, and “0” is before artificial aging started.

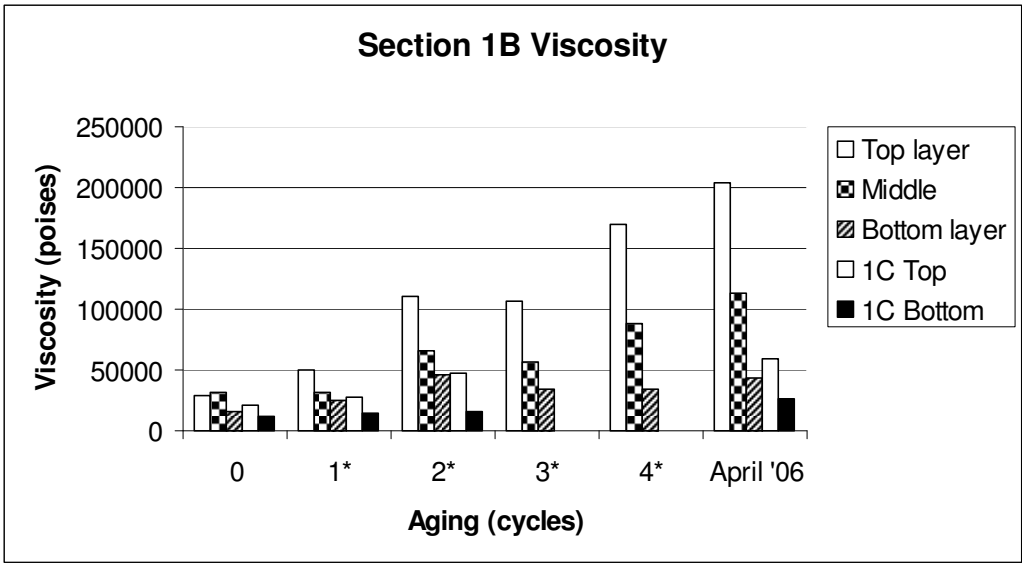


Figure 3.6 Recovered viscosity at different levels of aging at Section 1B and Section 1C

Even more obvious than for Section 1C (Figure 3.3), increased aging caused the top layer binder viscosity to increase dramatically. These values are significantly greater than viscosity of binders recovered from 20 year-old pavement sections in Florida, where the maximum reported viscosity was about 65000 poises. The April ’06 values also indicate that a significant amount of natural aging had taken place since the artificial aging ended in June and October 2005 for Section 1C and Section 1B, respectively.

Because the aging effort is so different for Section 1C and Section 1B, Figure 3.7 was created to show how viscosity varies with summed surface heating index. Only the top layer specimens from Section 1B and Section 1C are included. Figure 3.7 indicates that there is a fairly nice relationship between binder viscosity and imposed aging effort, which is relatively independent of the origin of the specimens.

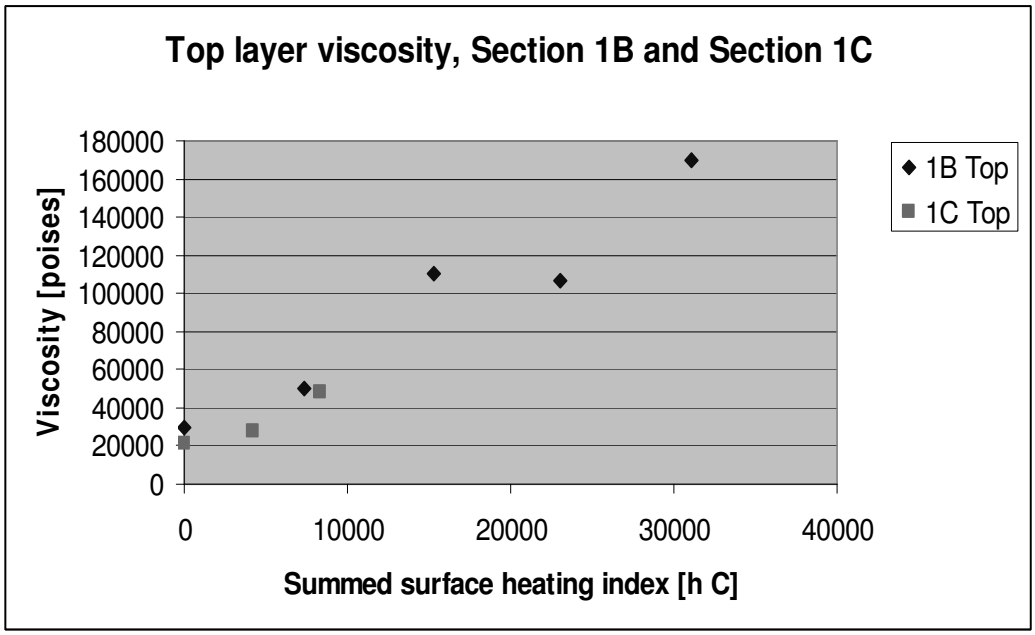


Figure 3.7 Recovered viscosity for top layer specimens from Section 1B and Section 1C

### 3.3 Section 1A

The heating process at Section 1A was similar to the one used for Section 1B, with a cycle of 48 hours heating, followed by 24 hours with no heating and then another 48 hours of heating constituting one heating sequence. The heating process started in September, 2006 and ended in January, 2007. More than 13 heating cycles were applied with total heating index of at least 97972.3 [h ºC]. The total aging procedure at Section 1A is summed up in Table 3.4. Clearly, Section 1A underwent more than twice as much artificial aging as Section 1B. A typical temperature plot during the heating process is given in Figure 3.8.

Table 3.4 Characteristics for the Section 1A heating procedure

| Cycle # | Start time | Length of each heating sequence until shut-off | Length of shut-off period between heating sequences | Surface heating index [h ºC] |
|---|---|---|---|---|
| 1 | 09/14/2006 6:29 PM | 48 hours | 24 hours | 6734.7 |
| 2 | 09/20/2006 3:30 PM | 48 hours | 24 hours | 7465.8 |
| 3 | 09/27/2006 2:02 PM | 48 hours | 24 hours | 6599.7 |
| 4 | 10/03/2006 9:38 AM | 48 hours | 24 hours | 7470.8 |
| 5 | 10/10/2006 3:25 PM | 48 hours | 24 hours | 7481.8 |
| 6 | 10/16/2006 3:51 PM | 48 hours | 24 hours | 7513.2 |
| 7 | 10/25/2006 3:12 PM | 48 hours | 24 hours | 8194.1 |
| 8 | 11/01/2006 4.11 PM | 48 hours | 24 hours | 6886.4 |
| 9 | 11/27/2006 8.12 AM | 48 hours | 24 hours | 8136.7 |
| 10 | 12/05/2006 2:36 PM | 48 hours | 24 hours | 8304.1 |
| 11 | 12/11/2006 3:19 PM | 48 hours | 24 hours | 7532.6 |
| 12 | 01/12/2007 3:06 PM | 48 hours | 24 hours | 7709.9 |
| 13 | 01/12/2007 3:29 PM | 48 hours | 24 hours | 7942.5 |
| | | | $\sum$ | 97972.3 |

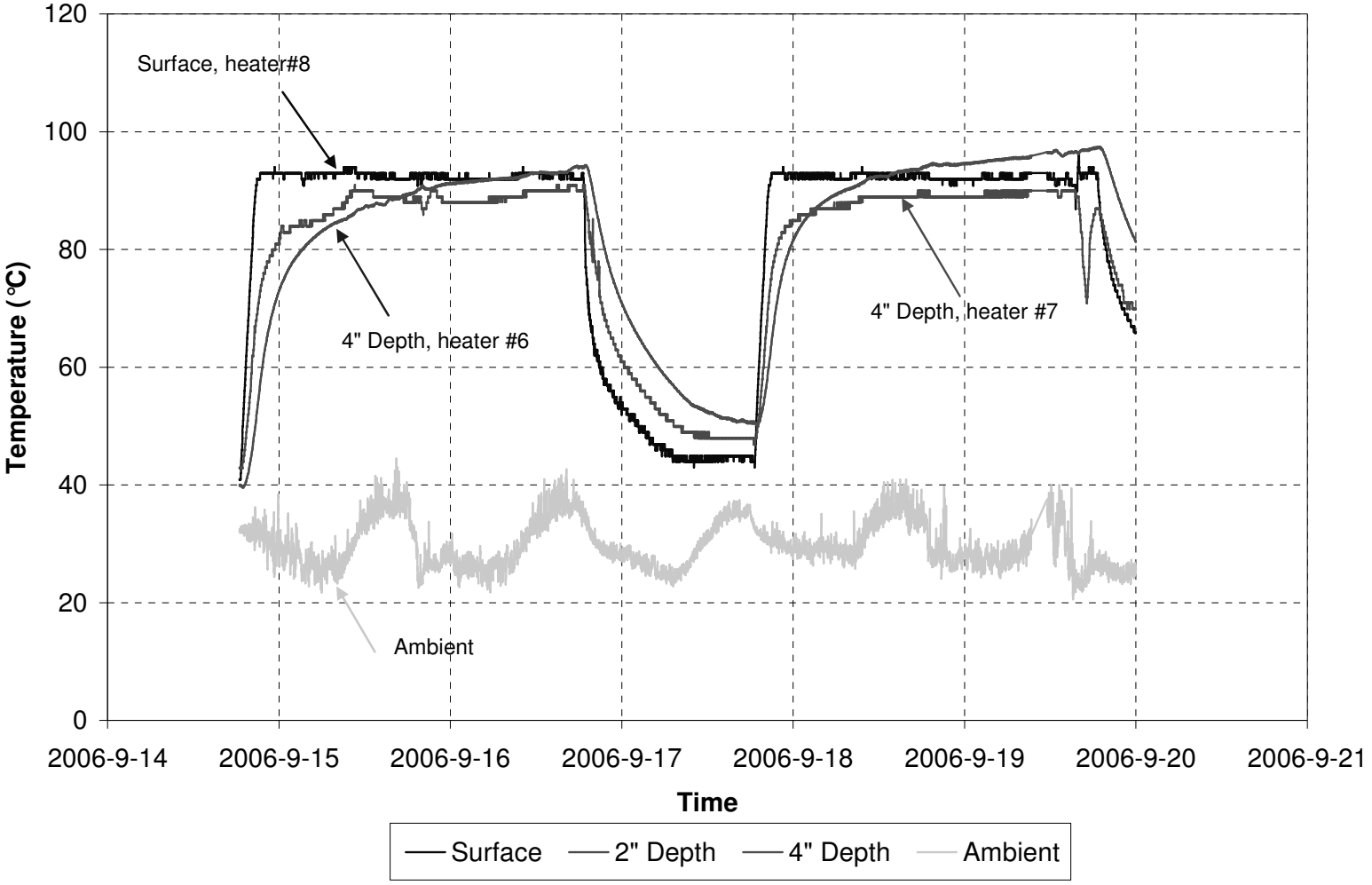


Figure 3.8 Typical Temperature Profiles in Section 1A

### 3.3.1 Binder Testing

Binder recovery and viscosity measurements performed on cores obtained from section 1A are presented in Figure 3.9.

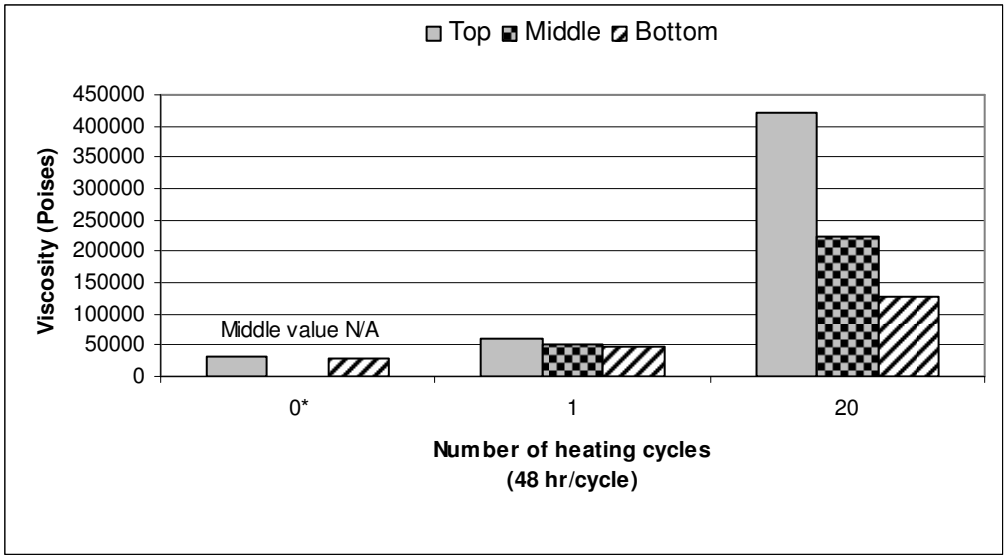


Figure 3.9 Recovered viscosity at different levels of aging at Section 1A

As can be seen, the aging levels induced in this section were about twice those induced in the previous sections (1C and 1B). These results also show that the APAS is able to effectively create a stiffness gradient through the asphalt concrete layer.

According to the lessons learned from the aging experiment in Sections 1C, 1B, and 1A; between two and three heating cycles (where one heating cycle consists of two consecutive days of heating followed by one day of rest) resulted in aging levels comparable to those observed in 10 to 20 year-old pavements in Florida. This is consistent with the Superpave LTOA protocol which uses 5 days of heating at 85˚C to achieve aging levels comparable to 5 to 10 years in the field.

# CHAPTER 4
# MIXTURE TESTS

As mentioned earlier in the report, the asphalt mixture at the site is a 90% Georgia granite and 10% local sand aggregate with a NMAS of 12.5 mm, and 4.6% PG 67-22 binder, produced December 2004. The asphalt layer thickness is about 6 inches.

Cores obtained before aging, between the aging cycles and after finalizing the artificial aging, were taken to the laboratory for testing in the Superpave Indirect Tension Test (IDT) and the results were evaluated with the University of Florida's HMA Fracture Mechanics Model (FMM). Table 4.1 gives a broad overview of the different phases of experiments carried out throughout the project.

Table 4.1 Overview of field and laboratory tests during the APAS project

<table>
<tr><td>Aging phase</td><td>Between aging and loading</td><td colspan="3">Loading phase</td></tr>
<tr><td>Temperature measurements</td><td></td><td>Temperature measurements</td><td></td><td></td></tr>
<tr><td rowspan="3">Asphalt cores before aging, between aging phases and after aging</td><td>IDT testing</td><td rowspan="3">HVS loading Strain measurements</td><td rowspan="3">Asphalt cores at different degrees of imposed damage</td><td>IDT testing</td></tr>
<tr><td>FMM calculation</td><td>FMM calculation</td></tr>
<tr><td>Binder recovery and viscosity measurements</td><td>Binder recovery and viscosity measurements</td></tr>
</table>

From the top and bottom, around 0.5" thick slices of the cores were removed, and around 1.5" thick slices were taken from each end of the remaining part of the cores, denoted "top" and "bottom" specimens, respectively. After IDT testing, these slices were subjected to binder recovery and viscosity measurements were made. In some cases, binder was also

recovered from the remaining middle part, even if this part was comprised of two asphalt lifts. This third slice was denoted “middle”.

Table 4.2 shows an overview of the measurements performed and cores taken on the APAS project.

Table 4.2 Overview of HVS measurements and accompanying coring and laboratory testing of asphalt specimens

| | HVS measurements 2006 | | | | Asphalt specimens | | | |
|---|---|---|---|---|---|---|---|---|
| Section | Phase | Performed | | # load repetitions | Coring date (#) = number of specimens | IDT testing | | Viscosity recovery |
| 1C | 1 | March 13 2005 | AM | 766 | April 28 (4) | June ‘05 To Aug ‘05 | Standard IDT/ER | Yes |
| | 2 | May 23–May 27 2005 | Night-time | 29960 | June 09 (3×3) (WP, WP edge, 17”) July 25 (1) (WP edge; replacem.) | | Standard IDT/ER | |
| | 3 | July 28–Aug. 14 2005 | All day | 205570 + conditioning | July 25 (3) (Far out) | | Shock cooling | |
| 1B | 1 | Aug. 23–Sept. 30 2006 | All day | 242134 w. 125453 no w. | Before aging (4) April 28 Between aging cycles After aging June 12 (3) | June ’06 to Dec ‘06 | Standard IDT/ER and Shock cooling | Yes |
| | | Oct.10–Oct.19 2006 | | 271849+ Conditioning (till Oct.19) | | | | |
| | 2 | Dec.5-Dec.16 2006 | | 732106+Conditioning (till Dec.16) | | | | |
| | | Jan.30-Feb.2 2007 | | 1,189,455+Conditioning (till Feb.2) | | | | |
| 1A | 1 | Feb.6-Mar.27 2007 | All day | 488,358 Aging (Northern) Non-Aged (Southern) | Before aging (4) Jun 2006 After aging (6) Jan 2007 | June ‘06 June ‘07 | Standard IDT/ER and damage susceptib. test | No |

## 4.1 Section 1C

All specimens from the aging phase were subjected to the "standard" set of IDT tests, and the results were interpreted according to the Fracture Mechanics Model developed at the University of Florida.

The location of the cores extracted is presented in the Figure 4.1.

The very first set of cores from Section 1C was tested with the FDOT MTS machine. It was later discovered that there was an issue with some of the extensometers for these measurements, and all later IDT testing in this project was carried out with the UF IDT device. Unfortunately, this initial measurement can therefore not be directly compared to the later results.

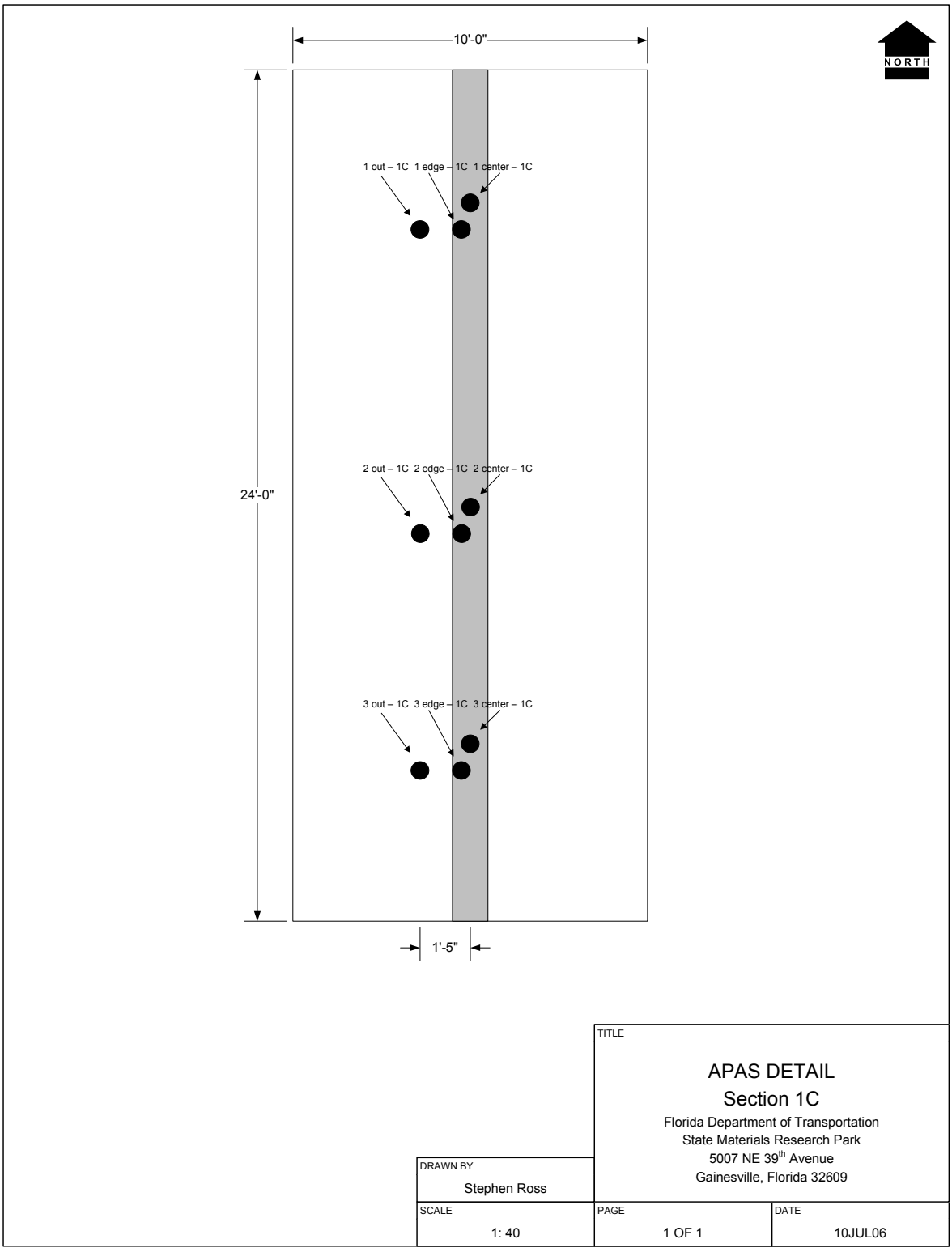


Figure 4.1. Location of cores obtained from Section 1C

Table 4.3 summarizes the IDT results from the aging process at Section 1C, while figure 4.2 shows the measured creep compliance values. It is clearly seen that the creep decreases significantly with increased aging, and for the top, with decreasing rate as more aging was imposed. The fact that the upper part shows lower compliance than the bottom before artificial aging began indicates that some natural aging took place between the time the pavement was constructed and the artificial aging started. However, as shown in figure 4.3, this is not reflected in significantly higher mixture stiffness for the top than the bottom specimen before artificial aging. Because the mixture stiffness reduces for the top specimen between three and six days of aging and even becomes lower than for the bottom part, the measured stiffness for the top specimen after six days of aging is questionable. Due to lower $DCSE_{min}$ but nearly unchanged $DCSE_{HMA}$ (and FE) with increased aging effort, the energy ratio (ER) increases with increasing aging as shown in figure 4.4, which indicates that other processes that reduce $DCSE_{HMA}$ may be in play in the field that were not induced by APAS.

Table 4.3 IDT test results for specimens taken during aging at Section 1C

| APAS 1C | | m-value | $D_1$ ($psi^{-1}$) | Creep rate @ 1000 s | $S_t$ (MPa) | $M_R$ (GPa) | FE ($kJ/m^3$) | $DCSE_{HMA}$ ($kJ/m^3$) | Stress (psi) | a | $DCSE_{MIN}$ ($kJ/m^3$) | ER |
|---|---|---|---|---|---|---|---|---|---|---|---|---|
| Day 0 | Top | 0.531 | 8.66E-07 | 1.801E-08 | 1.67 | 9.60 | 1.6 | 1.5 | 150 | 5.07E-08 | 2.591 | 0.56 |
| | Bot | 0.504 | 1.42E-06 | 2.326E-08 | 1.67 | 9.43 | 2.3 | 2.2 | 150 | 5.07E-08 | 3.627 | 0.59 |
| Day 3 | Top | 0.512 | 5.72E-07 | 1.006E-08 | 1.81 | 11.37 | 1.8 | 1.7 | 150 | 5.00E-08 | 1.558 | 1.06 |
| | Bot | 0.533 | 9.44E-07 | 1.998E-08 | 1.74 | 8.91 | 2.8 | 2.6 | 150 | 5.04E-08 | 2.881 | 0.91 |
| Day 6 | Top | 0.482 | 5.61E-07 | 7.551E-09 | 1.72 | 11.28 | 1.6 | 1.5 | 150 | 5.05E-08 | 1.266 | 1.16 |
| | Bot | 0.491 | 7.28E-07 | 1.062E-08 | 1.95 | 12.75 | 2.2 | 2.1 | 150 | 4.92E-08 | 1.781 | 1.15 |

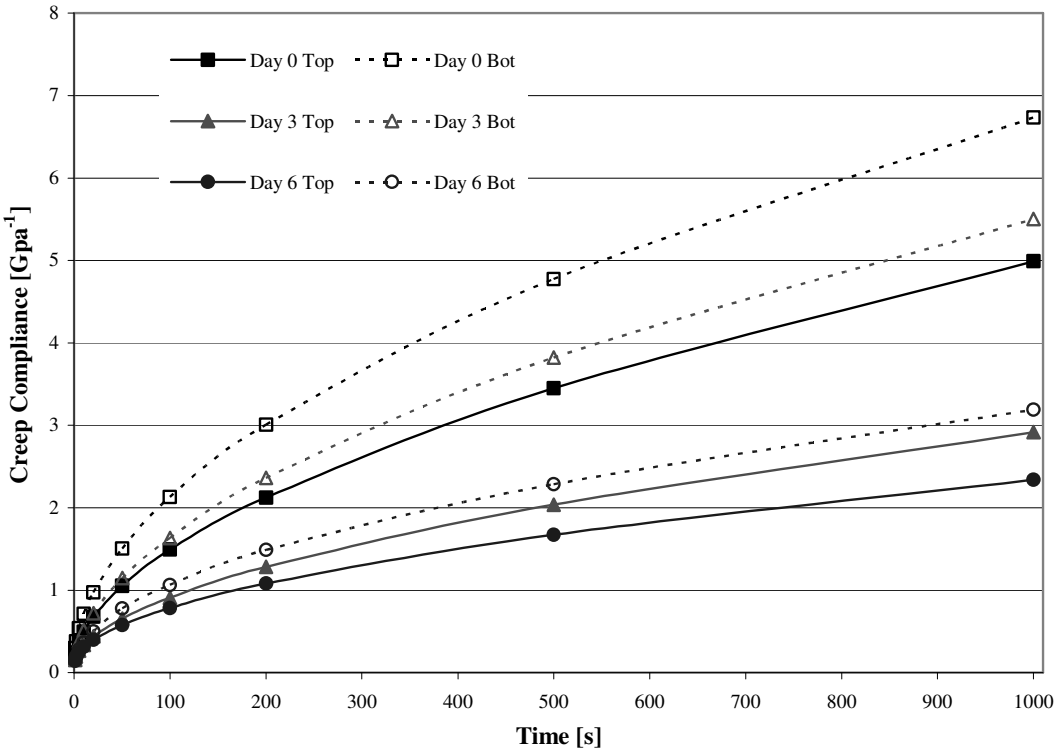


Figure 4.2 Creep compliance values for specimens from cores taken before and during aging process at Section 1C

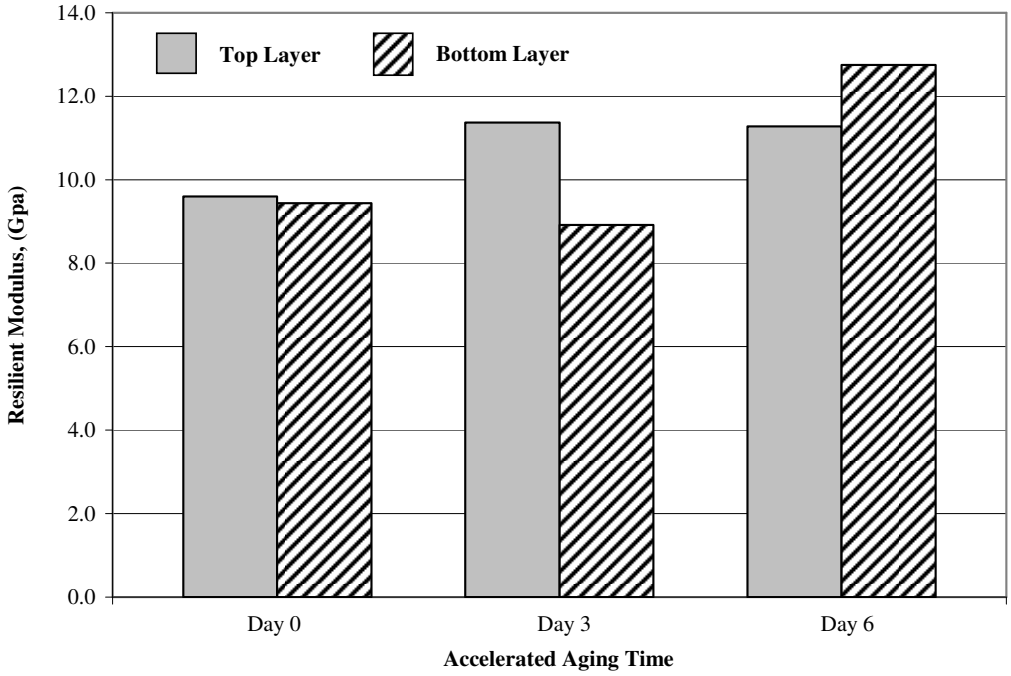


Figure 4.3 Mixture stiffness at different levels of aging at Section 1C

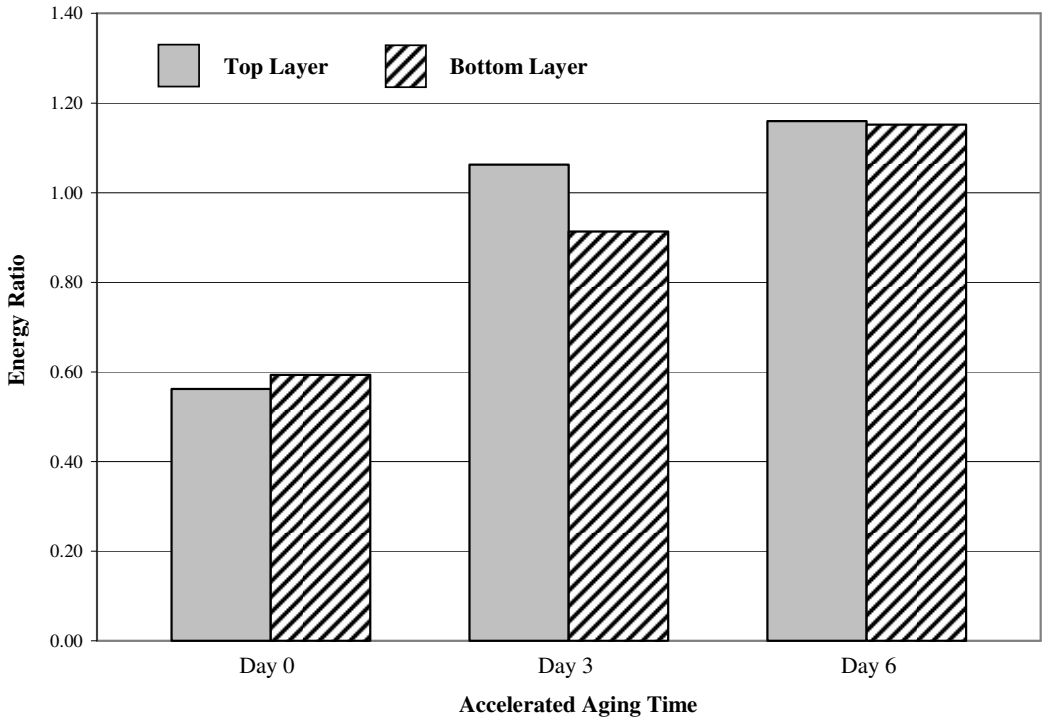


Figure 4.4 Energy ratio different levels of aging at Section 1C

## 4.2 Section 1B

The location of the cores extracted from Section B is shown in the Figure 4.5.

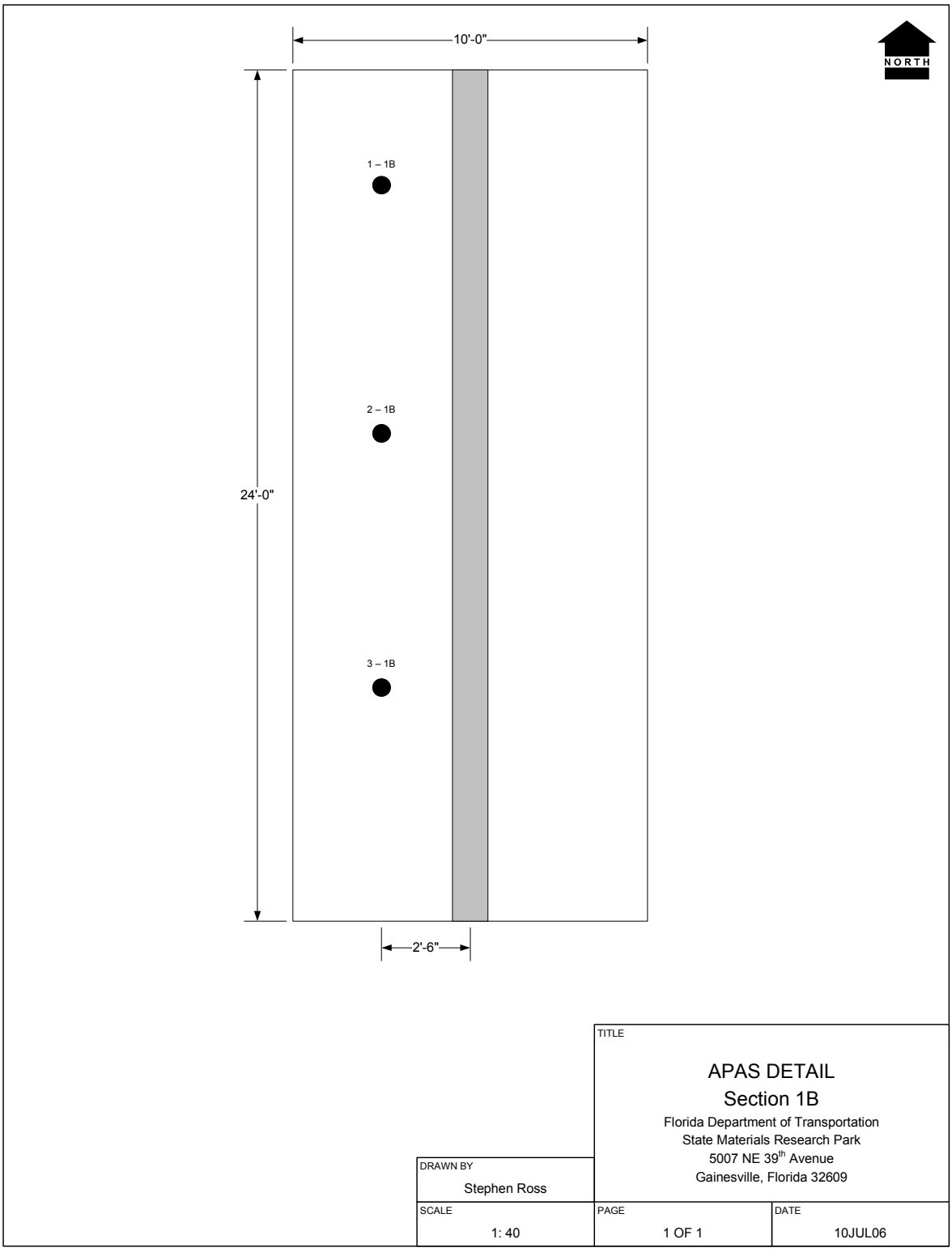


Figure 4.5 Location of the cores taken from Section 1B.

The artificial aging on Section 1B included four weekly heating stages during September-October 2005 at 90°C, each consisting of two two-day cycles with a one-day break between. Cores were extracted before the aging started and after each of the four stages; Week 0 (initial values), Week 1 (after one week of heating), Week 2 (after two weeks of heating), Week 3 (after three weeks of heating), and Week 4 (after four weeks of heating). Four cores were taken each time, three of which were used for testing, while the fourth specimen was retained for back-up purposes.

Table 4.4 summarizes the IDT results from the aging process at Section 1B, including the specimens from the cores taken April '06. Figure 4.6 shows the creep compliance results for the latter, while figures 4.7 to 4.9 show some of the key parameters for the all the specimens. The labels "0", "1", "2" and so on represent the aging cycles. Figures 4.10 to 4.15 express some parameters somewhat differently, with manual trend lines included. In addition, other sets of specimens were taken at both Section 1C and Section 1B to obtain a reference before phase 2 of the HVS measurements at Section 1C started. This was considered necessary to check whether the relatively hot Florida climate had induced any additional aging between the time when the last specimens at Section 1C were taken in May 2005 and April 2006. These last specimens are marked "5" in the following graphs.

Table 4.4 IDT test results at 10C for specimens taken during aging and April '06 at Section 1B

| APAS 1B | | m-value | $D_1$ ($psi^{-1}$) | Creep rate @ 1000 s | $S_t$ (MPa) | $M_R$ (GPa) | FE ($kJ/m^3$) | $DCSE_{HMA}$ ($kJ/m^3$) | Failure strain | ER |
|---|---|---|---|---|---|---|---|---|---|---|
| Cycle 0 | Top | 0.522 | 5.50E-07 | 1.05E-08 | 1.87 | 10.83 | 1.4 | 1.2 | 1063.03 | 0.78 |
| | Bot | 0.570 | 5.33E-07 | 1.56E-08 | 2.00 | 9.54 | 2.4 | 2.2 | 1454.64 | 1.07 |
| Cycle 1 | Top | 0.714 | 1.00E-07 | 9.89E-09 | 2.08 | 15.29 | 0.9 | 0.8 | 664.94 | 1.00 |
| | Bot | 0.604 | 3.29E-07 | 1.29E-08 | 1.74 | 9.33 | 1.7 | 1.5 | 1307.13 | 1.06 |
| Cycle 2 | Top | 0.482 | 2.48E-07 | 3.32E-09 | 2.37 | 13.71 | 1.4 | 1.2 | 889.25 | 1.99 |
| | Bot | 0.547 | 3.76E-07 | 8.97E-09 | 2.11 | 11.35 | 1.8 | 1.6 | 1205.40 | 1.25 |
| Cycle 3 | Top | 0.411 | 3.12E-07 | 2.20E-09 | 2.38 | 13.84 | 1.4 | 1.2 | 859.99 | 2.53 |
| | Bot | 0.504 | 6.08E-07 | 9.92E-09 | 1.74 | 10.3 | 1.0 | 0.9 | 863.54 | 0.55 |
| Cycle 4 | Top | 0.518 | 1.36E-07 | 2.53E-09 | 2.23 | 14.63 | 0.9 | 0.7 | 606.76 | 1.81 |
| | Bot | 0.444 | 5.21E-07 | 4.97E-09 | 1.89 | 11.53 | 1.1 | 0.9 | 861.32 | 1.01 |
| April '06 | Top | 0.518 | 1.43E-07 | 2.66E-09 | 2.61 | 14.54 | 1.5 | 1.3 | 834.72 | 2.90 |
| | Bot | 0.483 | 4.59E-07 | 6.26E-09 | 1.45 | 11.65 | 0.5 | 0.4 | 571.60 | 0.40 |

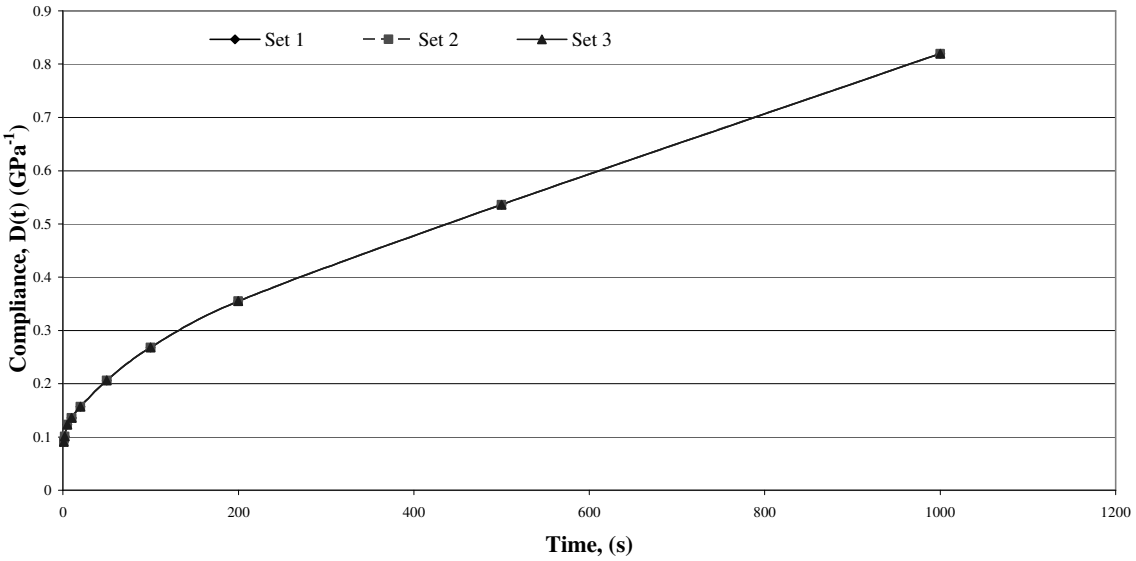


Figure 4.6 Creep compliance at 10C for top layer specimens taken April '06 at Section 1B

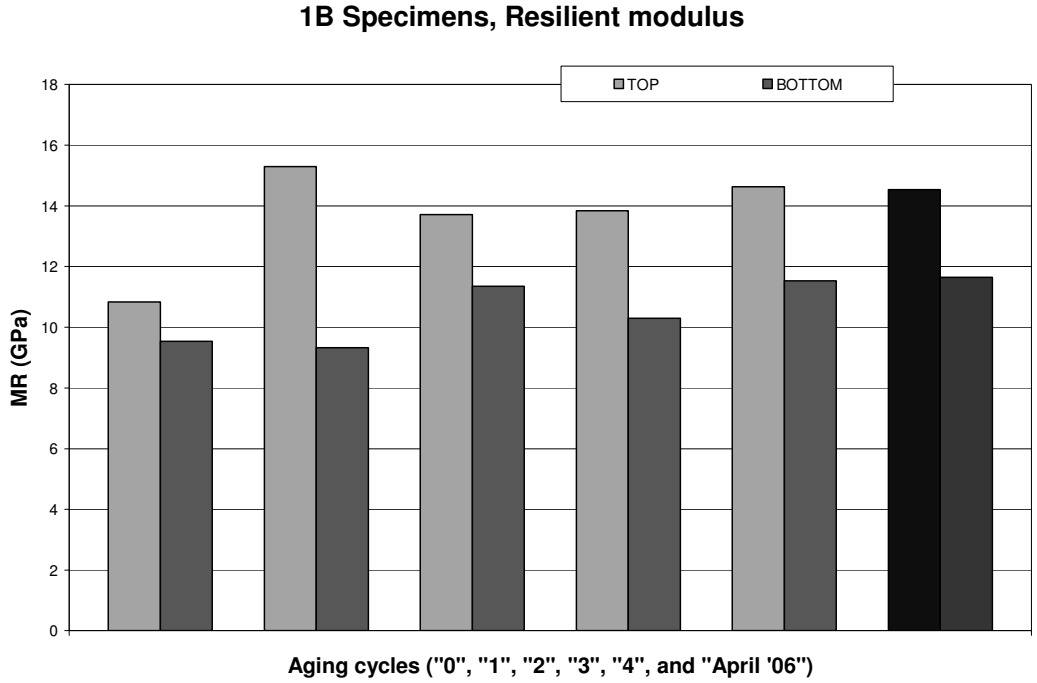


Figure 4.7 Mixture stiffness at 10C for specimens from cores taken at different levels of aging at Section 1B

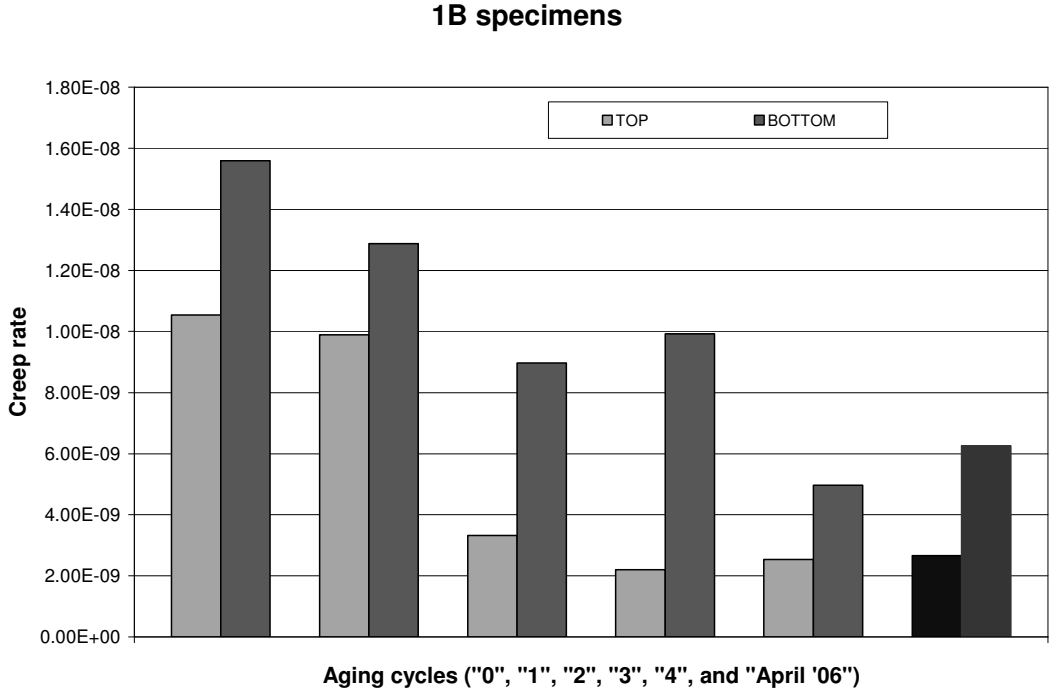


Figure 4.8 Creep rate at 1000 s for specimens from cores taken at different levels of aging at Section 1B

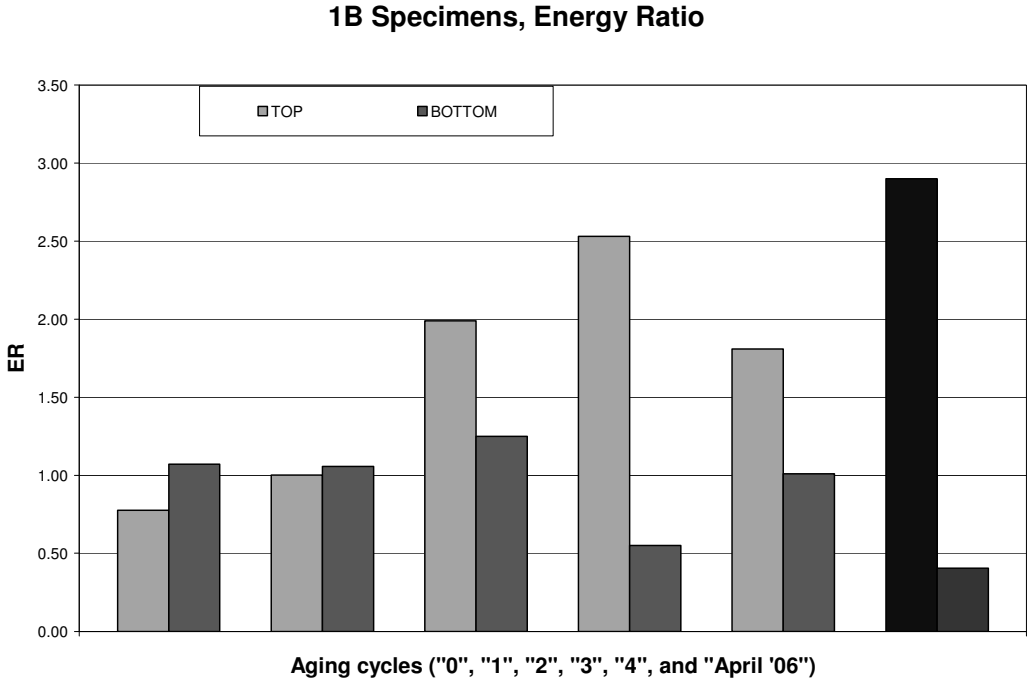


Figure 4.9 Energy Ratio for specimens from cores taken at different levels of aging at Section 1B

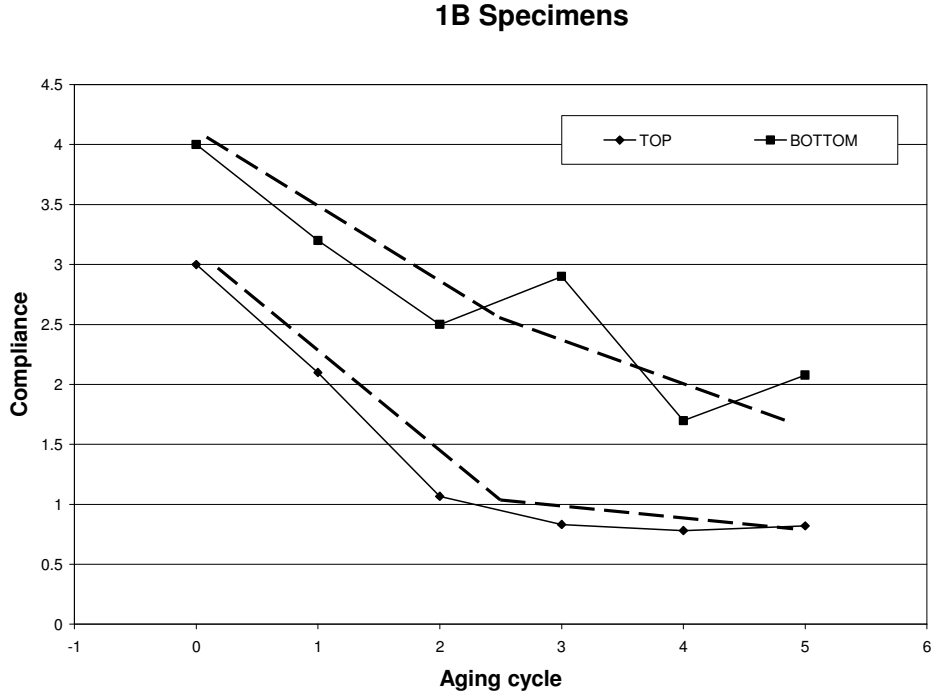


Figure 4.10 Creep compliance @ 1000 s for specimens from cores taken at different levels of aging at Section 1B

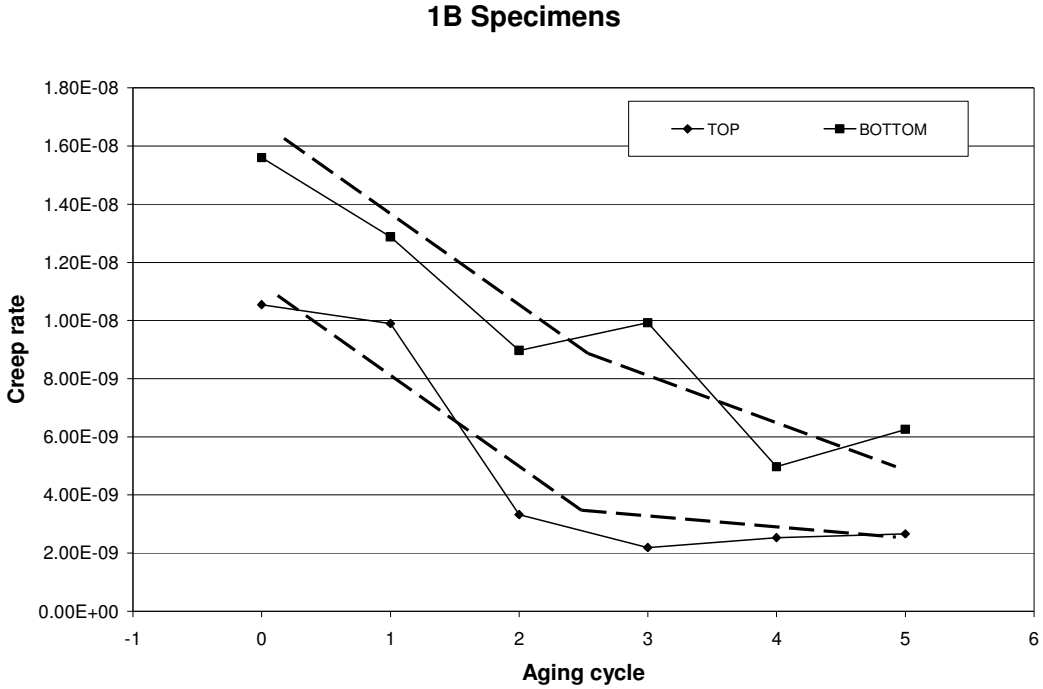


Figure 4.11 Creep Rate @ 1000 s for specimens from cores taken at different levels of aging at Section 1B

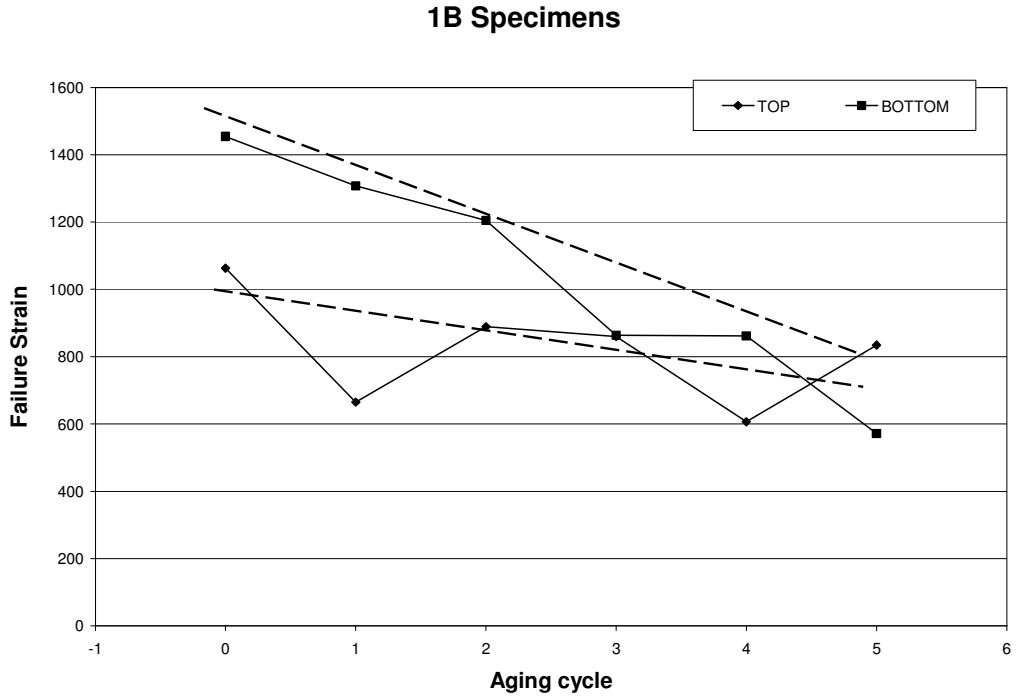


Figure 4.12 Failure Strain for specimens from cores taken at different levels of aging at Section 1B

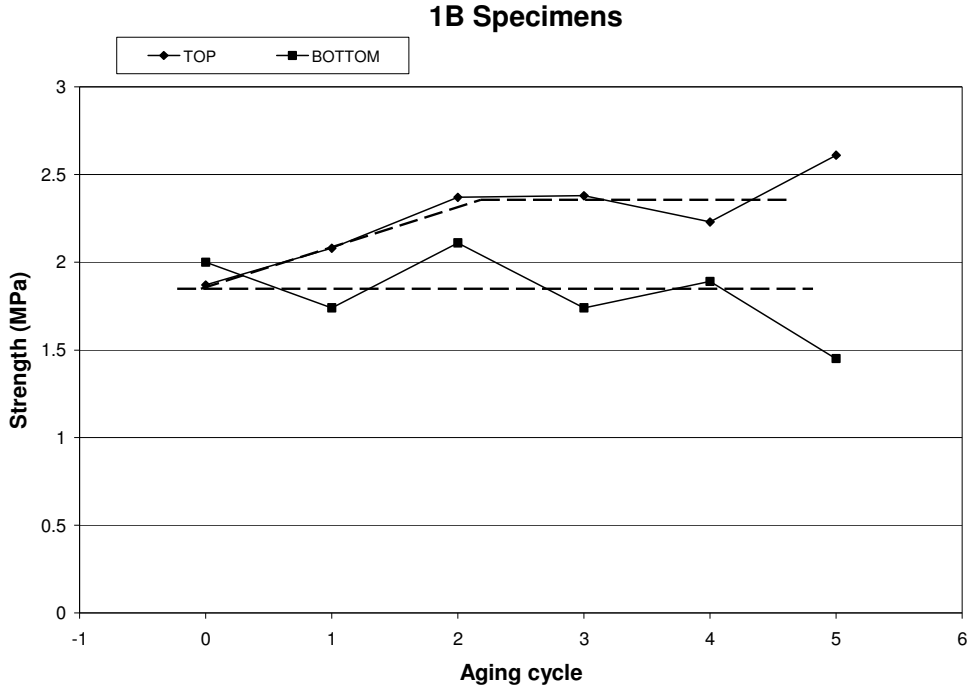


Figure 4.13 Failure strength for specimens from cores taken at different levels of aging at Section 1B

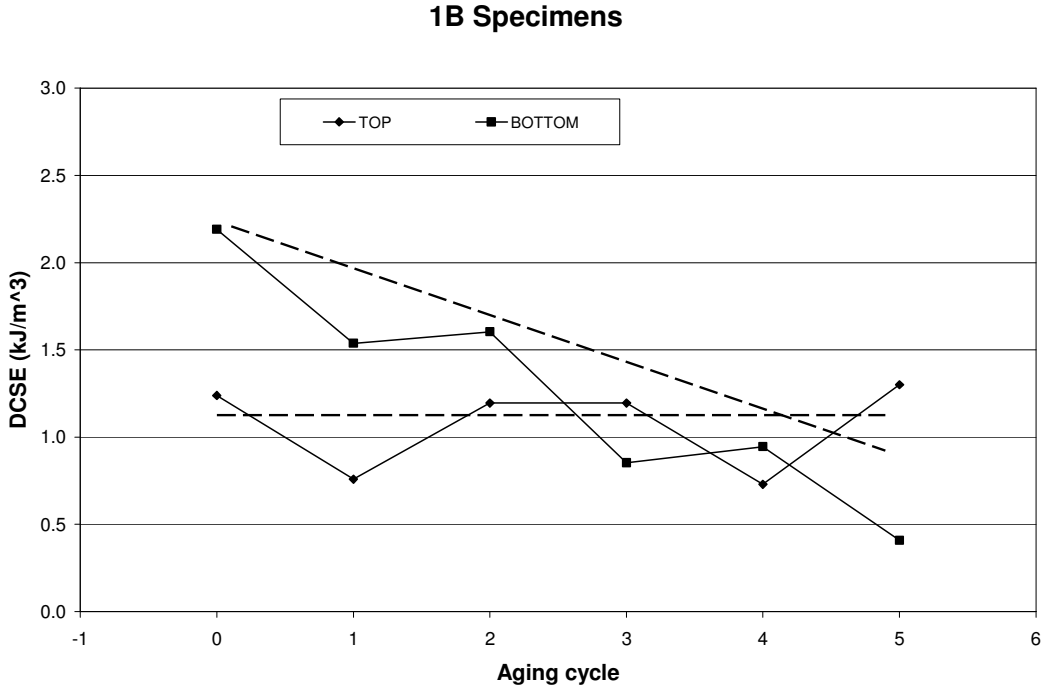


Figure 4.14 Dissipated creep strain energy for specimens from cores taken at different levels of aging at Section 1B

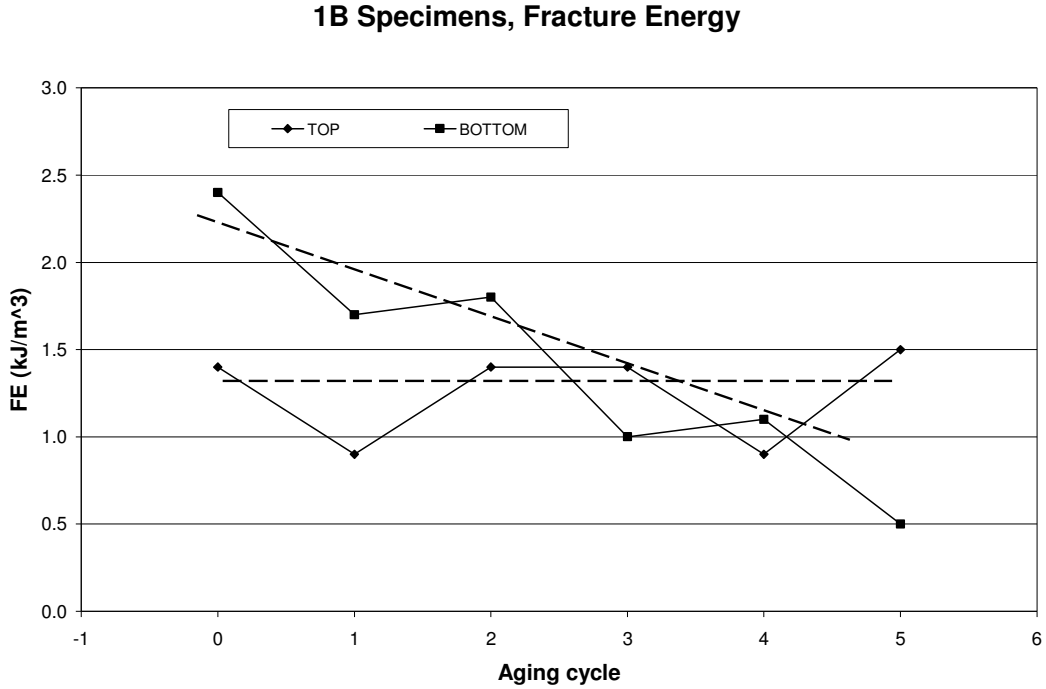


Figure 4.15 Fracture energy for specimens from cores taken at different levels of aging at Section 1B

### 4.3 Section 1A

The location of the cores taken from Section 1A is presented in the Figure 4.16. Table 4.5 summarizes the IDT results from Section 1A, including the specimens before aging and after approximately four months of aging. Figures 4.17 to 4.23 show some of the IDT parameters from section 1A before and after aging.

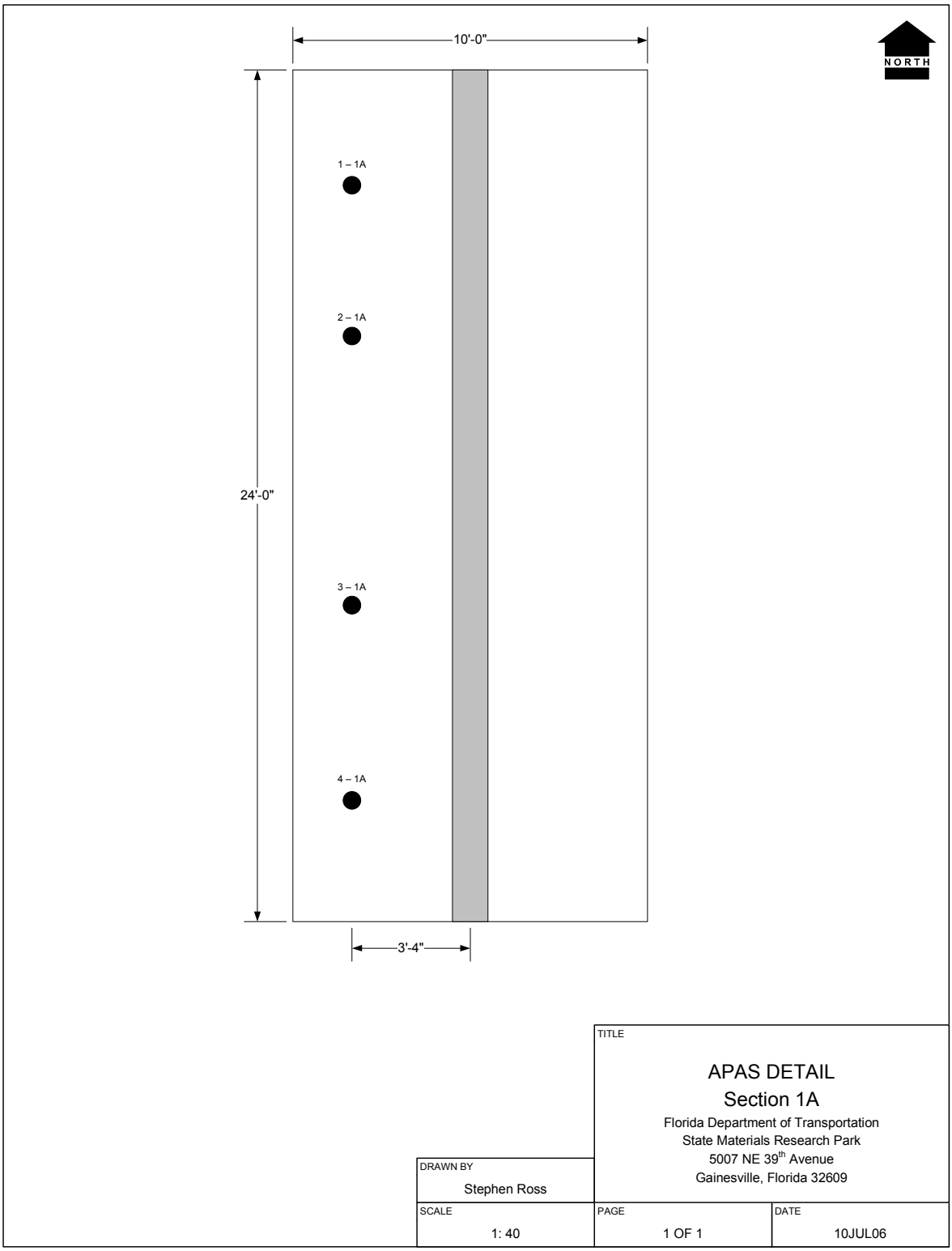


Figure 4.16 Location of the cores taken from Section 1A

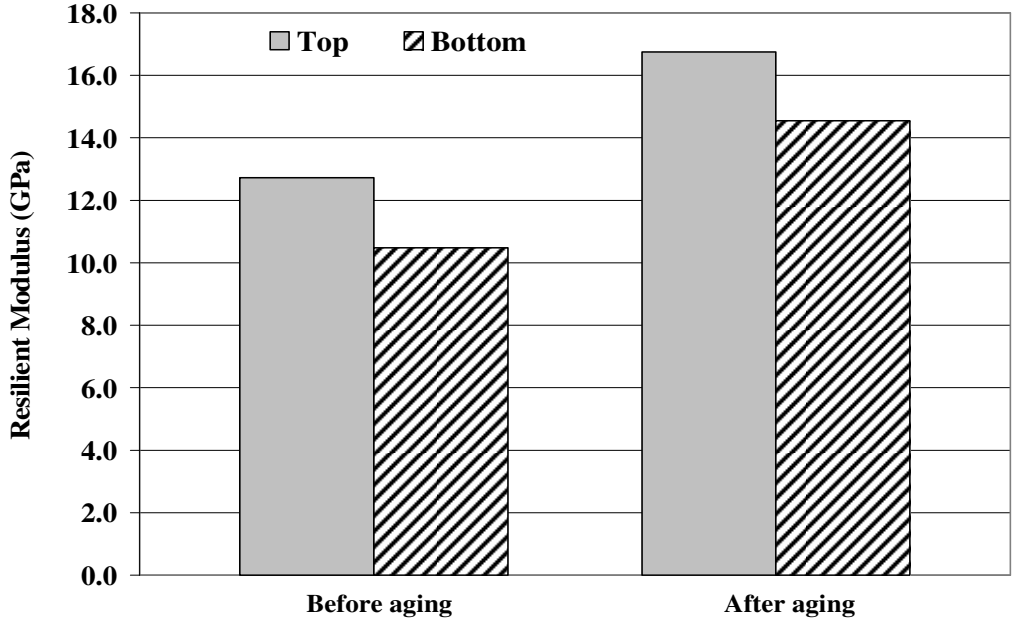


Figure 4.17 Resilient modulus for Section 1A

Table 4.5 IDT test results for Section 1A

| APAS | | m-value | $D_1$ | Creep compliance at 1000 sec | Creep rate 1/GPa | $S_t$ | $M_R$ | Failure Strain | FE | $DCSE_{HMA}$ | ER |
|---|---|---|---|---|---|---|---|---|---|---|---|
| Unaged | Top | 0.491 | 4.90E-07 | 2.15 | 7.13E-09 | 2.62 | 12.7 | 1434.5 | 2.7 | 2.4 | 1.88 |
| | Bottom | 0.537 | 5.43E-07 | 3.27 | 1.19E-08 | 2.17 | 10.5 | 1505.6 | 2.4 | 2.2 | 1.22 |
| Aged | Top | 0.355 | 1.40E-07 | 0.29 | 5.74E-10 | 2.62 | 16.7 | 597.4 | 1.0 | 0.8 | 5.68 |
| | Bottom | 0.377 | 4.16E-07 | 0.88 | 2.12E-09 | 2.07 | 14.5 | 811.8 | 1.1 | 1.0 | 2.03 |

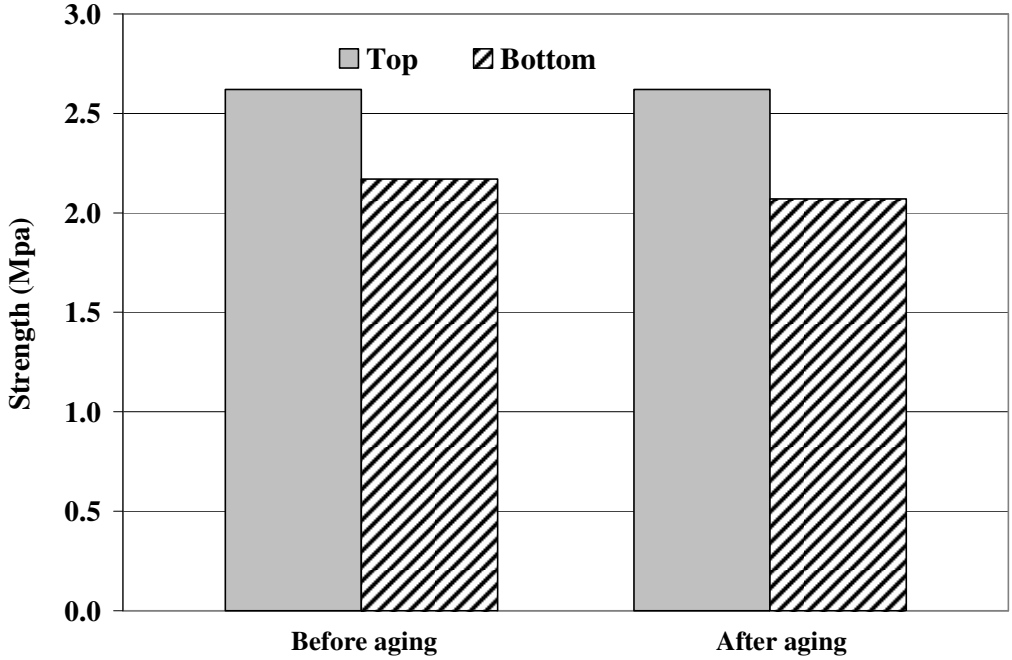


Figure 4.18 Strength for Section 1A

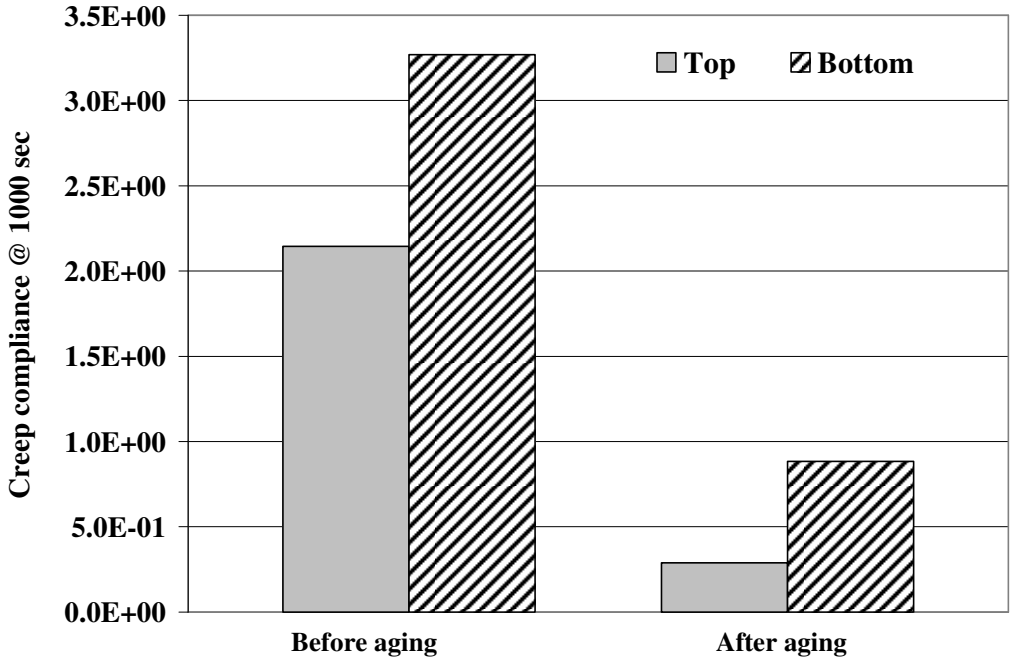


Figure 4.19 Creep compliance at 1000 sec for Section 1A

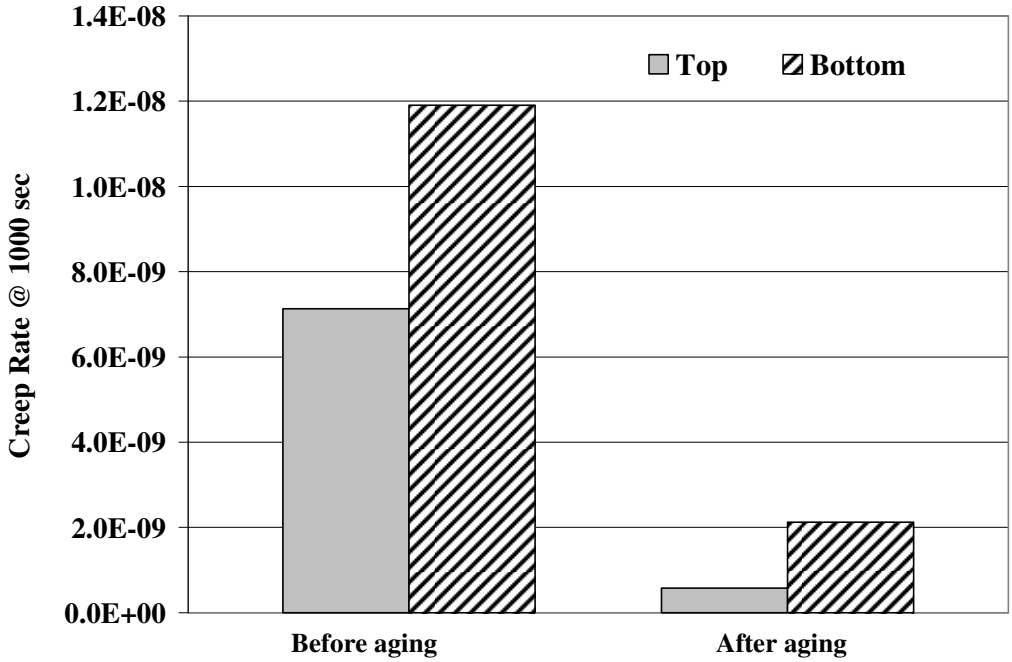


Figure 4.20 Creep rate @ 1000 sec for Section 1A

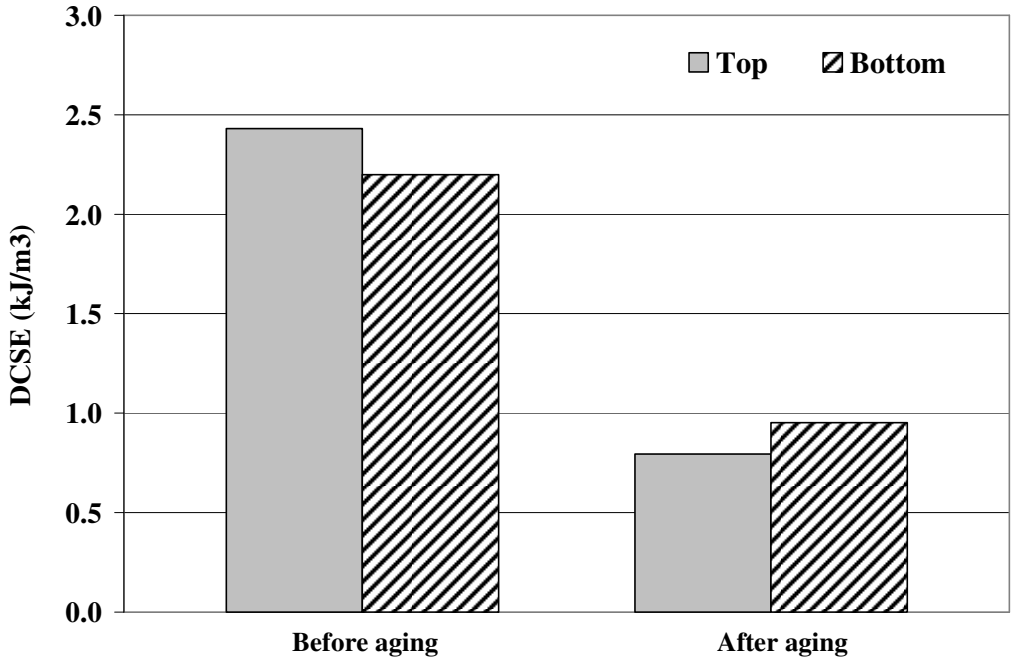


Figure 4.21 DCSE for Section 1A

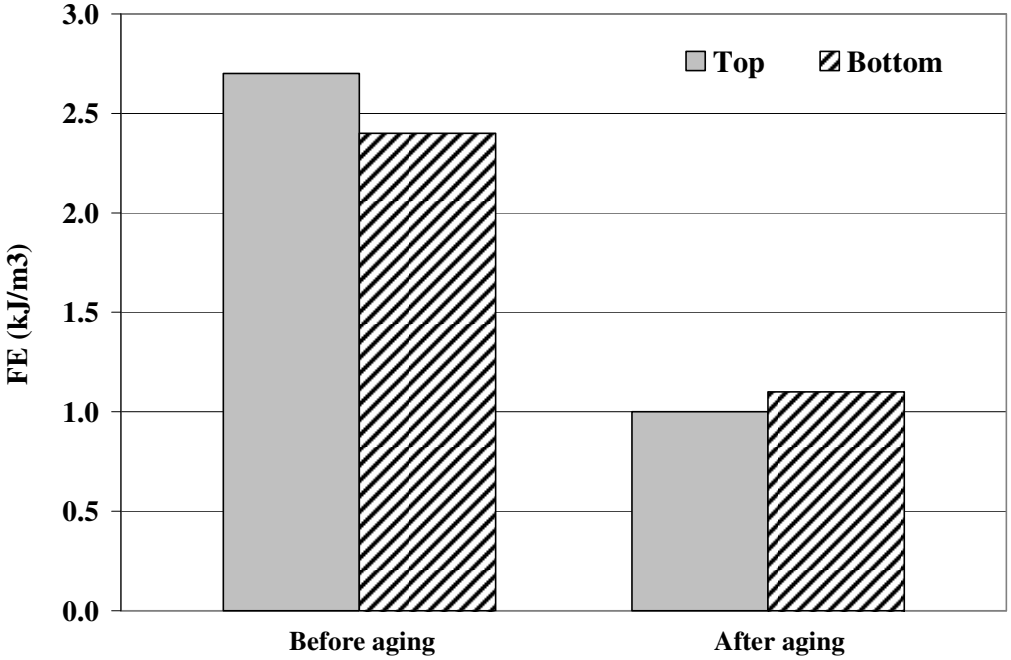


Figure 4.22 Fracture Energy for Section 1A

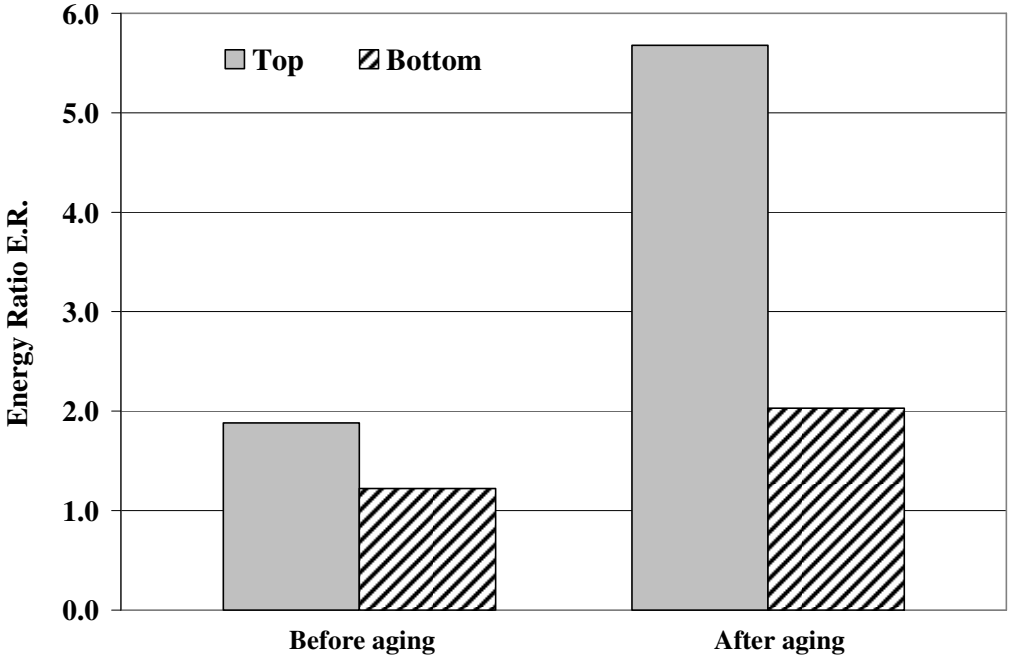


Figure 4.23 Energy Ratio for Section 1A

Both creep rate and failure strain reduction after aging indicates that Section 1A was also successfully aged by APAS; as this section was the only one that exhibited cracking, further analyses were performed in order to determine why cracking ocurred.

Therefore, in addition to the standard IDT Superpave procedure at 10°C; creep compliance curves were measured at 0°C, 10°C, and 20°C in order to obtain master curves. These master curves were incorporated in the calculations presented in the chapter 6: Theoretical Analysis. Table 4.6 and Figures 4.24 and 4.25 show the creep compliance values obtained.

Table 4.6 Section 1A Creep compliance values at 0C, 10C and 20C

| | **TOP** | | | **BOTTOM** | | |
|---|---|---|---|---|---|---|
| **TIME (SEC)** | **0C** | **10C** | **20C** | **0C** | **10C** | **20C** |
| **1** | 0.054 | 0.069 | 0.129 | 0.076 | 0.126 | 0.248 |
| **2** | 0.059 | 0.075 | 0.152 | 0.076 | 0.145 | 0.296 |
| **5** | 0.057 | 0.084 | 0.169 | 0.096 | 0.171 | 0.379 |
| **10** | 0.059 | 0.096 | 0.196 | 0.098 | 0.198 | 0.443 |
| **20** | 0.065 | 0.114 | 0.262 | 0.111 | 0.257 | 0.503 |
| **50** | 0.085 | 0.126 | 0.328 | 0.127 | 0.296 | 0.828 |
| **100** | 0.092 | 0.148 | 0.425 | 0.136 | 0.378 | 1.154 |
| **200** | 0.095 | 0.176 | 0.597 | 0.146 | 0.471 | 1.607 |
| **500** | 0.109 | 0.238 | 0.873 | 0.162 | 0.669 | 2.484 |
| **1000** | 0.110 | 0.282 | 1.168 | 0.160 | 0.884 | 3.443 |

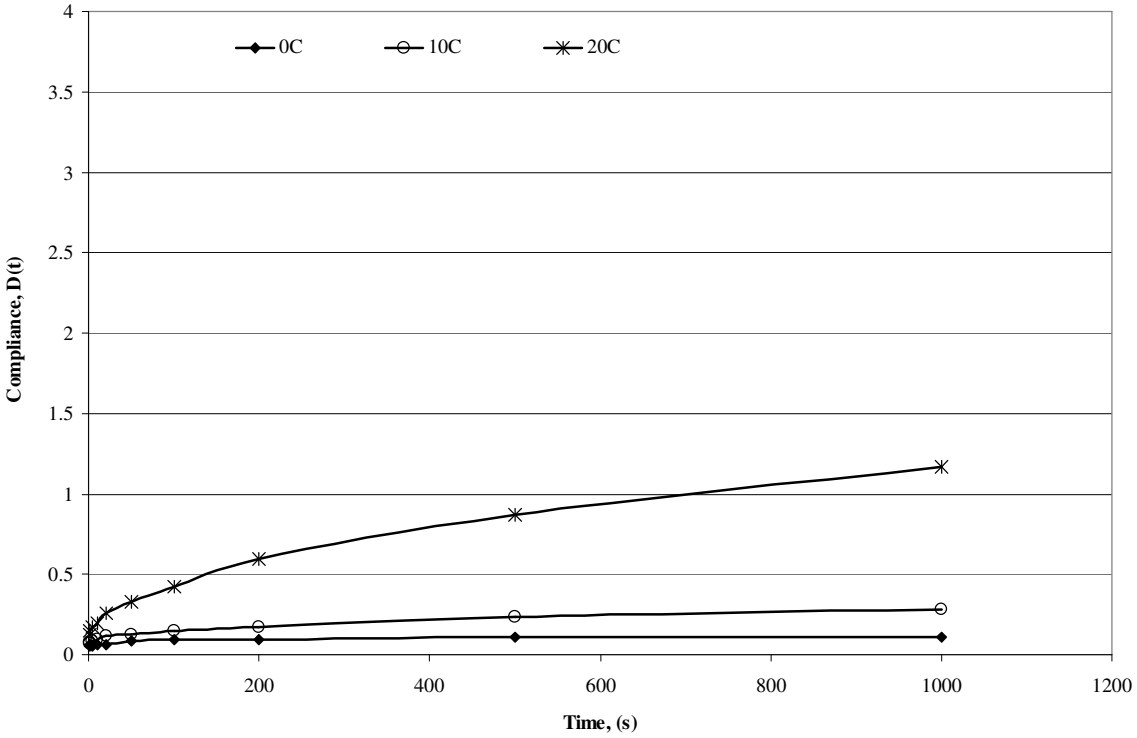


Figure 4.24 Creep Compliance for aged samples taken from top Section 1A

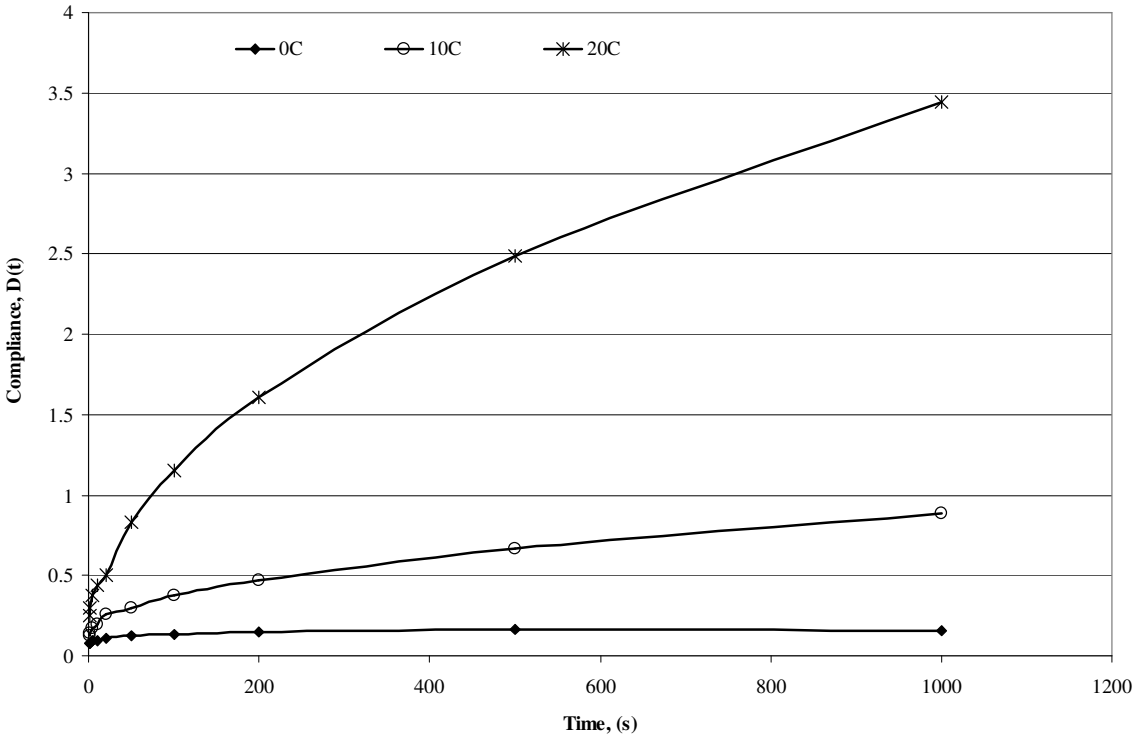


Figure 4.25 Creep Compliance for aged samples taken from bottom Section 1A

## 4.4 Additional tests

### 4.4.1 Thermal Shock Cooling Test

Some of the specimens collected at Section 1C and 1B were subjected to shock cooling in the laboratory before IDT testing to reveal if such a procedure was capable of simulating possible damage development during loading. Quite some effort was expended to plan and prepare this procedure. The idea was to have two baths, one at -20ºC and one at 25ºC. Specimens were kept in sealed bags to prevent water from penetrating into the specimens in the 25ºC bath. After tempering at 25ºC, the specimens were taken to the -20C bath and kept there until the temperature stabilized, and then taken back to the 25ºC bath. This transferring between the baths was repeated several times. After the last soaking in the -20ºC bath, the specimen was taken to the 10ºC air chamber to be prepared for the IDT testing. The main goal here was to assure that any damage induced in the specimen by contraction of the binder and possibly loss of adhesion between binder and aggregate, would not heal by maintaining the temperature as low as possible prior to testing.

The “Aged” values are from specimens taken April 2006. Section 1C had experienced 750 load repetitions. At that time, 1B had not been subjected to any load applications. After tests on Sections B and C were completed, the output files were evaluated with the HMA Fracture mechanics model developed by the University of Florida. The results are shown in the table 4.7. Figures 4.26 to 4.29 show some of the IDT parameters before and after shock cooling.

Table 4.7 Shock-cooling IDT results (Section 1B and 1C)

| | APAS | m-value | $D_1$ | $S_t$ (Mpa) | $M_R$ (Gpa) | FE ($kJ/m^3$) | $DCSE_{HMA}$ ($kJ/m^3$) | ER @ 150 PSI |
|---|---|---|---|---|---|---|---|---|
| **Aged Sections-After week 4 of aging** | SECTION B TOP | 0.518 | 1.43E-07 | 2.61 | 14.54 | 1.5 | 1.27 | 2.85 |
| | SECTION B BOTTOM | 0.483 | 4.59E-07 | 1.45 | 11.65 | 0.5 | 0.41 | 0.40 |
| | SECTION C TOP | 0.476 | 4.63E-07 | 2.23 | 11.19 | 2.3 | 2.08 | 1.95 |
| | SECTION C BOTTOM | 0.537 | 6.10E-07 | 1.98 | 10.03 | 2.4 | 2.20 | 1.13 |
| **Shock Cooling** | SECTION B TOP | 0.375 | 3.18E-07 | 2.8 | 11.99 | 1.8 | 1.47 | 3.82 |
| | SECTION B BOTTOM | 0.399 | 7.14E-07 | 2.12 | 10.09 | 1.4 | 1.18 | 1.23 |
| | SECTION C TOP | 0.427 | 5.36E-07 | 2.39 | 12.37 | 1.8 | 1.57 | 1.73 |
| | SECTION C BOTTOM | 0.485 | 6.49E-07 | 2.19 | 11.13 | 2.0 | 1.78 | 1.14 |


Figure 4.26 Resilient modulus values.

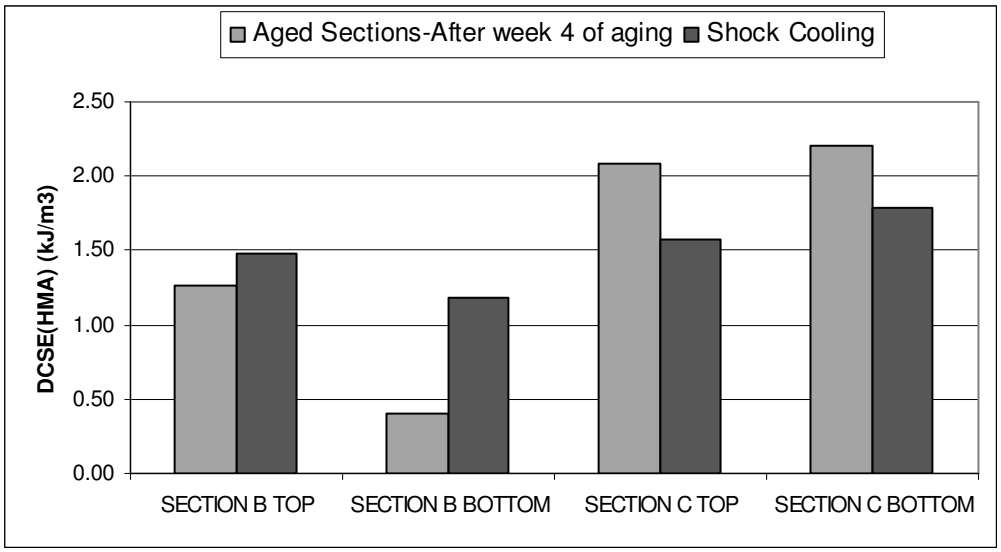


Figure 4.27 DCSE values.

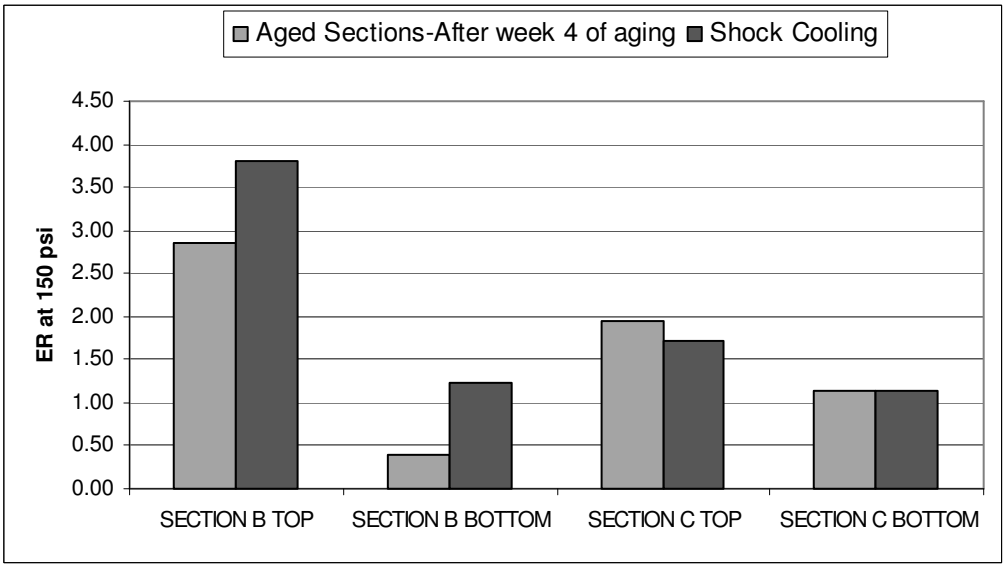


Figure 4.28 Energy ratio

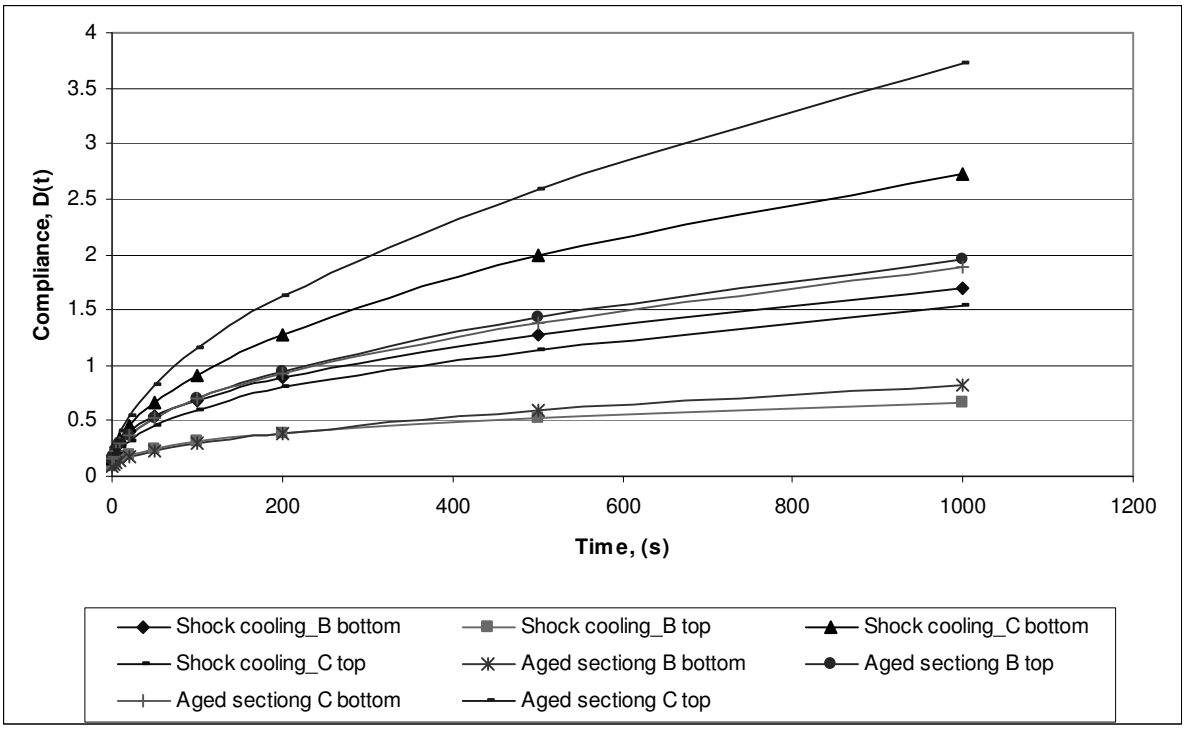


Figure 4.29 Creep compliance curves (Aging vs. Shock cooling).

Resilient modulus was expected to decrease after shock cooling process; but 1C section samples did not follow this trend. It was also difficult to draw any conclusion from the other IDT results obtained. In conclusion, the specimens may have experienced some healing throughout the test; therefore additional research is needed to fine-tune different aspects of the proposed procedure.

### 4.4.2 Determination of pavement damage susceptibility

Over the last seven years, a variety of tests and studies have been conducted at the University of Florida to determine the healing properties of asphalt mixtures. For this experiment, specimens prepared for IDT testing were subjected to repeated loads, a haversine waveform of 0.1 seconds duration followed by a 0.9 second rest period. (This is the same load configuration typically used for the Resilient Modulus test.) In terms of permanent strain, the resulting specimen response is similar to that obtained from the static creep test.

The load was repeated for thousands of cycles, and it was determined that as long as the specimen did not reach a specific failure criterion, the specimen would completely heal.

This research also investigated the change in stiffness of these specimens with respect to time. It was shown that the Modulus or stiffness of the specimens did not change, indicating that the specimens were not being damaged by the application of these load pulses. Therefore, if a single stress or multiple stresses are applied to a specimen that do not result in a strain high enough to induce damage, the stiffness of the specimen or material will remain the same.

A similar test procedure, to that already described, was written for UF's MTS test system to test the specimens taken from the HVS sections. The procedure applied a predetermined stress, calculated to simulate the stress applied by the HVS, and then recorded the specimen's response. Load pulses were continuously applied during the tests. At any chosen time during the test, the operator can record seven load pulses and the associated vertical and horizontal deformations and store them for future analysis to determine whether or not the Modulus or stiffness of the specimen is decreasing throughout the test.

The samples used for this experiment were obtained from section 1B; they were taken from the area of maximum compaction in the APAS heated zone. The following graphs and figures are from samples taken from the HVS test sections and tested at UF using this procedure.

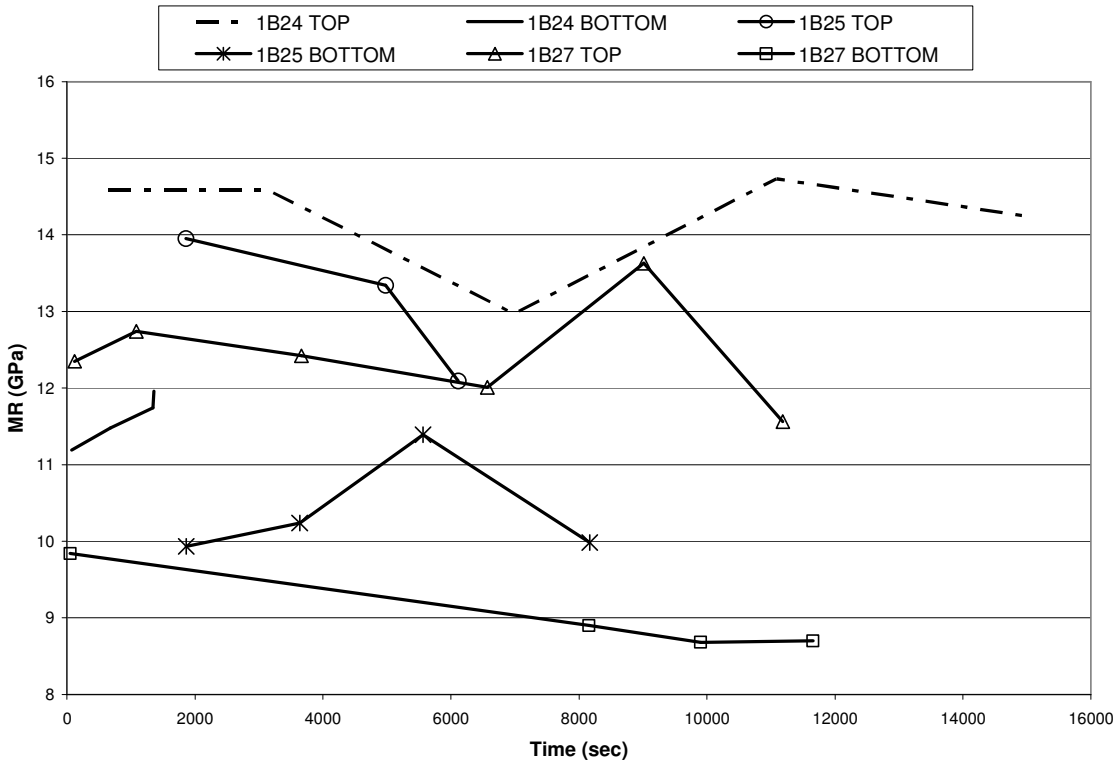


Figure 4.30 Resilient modulus (Damage susceptibility test)

According to the figure 4.34, resilient modulus appears to be relatively constant through the experiment; in other words, either little or no damage seems to be induced to the samples or healing may be occurring during the test. Additional research is needed to better understand this process.

# CHAPTER 5
# NON-DESTRUCTIVE TESTING

Falling Weight Deflectometer FWD tests were performed to determine pavement materials properties; also several systems were evaluated as potential candidates to detect age-hardening and cracking in the APT facility, including impact-echo, Spectral Analysis Of Surface Waves (SASW), and electrical resistivity. Results of these activities are presented in the following sections.

## 5.1 Falling Weight Deflectometer FWD

In order to determine layer moduli in situ, FWD backcalculation analysis was performed with the BISDEF computer program. BISDEF was developed to handle multiple loads and to consider different interface layer conditions [Bush and Alexander 1985]. To determine the modulus values, the pavement system is modeled as a layered system. Roque et al. [1992, 1997 and 2003] has shown that elastic layer analysis provides reasonably accurate predictions of load induced strains in the HMA surface layer.

One or two representative FWD deflection basins were selected for analysis; these were selected visually as the middle of deflection basins from locations exhibiting similar response. Figure 5.1 shows typical match of deflection basin between measured and calculated values.

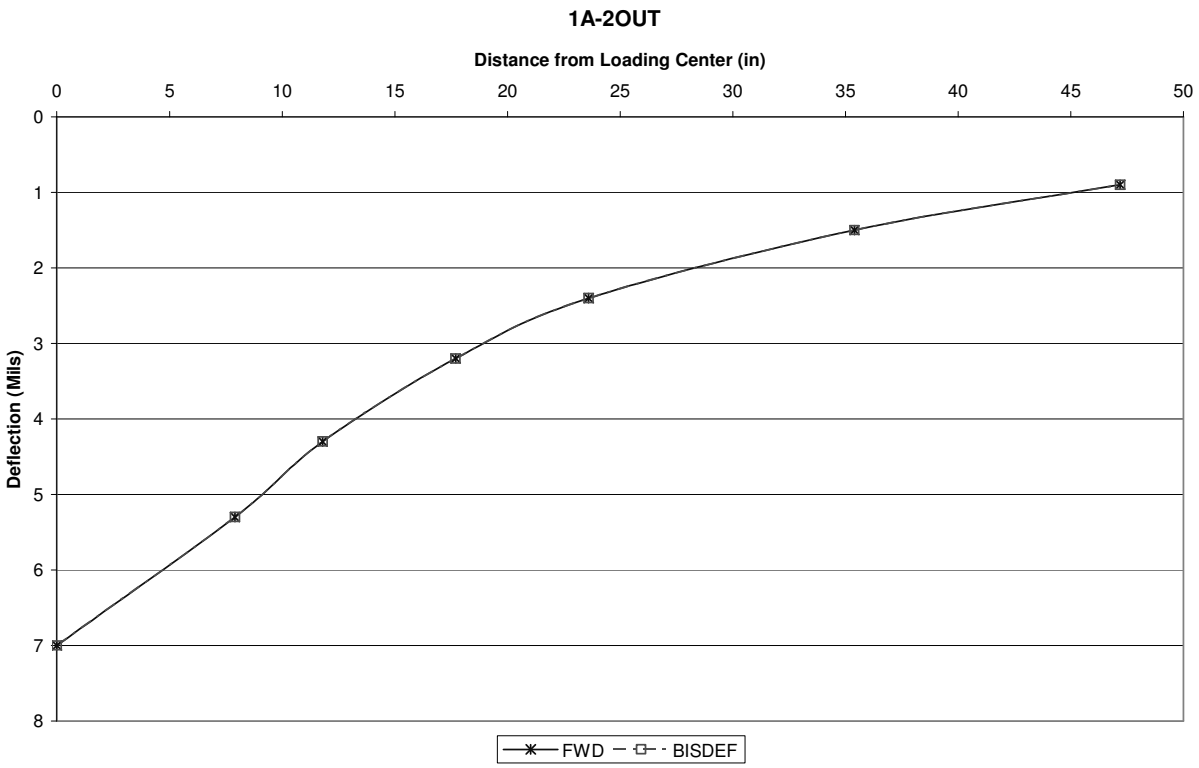


Figure 5.1 Typical Matching of Deflection Basins between FWD and BISDEF

The backcalculation was performed in two ways: 1) by considering base and subbase layers independently (four-layer structure); and 2) by treating base and subbase as a single layer (three-layer structure). The three-layer structure was modeled first to establish reasonable bounds for the layer moduli, then the four-layer analysis was performed to fine-tune the analysis.

Table 5.1 shows an overview of the measurements performed during FWD and impact echo tests. FWD measurement locations are presented in the Figures 5.2 to 5.4.

Table 5.1 Overview of HVS measurements and accompanying non-destructive tests

| | HVS measurements 2006 | | | | | FWD measurements 2006 | IE measurements 2006 | |
|---|---|---|---|---|---|---|---|---|
| Section | Phase | Performed | | Strain measurements<br>T = transversal<br>L = longitudinal | # load repetitions | Measured | June 09 | 1A, 1B, 1C: 1 point in wheel path, 1 point out of wheel path |
| 1C | 1 | March 13 | AM | 13 × 50 mm T (left) | 766 | March 10 (6 points) | | |
| | 2 | May 23–May 27 | Night-time | 3 × 50 mm T (right)<br>4 × 20 mm L (right)<br>2 × 20 mm T (left)<br>2 × 50 mm T (left)<br>5 × 30 mm T (left) | 29960 | May 16 (6 points)<br>June 02 (3 lines; 4 points in centerline, 3 points in each of other lines, 2 single points) | | |
| | 3 | July 28–Aug. 14 | All day | 8 × 50 mm T (right)<br>5 × 120 mm T (left) | 205570 + conditioning | August 21 (4 lines, 4 points in each) | July 26 | 5×5 points |
| 1B | 1 | Aug. 23–Sept 30 | All day | No | 242134 w.<br>125453 no w. | August 18 (4 lines, 4 points in each) | Sept. 20 | 2×5 points |
| 1A | | | | | | June 06 (4 points for each of two loads) | | |

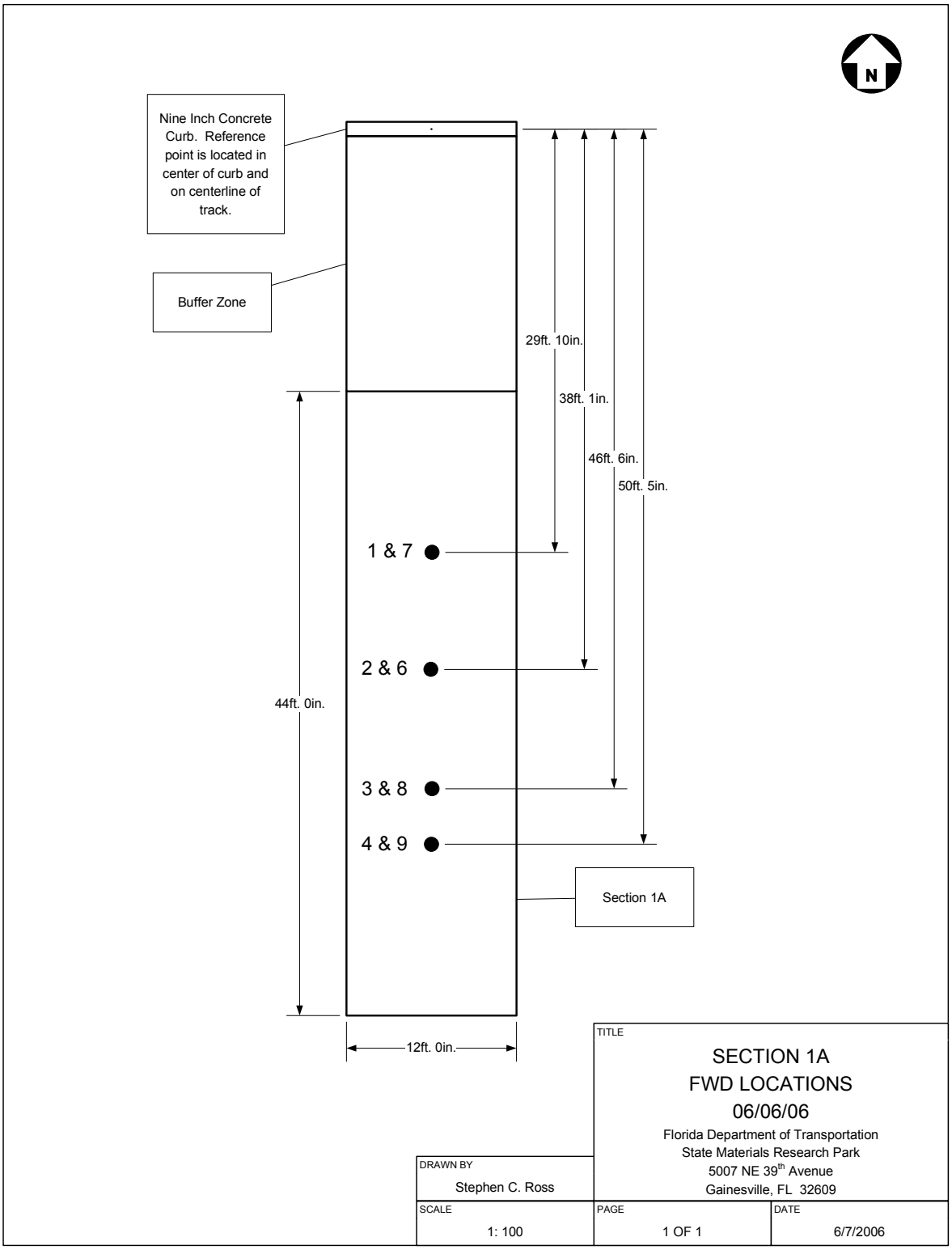


Figure 5.2 Section 1A FWD measurement locations

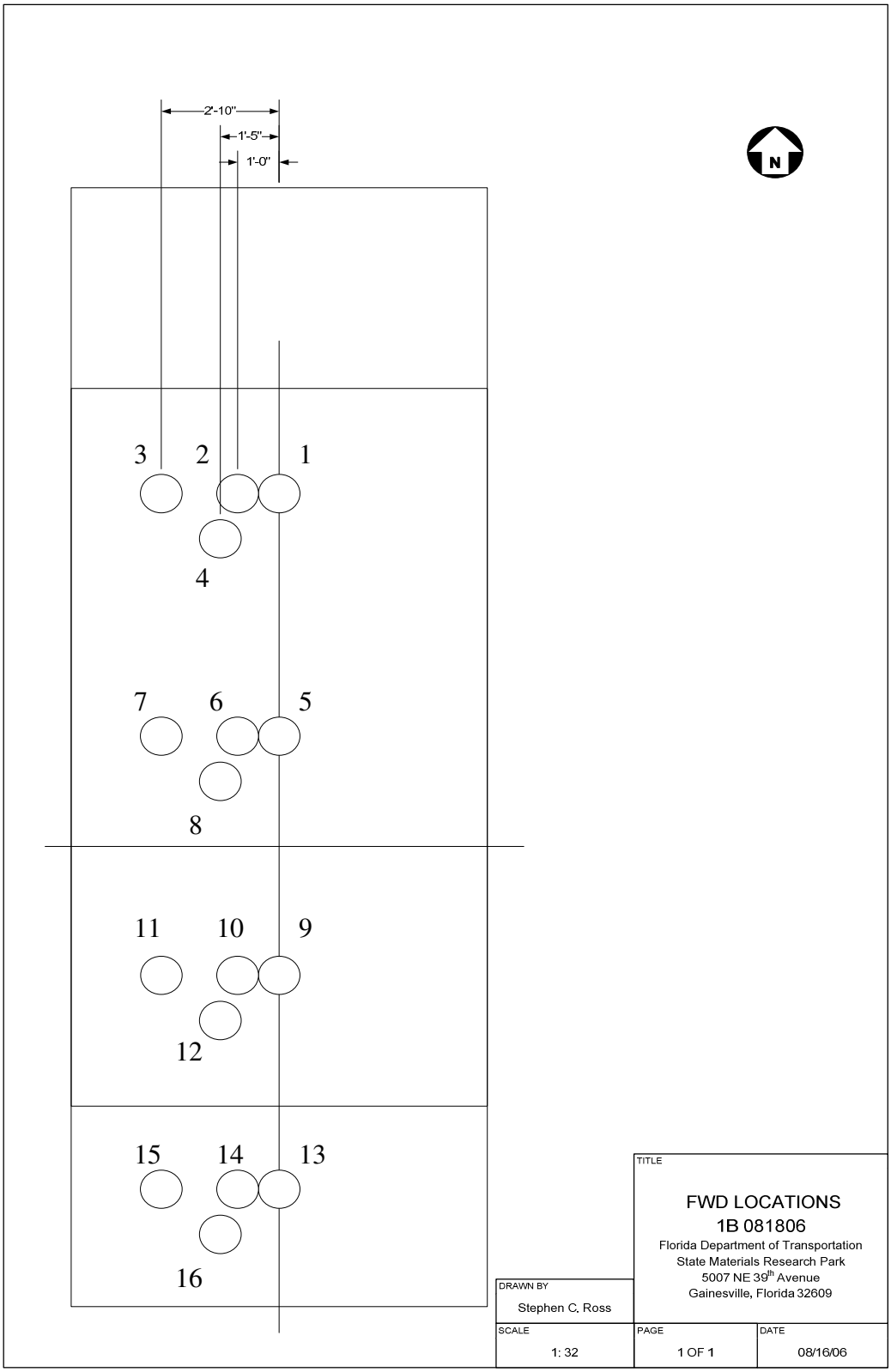


Figure 5.3 Section 1B FWD Measurement Locations

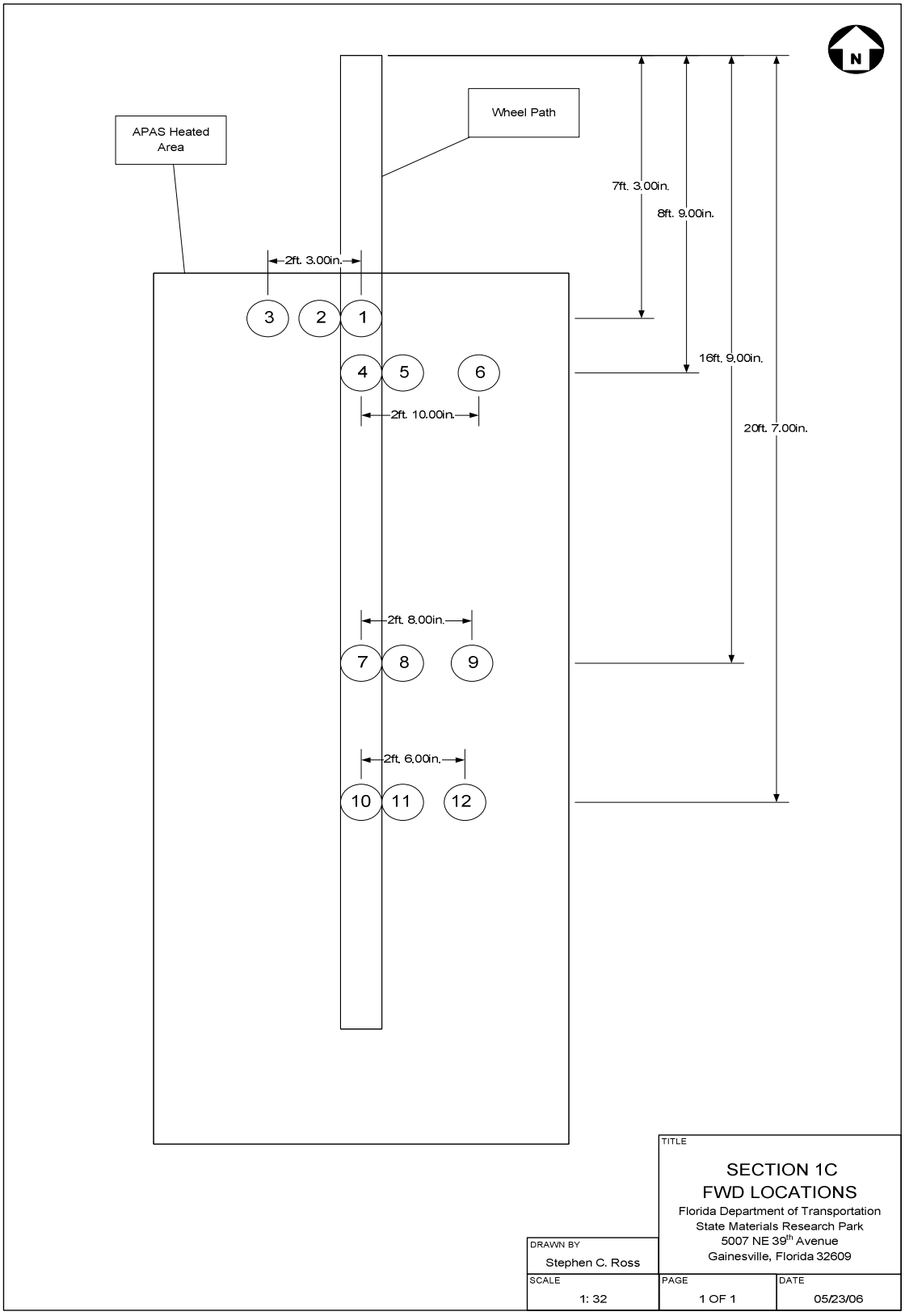


Figure 5.4 Section 1C FWD measurement locations

Tables 5.2 and 5.3 show the backcalculated moduli for the four-layer and the three-layer cases, respectively. Figure 5.5 shows the average base layer moduli for the different sections, while Figure 5.6 presents the average backcalculated AC modulus and range, where relevant, for the four-layer pavement. The HMA modulus variation was expected because of differences in temperature during testing.

Table 5.2 Backcalculated moduli [psi] from FWD measurements (four layer structure)

| | Thickness | Section 1A | Section 1B | | Section 1C | | | | |
|---|---|---|---|---|---|---|---|---|---|
| | | June '06 | Aug '06 | Aug '06 | Mar '06 | May '06 | June '06 | | Aug '06 |
| Dist. from center | | 0 | 0 | 2'-10" | 0 | 0 | 0 | 0 | 1' |
| Pvmt. tmp. [F] | | 73 | 77 | 78 | 59 | 67 | 72 | 72 | 76 |
| AC | 6" | 580 500 | 500 000 | 490 000 | 715 000 | 475 000 | 645 000 | 530 000 | 450 000 |
| Base | 10.5" | 81 000 | 67 000 | 39 000 | 29 000 | 38 500 | 30 000 | 30 000 | 36 000 |
| Subbase | 12" | 24 000 | 32 000 | 39 000 | 22 000 | 16 500 | 21 000 | 21 000 | 33 000 |
| Subgrade | 210" | 44 500 | 38 000 | 38 000 | 43 500 | 53 000 | 46 000 | 46 000 | 53 000 |
| Av. % diff. | | 1.5 | 3.1 | 3.1 | 2.8 | 3.2 | 4.5 | 4.3 | 2.0 |

Table 5.3 Backcalculated moduli [psi] from FWD measurements (three layer structure)

| | Thickness | Section 1A | Section 1B | | Section 1C | | | | |
|---|---|---|---|---|---|---|---|---|---|
| | | June '06 | Aug '06 | Aug '06 | Mar '06 | May '06 | June '06 | | Aug '06 |
| Dist. from center | | 0 | 0 | 2' 10" | 0 | 0 | 0 | 0 | 1' |
| Pvmt. tmp. [F] | | 73 | 77 | 78 | 59 | 67 | 72 | 72 | 76 |
| AC | 6" | 650 000 | 565 000 | 490 000 | 715 000 | 475 000 | 565 000 | 530 000 | 440 000 |
| Base/ subbase | 22.5" | 49 000 | 47 000 | 39 000 | 25 700 | 28 000 | 28 000 | 26 000 | 35 000 |
| Subgrade | 210" | 41 000 | 38 000 | 38 000 | 43 000 | 48 000 | 44 000 | 46 000 | 53 000 |
| Av. % diff. | | 3.1 | 4.1 | 3.1 | 3.2 | 3.3 | 4.8 | 4.4 | 1.9 |

As can be seen, only minor improvements were achieved by going from a three to a four layer pavement, and in some cases the goodness of fit drops by such a change. The subgrade and AC moduli hardly change at all by this shift, and when they do, the change is within ±10 % for the subgrade and within ±15 % for the AC layer. With a few exceptions, the individual base and subbase moduli vary by less than ±20 % from the combined modulus. The base modulus is clearly decreasing from the normal level in the

northern part of the test track southwards. Section 1C had a rather low base layer stiffness, which appeared to be caused by groundwater level effects.

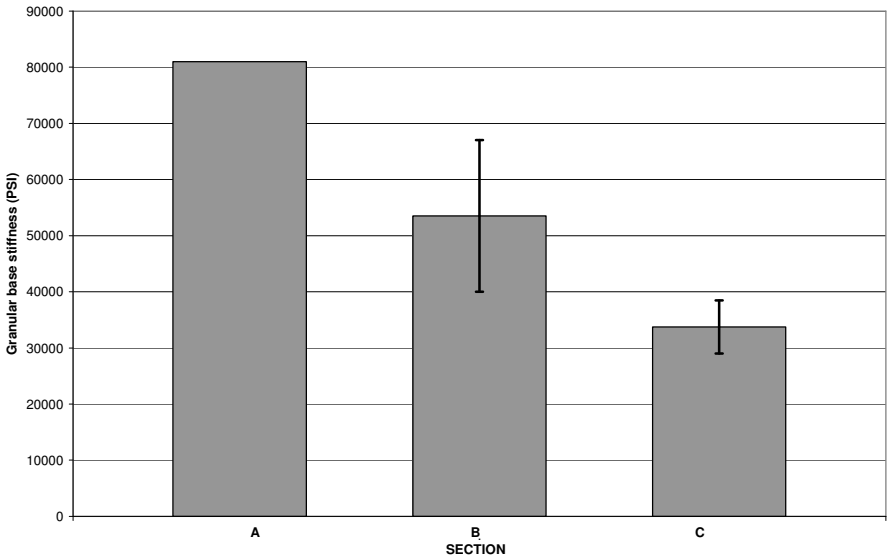


Figure 5.5 Average backcalculated base layer modulus (psi) for the sections

As expected, the highest AC modulus was backcalculated from the March measurements, when the temperature was lowest. For the rest of the measurements there was relatively little temperature variation. Two of the three AC moduli lower than 500000 psi were from FWD tests performed outside the wheel path. Therefore, these results seemed to indicate that no permanent damage was caused by loading. However, it should be noted that FWD measurements are greatly affected by subgrade and base condition, whereas micro-damage is rather local. Therefore, FWD measurements would probably not be affected by surface damage until the damage develops into a major deficiency of the asphalt layer.

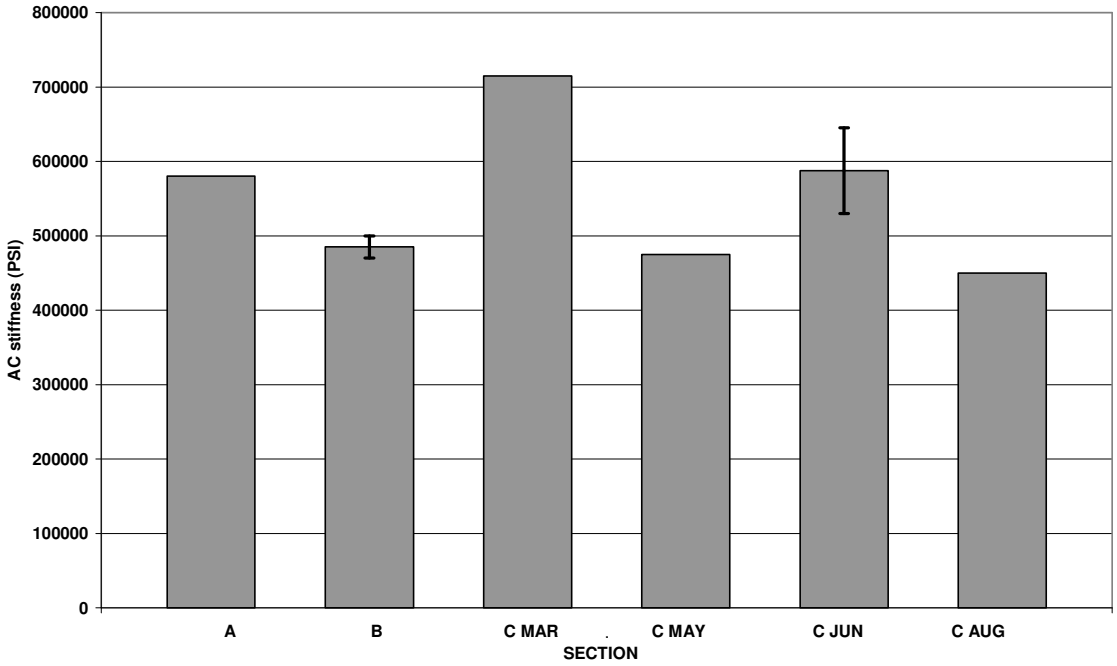


Figure 5.6 Backcalculated AC layer modulus [psi] for different FWD measurements

## 5.2 Impact Echo

Analyses presented in this report have shown that it would be difficult to capture crack initiation and development with strain gauges alone. Furthermore, for more production-like experiments strain gages are an impractical way to measure distress. The purpose of performing impact-echo testing for this research was to evaluate the possibility of using a completely nondestructive testing method to obtain quantitative results for determining cracking and deterioration in asphalt pavement. Such results have been successfully acquired in Portland cement concrete structures and pavements, therefore the application of impact-echo to asphalt concrete was considered viable.

A limited test was conducted early in the morning of June 9 2006, approximately one hour before sunrise; the test was conducted before sunrise to avoid the effects of differential heating of the pavement by solar radiation. The impact echo device was used in and outside the wheel paths at Section 1C, the aged but so far untrafficked Section 1B

and the unaged Section 1A. In addition, measurements were performed across a filled core hole and across a cable groove.

As shown in table 5.4, the results from these measurements were promising, as considerable differences could be seen among some of the different locations. The values in this table represent an average of five readings at each location. There was significant variability in the data; the results were not statistically significant at the 95% confidence level.

Table 5.4 Impact Echo statistics from initial measurements at Section 1C July 2006

| | In wheel path [m/s] | Velocity [m/s] | Outside wheel path [m/s] |
|---|---|---|---|
| Section 1A | 3209 | - | 3234 |
| Section 1B | 3250 | - | 3301 |
| Section 1C | 3030 | - | 3175 |
| Across core | - | 2583 | - |
| Across groove | - | 2835 | - |

As the initial Impact Echo measurements showed interesting results, more extensive measurements with a more statistically sound set-up were carried out at Section 1C in the morning of July 26 2006, the same day as the conditioning HVS loading for phase 3 started. The measurements were performed at five cross-sections, with measurement points in the wheel path and at several locations on both sides of the wheel path. At the 17” offset, where the highest tensile stresses were determined to occurred, measurements were carried out with the instrument both in the longitudinal and the transversal direction. Table 5.5 shows some statistics for the IE velocities measured at the different positions (based on five individual values):

Table 5.5 Impact Echo statistics from follow-up measurements at Section 1C July 2006

| | IE Velocity [m/s] | | Some probabilities [%] | | | |
|---|---|---|---|---|---|---|
| | Average | St. Dev. | WP ≠ x | 17" wL ≠ x | 17" wT ≠ x | WP > x |
| 41" west | 2656 | 114 | | | | |
| 29" west | 2634 | 156 | 99.8 | 93.8 | | 99.9 |
| 17" west Transv. | 2912 | 189 | | 67.8 | - | |
| 17" west Longit. | 2813 | 73 | 99.9 | - | | 99.97 |
| Center of wheel path | 3050 | 66 | - | | | - |
| 17" east Longit. | 2798 | 283 | 88.1 | 8.5 | | 94.1 |
| 17" east Transv. | 2868 | 189 | | | 27.7 | |
| 29" east | 2848 | 106 | 99.1 | | | 99.5 |
| 41" east | 2681 | 214 | | | | |

WP:Wheel Path wL:West Longitudinal wT:West Transverse x:Location being compared

A possible explanation for the observed difference between the wheel path and the other positions covered, is that the wheel loading caused some densification of the asphalt material.

Table 5.6 shows some statistics for the IE velocities measured at Section 1B on September 20 (based on two individual values). The measurements were planned according to a similar pattern as for Section 1C, but due to equipment problems only two measurements were performed along each line. The measurements are therefore not as extensive as the ones carried out at 1C.

Table 5.6 Impact Echo statistics from measurements at Section 1B September 2006

| | IE Velocity [m/s] | | Some probabilities [%] | | | |
|---|---|---|---|---|---|---|
| | Average | St. Dev. | WP ≠ x | 17" wL ≠ x | 17" wT ≠ x | WP > x |
| 29" west | 2835 | 31 | 99.1 | 95.5 | | 99.6 |
| 17" west Transv. | 3151 | 11 | | 91.6 | - | |
| 17" west Longit. | 3114 | 5 | 90.4 | - | | 95.2 |
| Center of wheel path | 3303 | 42 | - | | | - |
| 17" east Longit. | 3192 | 201 | 42.4 | 32.2 | | 71.2 |
| 17" east Transv. | 3164 | -* | | | N/A | |
| 29" east | 3052 | 74 | 92.4 | | | 96.2 |

1. * Just one measurement
2. WP:Wheel Path wL:West Longitudinal wT:West Transverse x:Location being compared

In any case, the same tendencies can be seen for 1B as for 1C. The wheel path has a significantly higher velocity than the other lines (not significant for the 17" east line due to the higher standard deviation for the latter). For the same reason, the 17" east line is not significantly different from the 29" east line. Except for that, there is a significant trend towards decreasing stiffness from the center line outwards.

During the course of the testing regimen it was discovered that larger spherical impactors than the ones typically used for Portland Cement Concrete were required for asphalt concrete. This is due to the fact that the stress waves required much more energy to create a signal large enough to be obtained by the piezoelectric transducers on the impact-echo device. Also, it was observed that the collision between the spherical impactor and the asphalt concrete did not produce a rebound similar to those observed by PCC with the same impactors.

Other differences between PCC and asphalt concrete that may affect the results include the fact that PCC does not experience localized density changes due to loading conditions within its elastic range. Also, the hardened product of Portland cement paste is typically more brittle and dense than that of asphalt concrete and healing of cracks upon temperature changes observed in asphalt concrete, does not occur in Portland cement concrete materials. Thus, the nature of damage and cracking in Portland cement concrete tends to be a permanent, cumulative, effect which allows for the long term monitoring of damage due to cracking using Impact Echo. The behavior of asphalt concrete makes Impact Echo less suitable for this purpose.

Due to the inherent property differences between PCC and Asphalt Concrete it may be beneficial to do some comparative laboratory studies on both materials in an effort to

determine the applicability of impact-echo to asphalt concrete. Therefore, more research is needed to determine the viability of using impact-echo for the monitoring of asphalt concrete pavement.

### 5.3 Spectral Analysis Of Surface Waves SASW

SASW （Joh,1996）is a seismic method developed for determining shear wave velocity and shear modulus profiles of geotechnical sites; this is not a routine technique for detecting cracks or damage in asphalt concrete (AC). However, some SASW tests were conducted prior to the HVS loading to measure the pavement's characteristics in the uncracked state. These SASW tests indicated that existing measurement techniques and interpretation methods were not optimized for purposes of detecting the near-surface changes resulting either from age-hardening or damage. Also, the system was rather cumbersome in its current state and required high level technical expertise to perform and interpret the tests at this time. Figure 5.7 shows the typical setup for SASW test.

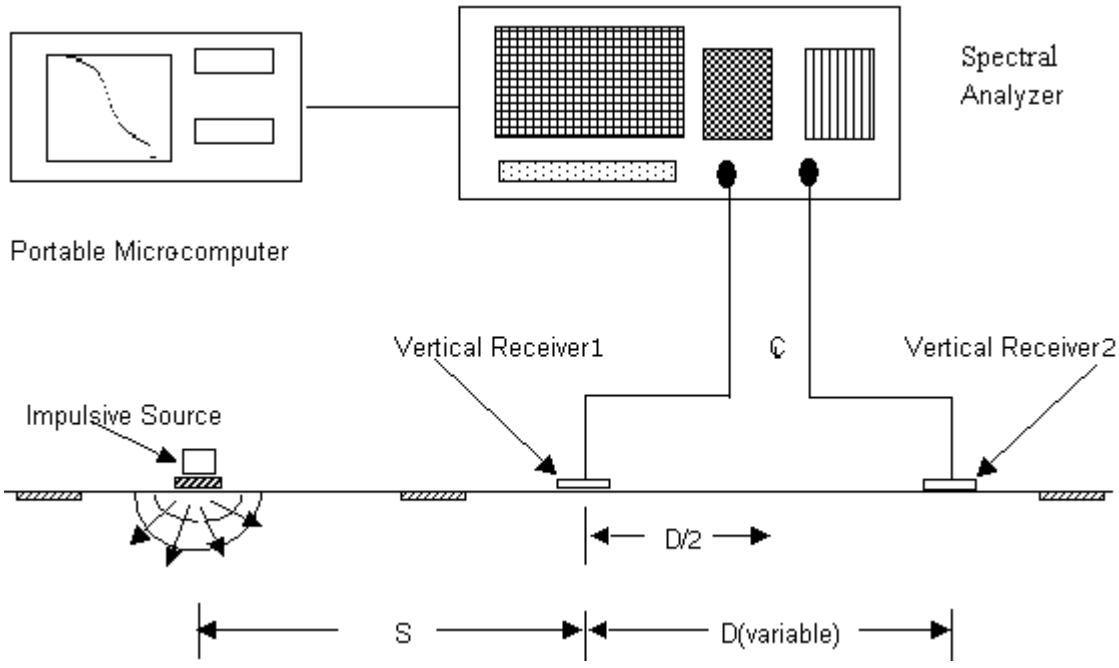


Figure 5.7. Layout of the testing setup of the SASW method

### 5.4 Electrical Resistivity Test.

An idea emerged to use electrical potential to reveal micro-cracking; contact was established with Chemical Engineering at UF to test this idea. Some ordinary asphalt specimens were prepared and sent to Chemical Engineering for initial testing.

Electrical resistivity tests performed on cores in the laboratory indicated that this approach does have potential for crack and damage detection. However, the system would have to be developed and evaluated for use on full-scale pavements.

# CHAPTER 6
# ANALYSIS OF RESPONSE AND CRACKING

This chapter includes the theoretical analyses performed for modeling of HVS loading, including potential effects of consolidation rutting on stress distribution near the tire, and DCSE calculations for prediction of crack initiation.

## 6.1. HVS loading and strain data analysis

An overview of the HVS loading performed on the different test sections is presented in the table 6.1.

Table 6.1 Overview of HVS measurements

| | HVS measurements in 2006 | | | | |
|---|---|---|---|---|---|
| Section | Phase | Performed | | Strain measurements<br>T = transversal<br>L = longitudinal | # load repetitions |
| 1C | 1 | March 13, 2006 | AM | 13 × 50 mm T (left) | 766 |
| | 2 | May 23–May 27 2006 | Night-time | 3 × 50 mm T (right)<br>4 × 20 mm L (right)<br>2 × 20 mm T (left)<br>2 × 50 mm T (left)<br>5 × 30 mm T (left) | 29960 |
| | 3 | July 28–Aug. 14 2006 | All day | 8 × 50 mm T (right)<br>5 × 120 mm T (left) | 205570 + conditioning |
| 1B | 1 | Aug. 23–Sept 30 2006 | All day | No | 242134 w.<br>125453 now. |
| | | Oct.10–Oct.19 2006 | All day | 6× 50mm T<br>2×50mm T (Embedded) | 271849+ Conditioning (till Oct.19) |
| | 2 | Dec.5-Dec.16 2006 | All Day | 4× 50 mm T (left)<br>4 × 50 mm T (Right) | 732106+Conditioning (till Dec.16) |
| | | HVS measurements in 2007 | | | |
| | | Jan.30-Feb.2 2007 | All Day | 4× 50 mm T (left)<br>4 × 50 mm T (Right) | 1,189,455+Conditioning (till Feb.2) |
| 1A | 1 | Feb.6-Mar.27 2007 | All Day | 4 × 50 mm T (Southern)<br>4 × 50 mm T (Northern) | 488,358 Aging (Northern)<br>Non-Aged (Southern) |

### 6.1.1 Section 1C

Three HVS load phases were involved in this section. Results of each phase are presented in the following subsections.

#### 6.1.1.1 Phase I

In order to test whether the strain measurement system worked properly or not, HVS Phase I loading was applied to Section 1C on March 13, 2006. The pavement was loaded at three levels; 6 kip, 8 kip and 10 kip. Around 250 load cycles were applied at each level. Dynamic strain data were collected for 10 second increments each minute. As shown in Figure 6.1, 13 strain gages, 50 mm long each, were installed transverse to the wheel path, spanning a total distance of 0.5 to 30 inches from the wheel path edge. The asphalt surface was polished along a 2.5 foot long track outside and perpendicular to the HVS wheel track by using a belt sander. Additional smoothness was secured by adding a thin layer of epoxy along the track and resanding with finer sand paper.

Figures 6.2 to 6.4 present typical plots of strain measurements; these curves clearly depict expected strain reversals and viscoelastic effects during loading. Generally, as the wheel approached the gage location, compressive strain was measured by the gage, then when the wheel was directly above the gage, the strain reversed to a low value of compressive strain or higher value of tensile strain, depending on the location of the gage. When the wheel moved away from the gage, the strain again reversed.

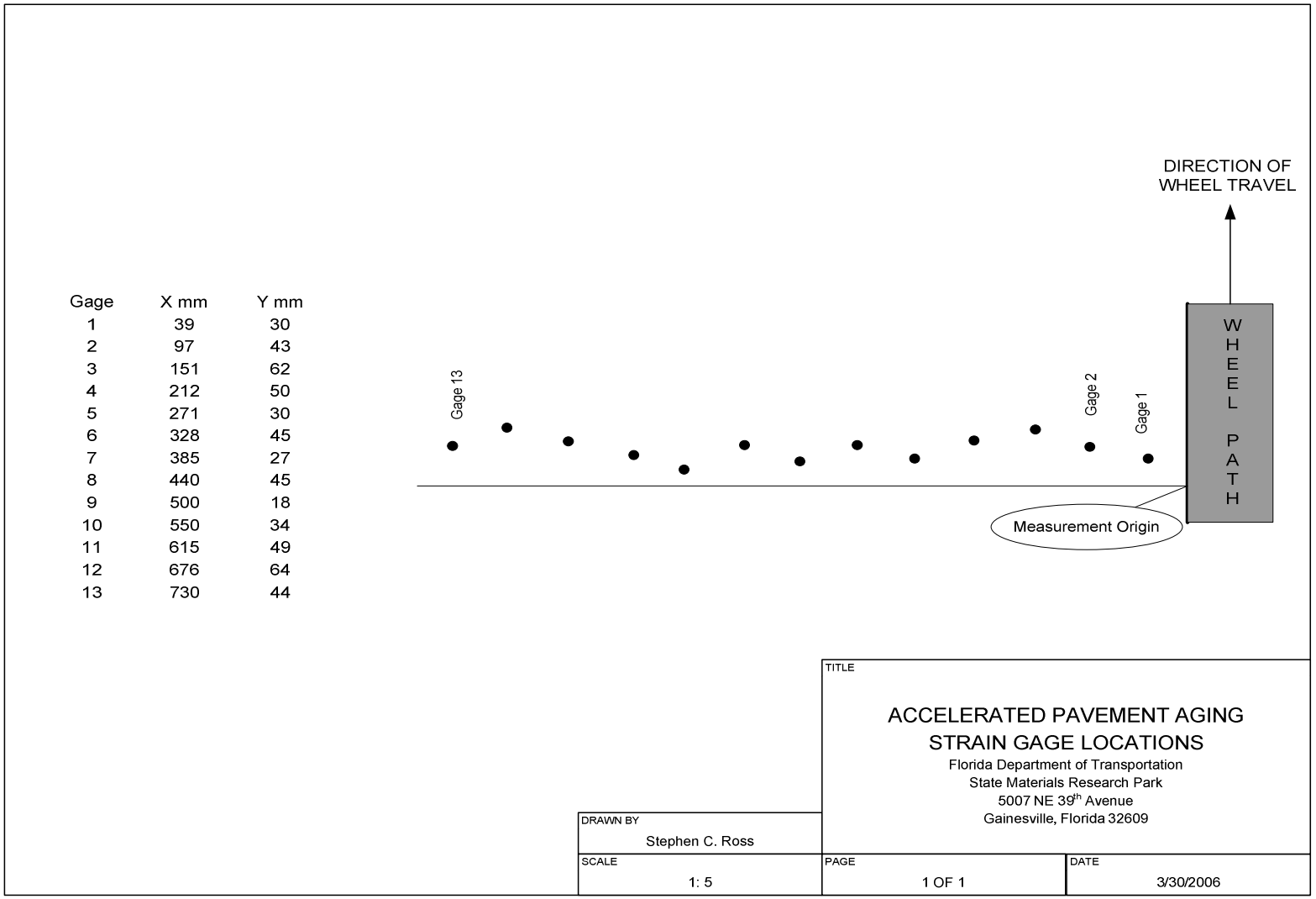


| Gage | X mm | Y mm |
|---|---|---|
| 1 | 39 | 30 |
| 2 | 97 | 43 |
| 3 | 151 | 62 |
| 4 | 212 | 50 |
| 5 | 271 | 30 |
| 6 | 328 | 45 |
| 7 | 385 | 27 |
| 8 | 440 | 45 |
| 9 | 500 | 18 |
| 10 | 550 | 34 |
| 11 | 615 | 49 |
| 12 | 676 | 64 |
| 13 | 730 | 44 |

Figure 6.1 Strain Gages for Section 1C Phase I Layout

In Figures 6.2 to 6.4, the first downward peak (into compression) is called the first peak, while the following upward peak (either tension or a small compression strain) is called the second peak. The constant horizontal strain level recorded before the wheel pass is called the baseline strain. The difference between the peak and baseline is called strain (either tensile strain or compressive strain). Since the 2nd peak is the one that most likely gives the tensile response of the gage, most of the effort in this report was focused on the strain difference between the 2nd peak and the baseline.

Figure 6.5 shows the 2nd peak strain as a function of load cycles for different load levels. Except for gages 1 and 2, all the gages exhibited tensile responses. Both tensile and compressive strain increased with load level. However, no significant variation was observed in the strain as function of number of passes for 6 kip, 8 kip or 10 kip loading. This indicates that there was little or no damage induced near the locations of the strain gages.

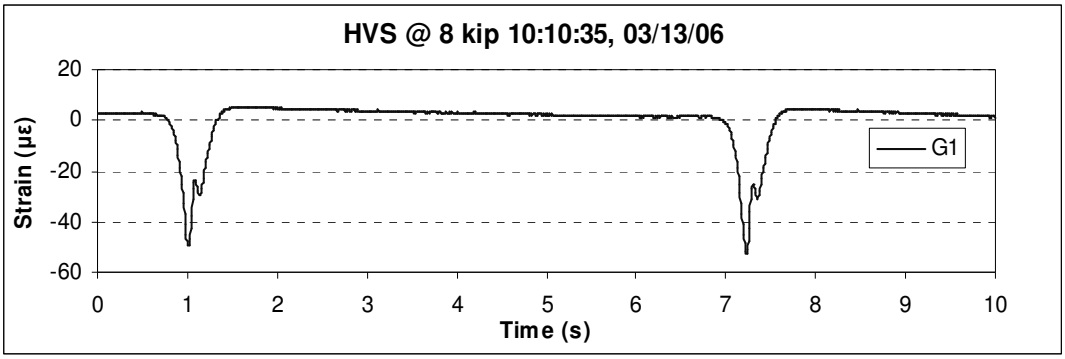


Figure 6.2 Typical Strains Reading for Gage 1

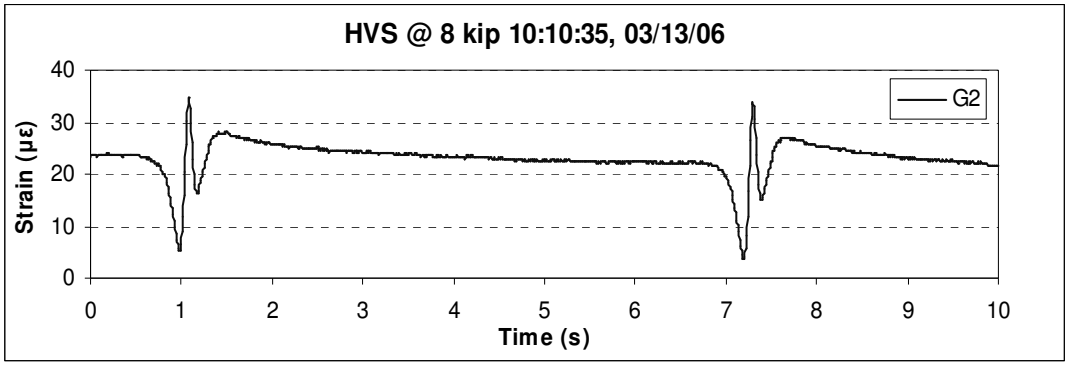


Figure 6.3 Typical Strains Reading for Gage 2

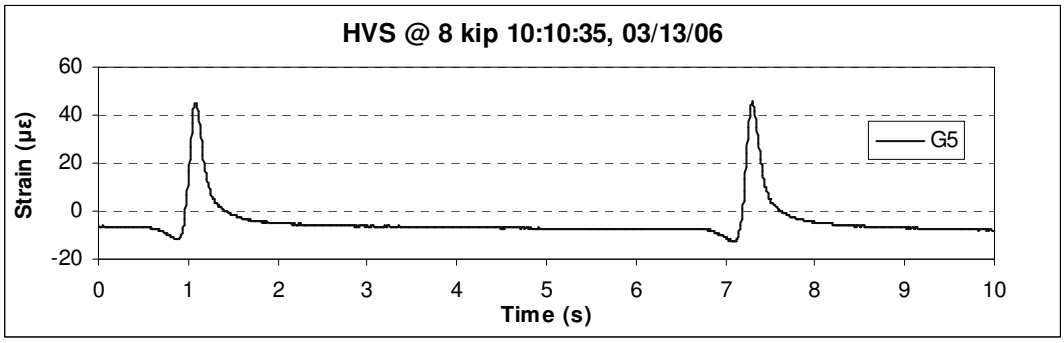


Figure 6.4 Typical Strains Reading for Gage 5

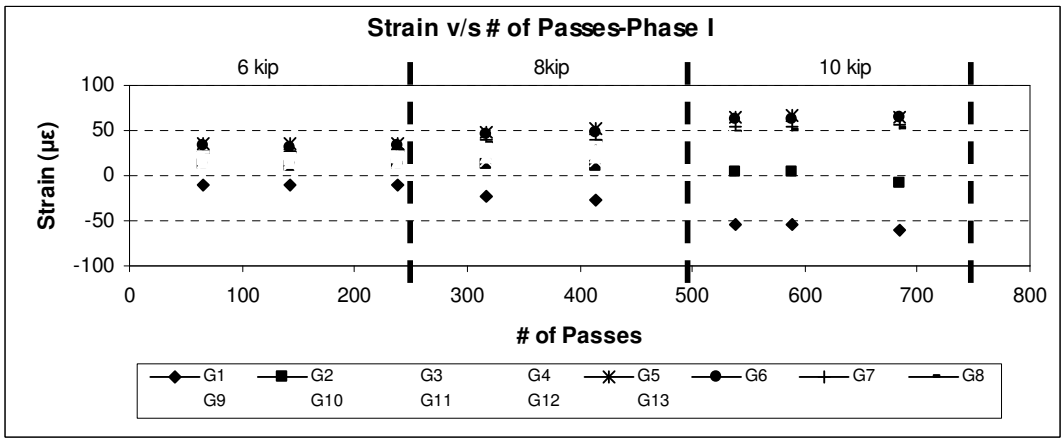


Figure 6.5 Variation of 2nd Peak Responses for Gages during HVS Test in Section 1C-I

### 6.1.1.2 Phase II

Figure 6.6 shows the strain gage layout for Phase II. After Phase I, all strain gages (50 mm long each) were removed and new gages were installed for Phase II. According to the experiences from Phase I, some of the previous positions were left out, but for the remaining locations the new gages were mounted as close to the previous positions as

possible. In addition, a 20 mm gage was mounted parallel to the 50 mm gage placed near the Phase I gage 2 position (the 20mm gage was actually 15mm/0.6 in further away from the wheel path). Altogether nine transverse strain gages were installed at the previously prepared surface track.

To compare strains on the different sides of the wheel path, three 50 mm transverse strain gages were mounted on the opposite side of the wheel track. These coincided closely to the gage 1, gage 2 and gage 5 positions on the other side. Four 20 mm strain gages were also installed to measure longitudinal strains. Three were placed on the same side and transverse location as the three 50 mm duplicate gages described above. The fourth longitudinal gage was mounted just 25 mm from the edge of the wheel path.

The second phase of HVS load cycles started on May 22 and ended on May 27, 2006. The measurements were carried out at night, from around 8:30 pm to 07:00 am to take advantage of cooler temperatures and early evening temperature gradients. The HVS load was 8 kip the first two nights, but as no damage effects were observed during those nights, the load was increased to 12 kip. Due to some problems with the HVS application counter, the exact number of applications is not known, but around 6,000 load repetitions were applied each night. In total, around 29,950 load cycles were applied during phase II. The strain measuring, reporting procedure and temperature recordings used for this phase were the same as for the Phase I HVS test.

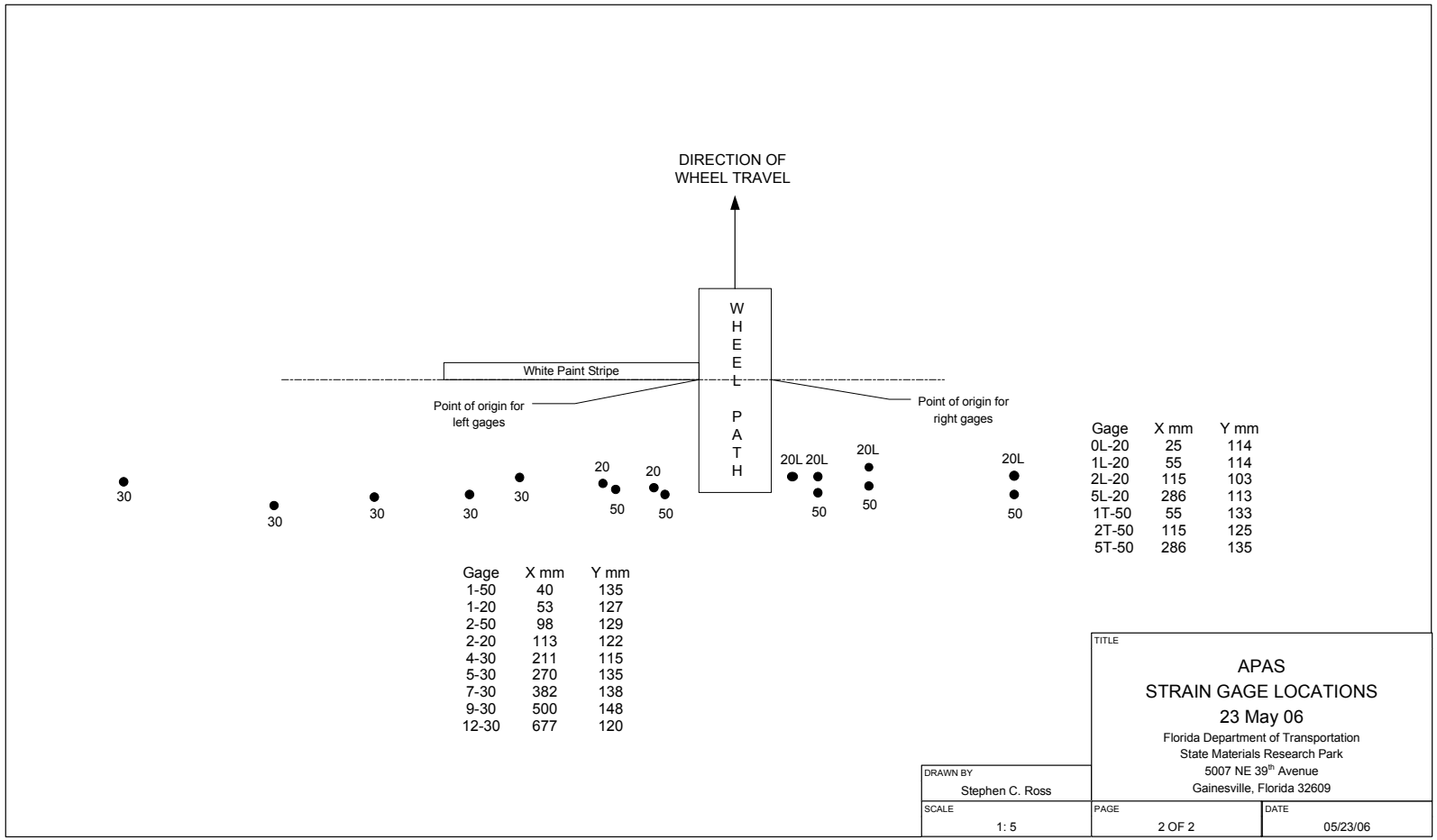


Figure 6.6 Strain Gages for Phase II in Section 1C Layout

Unfortunately, no cracks were discovered. Figure 6.7 shows typical gage readings for the 2nd peak in this phase, which clearly indicate that the 2nd peak values vary slightly within a day. This might be caused by changes in temperatures, and increased slightly from day to day. This appeared to provide some indication that the pavement was being damaged with the increased number of load repetitions, which decreased the modulus of the material and increased strain readings.

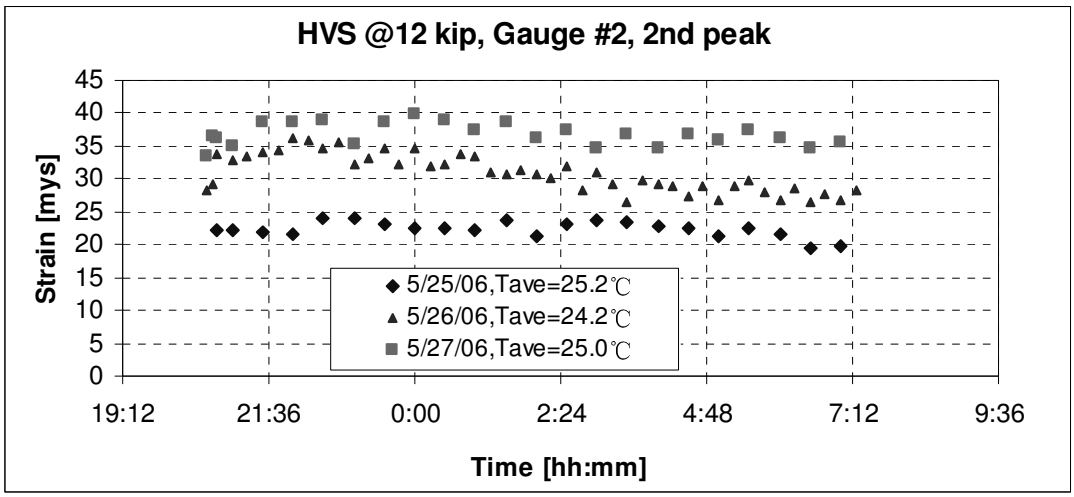


**Tave: Average temperature at AC surface**

Figure 6.7 Typical gage readings for 2nd peak values in Section 1C-II

Figures 6.8 and 6.9 show the peak load-induced strains measured for all gages in this phase as a function of load repetitions. It can be seen that the peak strain values increase suddenly at about 12,000 load cycles due to change of loading level from 8 kips to 12 kips. However, there was little change in strain readings at each loading level, which might indicate that there was no damage occurred at this stage.

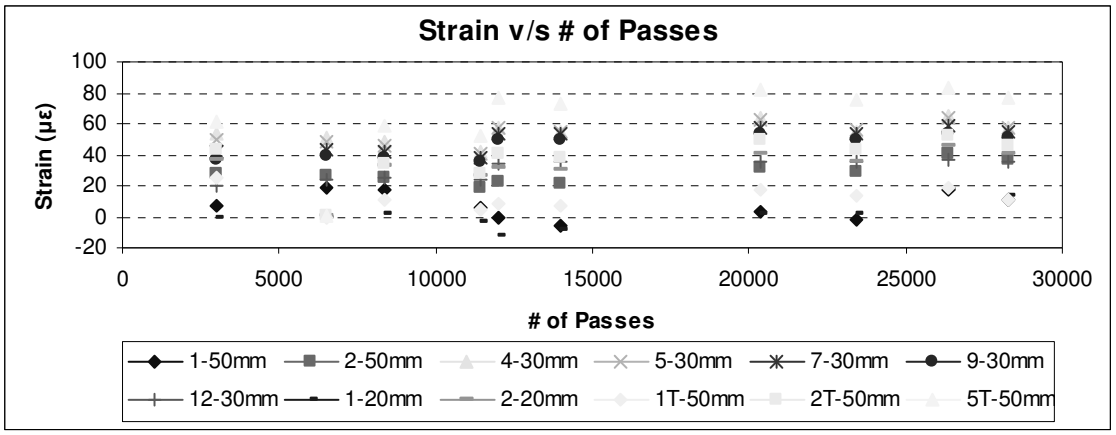


Figure 6.8 Variation of 2nd Peak Strains for Transverse Gages during HVS Test in Section 1C-II

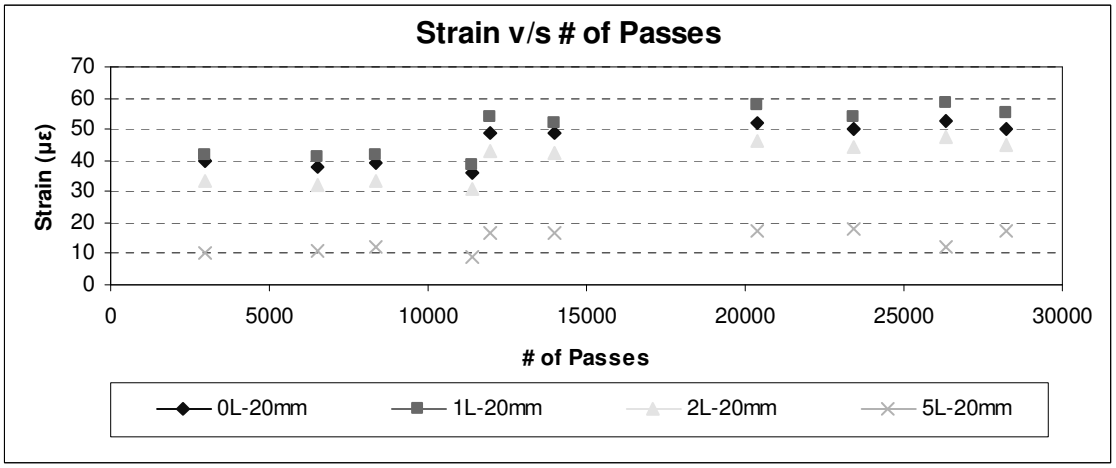


Figure 6.9 Variation of 2nd Peak Strains for Longitudinal Gages during HVS Test in Section 1C-II

### 6.1.1.3 Phase III

The third phase of HVS load cycles was applied to Section 1C between July 28 and August 14, 2006. Prior to that, around 24,000 applications of 9 kip conditioning load with 30" wander were applied during a 48 h period. The idea was to attempt to induce microdamage in the general area of the wheel path prior to concentrated loading. A 12 kip load with no wander was then applied 24 h a day, but there were short stops in the morning and afternoon to check for cracks. In total 205,570 cycles of the 12 kip load were applied during phase III.

Strain gages were installed after the conditioning load stage was finished. In Phase III, a new gage set-up was used, which originally was planned to be divided into a crack detecting stage and a crack development stage. As no crack was ever detected before, the measurements had to be abandoned due to excessive permanent deformations, therefore the last stage was never reached. The idea for the crack-detecting stage was to cover the most tensile-prone parts of the pavement surface on both sides of the wheel path with strain gages. On one side, 120 mm gages with around 1" individual overlap were mounted, while on the other side, 50 mm gages with practically no overlap were installed. The same strain measuring, reporting procedure and temperature recordings were used as in phase I and phase II. Figure 6.10 shows the actual strain gage set-up.

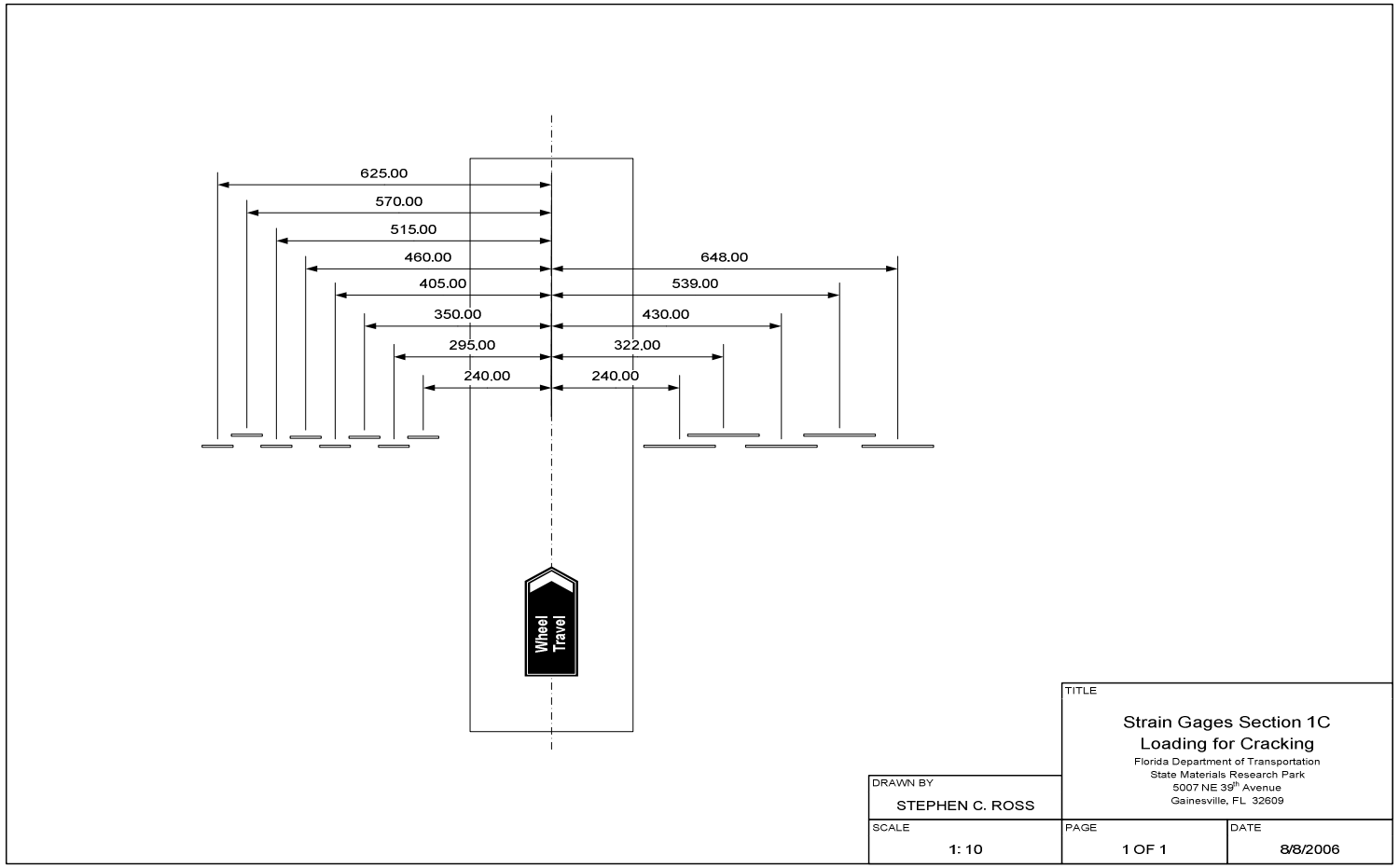


Figure 6.10 Strain Gages for Phase III in Section 1C Layout

Figures 6.11 and 6.12 show typical load pulses for Gage #1R50 and Gage #1L120 (the 50 mm and 120 mm gages closest to the wheel path on either side). As can be seen, the pulses do have a very similar shape. Comparable response patterns were observed for other gages, as well.

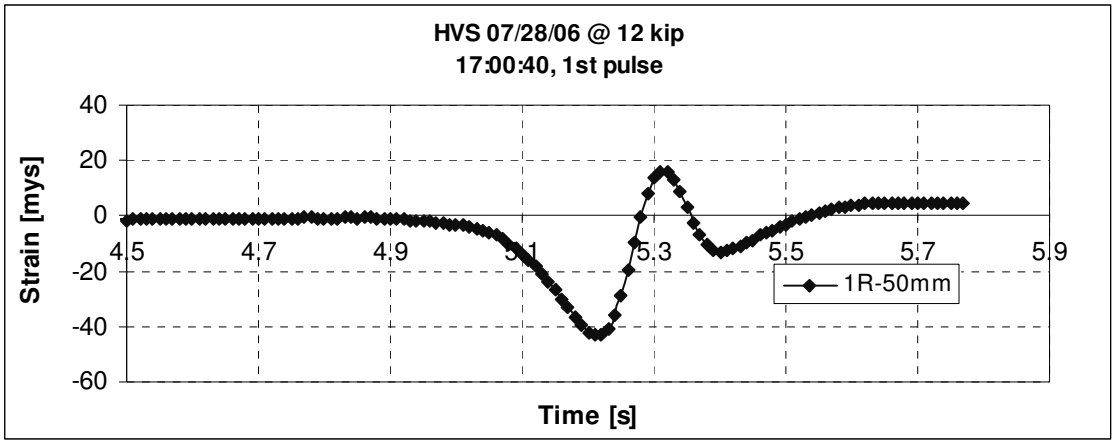


Figure 6.11 Typical strain readings for Gage #1R50 in section 1C-III

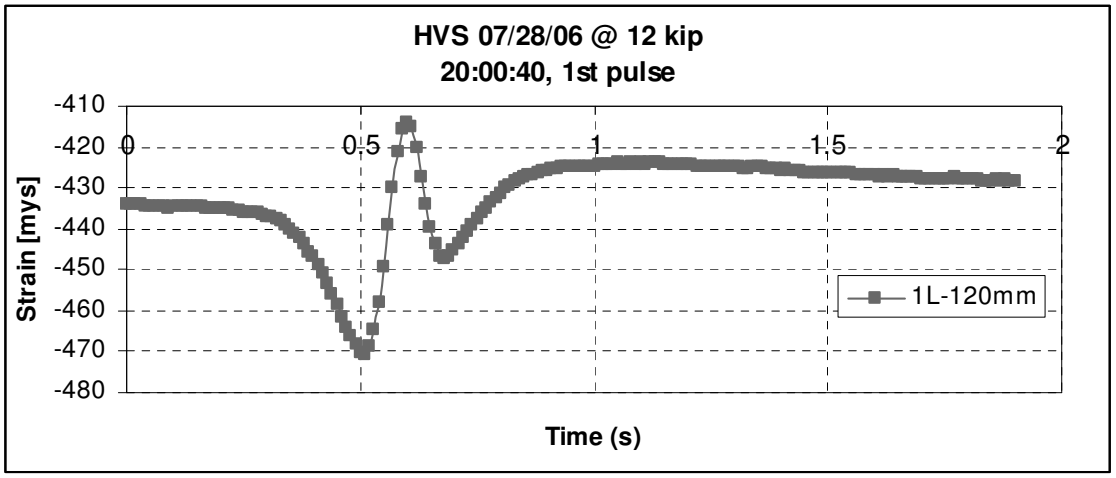


Figure 6.12 Typical strain readings for Gage #1L120 in section 1C-Phase III

An enormous amount of data was collected and analyzed, so just a selection is presented for each day. For all days, hourly measurements between 5:00 pm and 7:00 am are included, while measurements between 7am and 5pm are presented just for a selection of days and usually just for every second hour. However, in some cases, values

are presented at shorter time intervals to study their development and possibly explain suspicious peak values. Figure 6.13 shows the 2nd strain peak responses throughout Phase III.

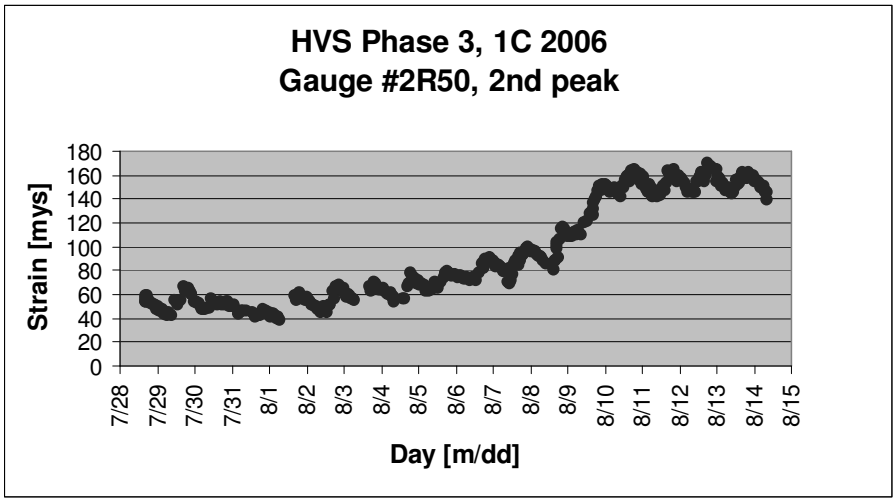


Figure 6.13 Typical 2nd peak responses in Section 1C-III

It was observed that daily variations are overshadowed by the general increasing trend with time. For most of the strain gages the daily variation was within 40 μs; also a rather dramatic strain increment was recorded when loading level was increased from 12 kips to 18 kips. Daily strain variation could be caused by daily temperature variation, while the increment of strain with time might be due to the increase of loading cycles and loading level.

### 6.1.2 Section 1B

Based on lessons learned during testing of section 1C, an instrumentation plan was developed for section 1B, which involved two phases.

#### 6.1.2.1 Phase I

HVS preload without strain measurement started on August 28 with a 12 kip load running with 34” wander (44-45” between outside edges of the tire at either side). After a hydraulic oil leak on the night of September 18, the HVS was stopped for repair for about

three working days starting on the morning of September 19, after which the loading continued for another day. Thereafter, the HVS wheel was moved slightly to the right of the center of the previous wander path, and run without wander for five days, until September 25. Taking into consideration the position of maximum tensile strain values at the surface and the strain profile during the full-wander phase, the center of the HVS wheel was moved 6” to the left of the center of the previous full-wander path on September 26. At the same time the inflation pressure was increased from 115 psi to 130 psi. The load proceeded at 12 kips load without wander until October, when the load had to be stopped again; this time due to extensive tire wear so that the HVS tire had to be replaced. Probably, the hydraulic oil from two weeks earlier played a role in this process, the tire got sticky and dissolved tire debris had to be removed from the pavement. How the oil affected the asphalt pavement is unclear, but even after attempts to clean up, the surface still seemed oily. For the period from August 23 to September 30, around 367,590 HVS load applications at 12 kips were applied, 242,134 of them were included in the 34” wander mode; 65,453 passes were applied during the first non-wander phase and around 60,000 in the second non-wander phase.

Strain gages were installed across crack-initiating grooves cut along the wheel path to measure surface strains; some strain gages were installed slightly below the asphalt surface to test whether or not they would survive directly under the wheel. In total, eight gages were installed, two in the wheel path and six outside. The strain gage layout is given in Figure 6.14. The strain measurements started on October 10 and ended on October 19 with around 639,439 cycles applied in total.

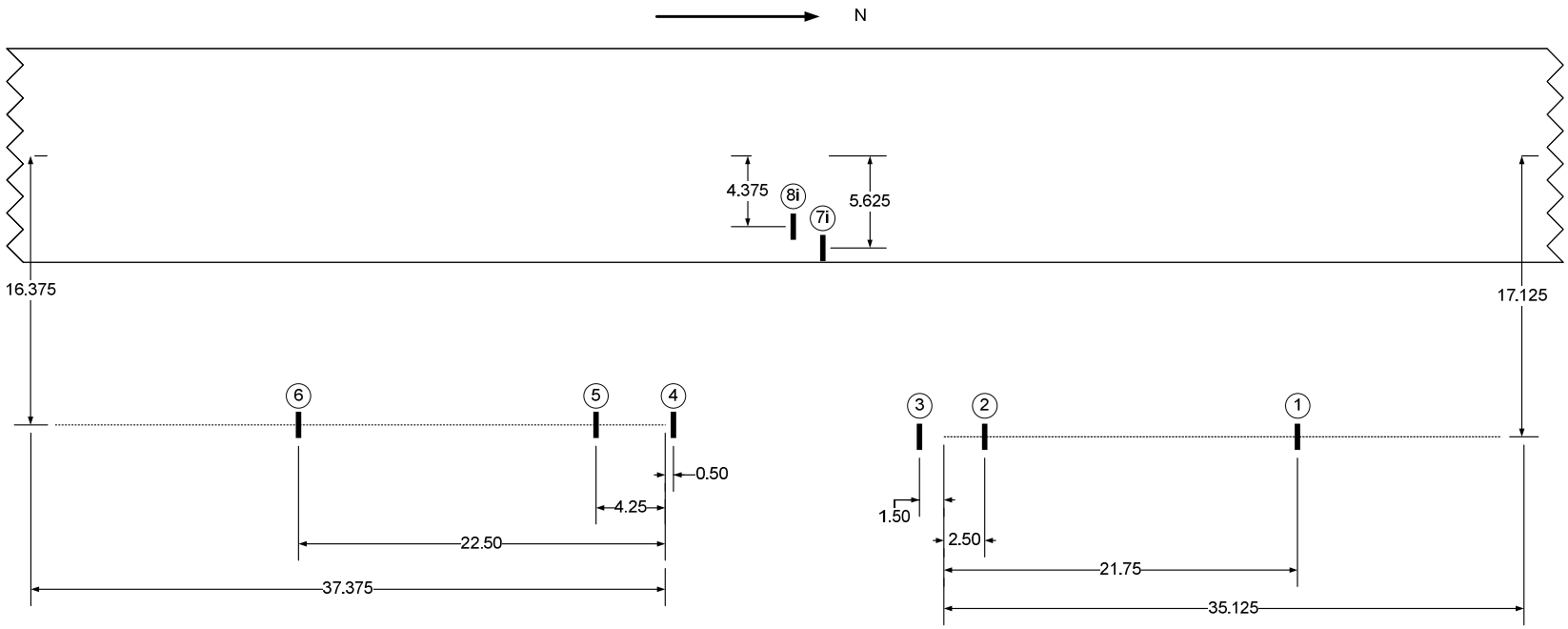


Figure 6.14 Strain Gages for Phase I in Section 1B Layout

Phase I typical strain readings are shown in Figure 6.15; it can be observed that pure compressive strain dominated in gage 8, which was surface mounted in the wheel path. The maximum compressive strain for this gage is about 300 με, which compares very favorably predicted values based on finite element analysis. This means that strain gages embedded in the wheel path can survive well and measure strains successfully when properly installed. However, it should be noted that the gages under wheel path would fail if they were not handled properly. For instance, the strain data from embedded gages were not reliable and had to be abandoned during the second phase of this section.

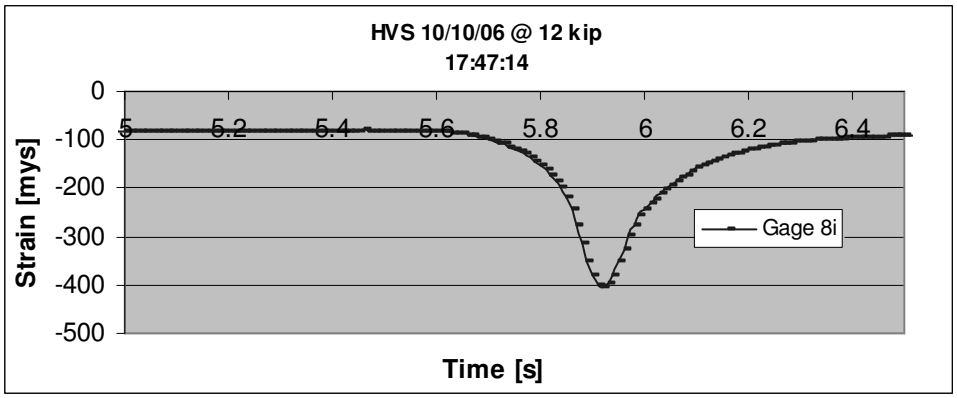


Figure 6.15 Typical strain readings for gages 8i in Section 1B-I

Figure 6.16 shows the 2nd strain peak responses throughout Phase I for gages outside the wheel path. This figure suggests that strains did not increase with time, which means there was little or no damage produced in this phase; also that strain varied daily around $20\,u\varepsilon$ magnitude, which indicates that ambient temperature probably influenced the strain readings.

To further illustrate how ambient temperature influenced the strain readings, typical plots with combinations of temperature and strains are given in Figures 6.17

and 6.18. These figures show excellent correspondence between temperature change and strain variation.

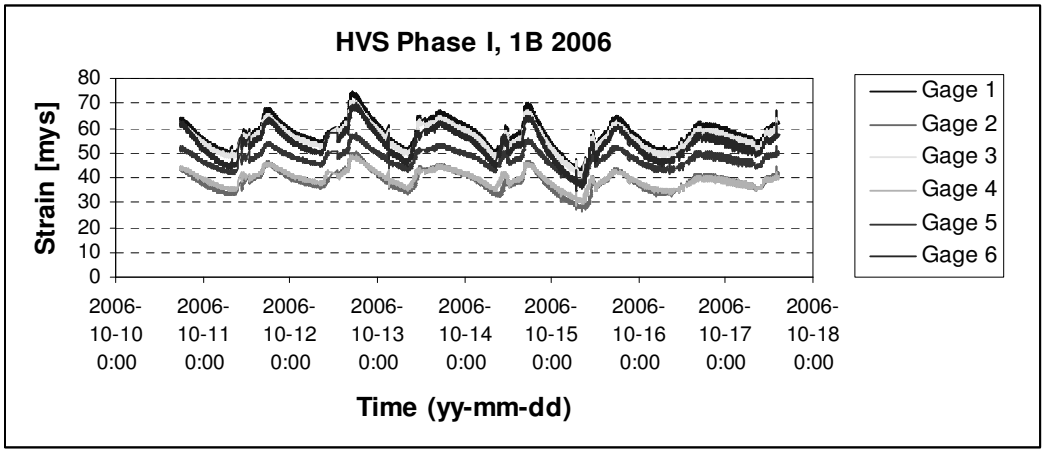


Figure 6.16 Variation of 2nd Peak Strains for Gages outside Wheel Path during HVS Test in Section 1B-I

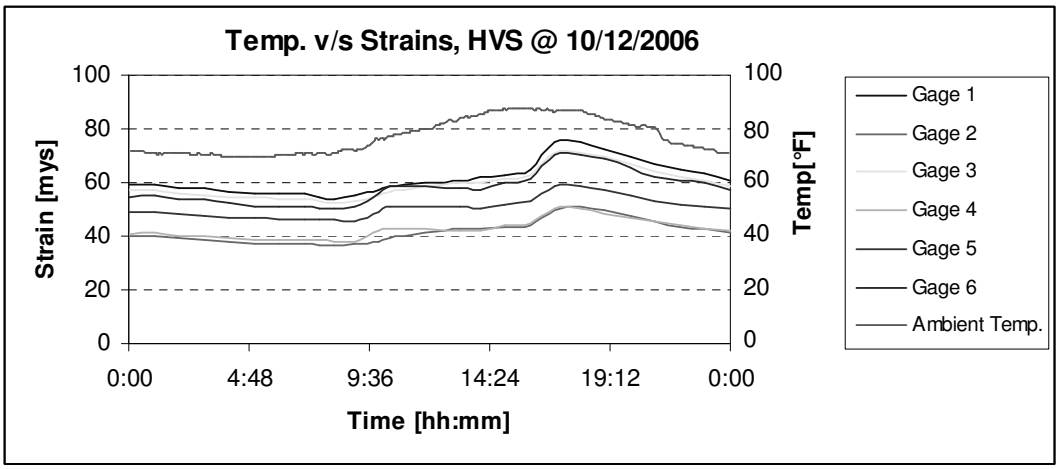


Figure 6.17 Temp. Variation vs. 2nd Peak Strains for Gages outside Wheel Path during HVS Test in Section 1B-I

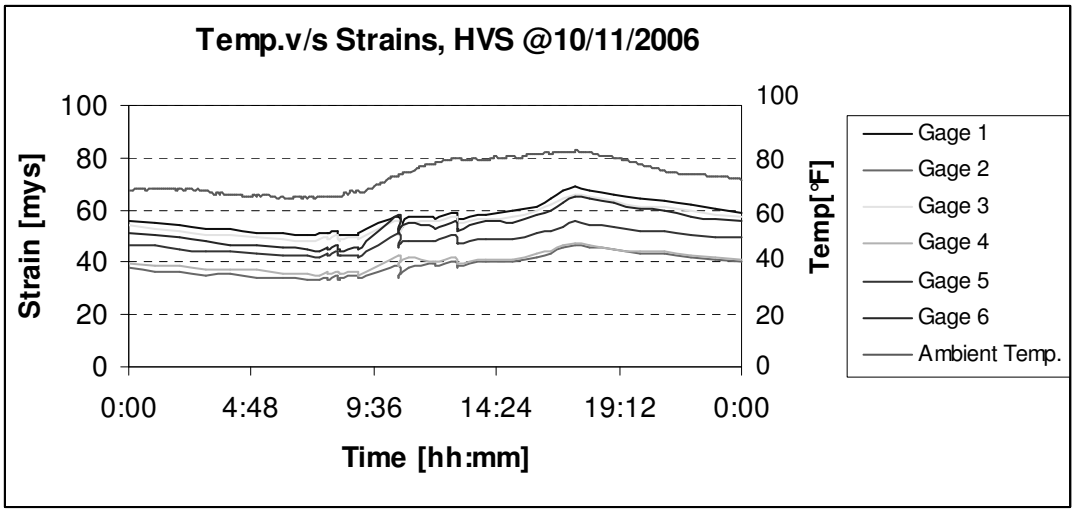


Figure 6.18 Temp. Variation vs. 2nd Peak Strains for Gages outside Wheel Path during HVS Test in Section 1B-I

### 6.1.2.2 Phase II

For Phase II, the strain gages were mounted similarly as Phase III of section 1C except for some gages that were embedded in the wheel path. Eight gages were installed perpendicular to the wheel path, one gage was installed in the longitudinal direction, and another one was mounted at the edge of wheel path. Figure 6.19 shows the actual set-up.

Strain measurements started on December 5, 2006 and ended on December 16, 2006 and it was found that strain data from the embedded gages did not look reliable, so these were abandoned. Measurements continued on January 30, 2007; after applying 1,189,455 passes, still no surface cracking developed and the HVS was stopped on February 2, 2007.

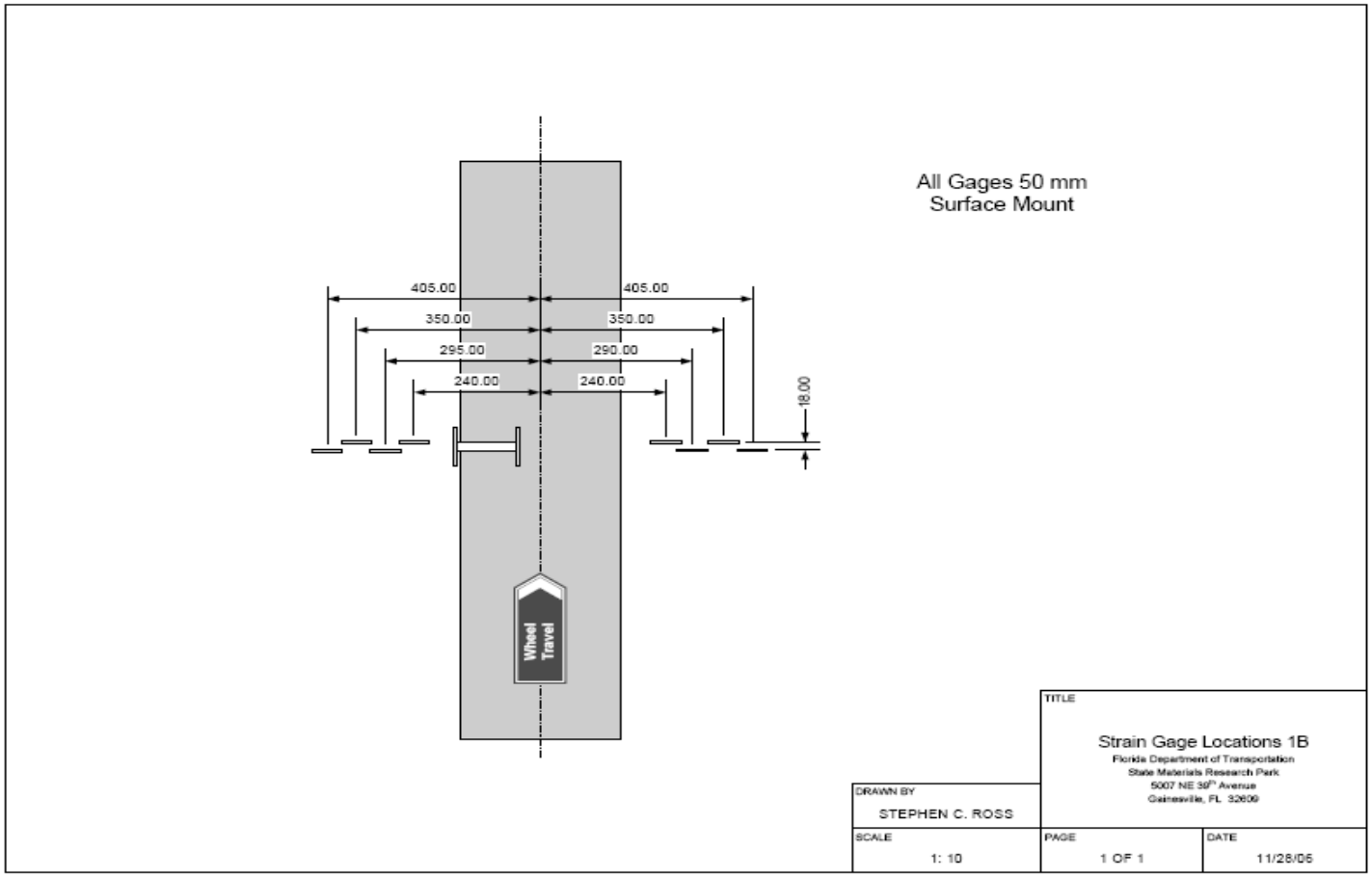


Figure 6.19 Strain Gages for Phase II in Section 1B Layout

Figures 6.20 and 6.21 show strain variation as a function of load repetitions. There was a little change in strain when load repetitions increased from 600,000 to 700,000 (Figure 6.20), and from 1,160,000 to 1,190,000 (Figure 6.21).

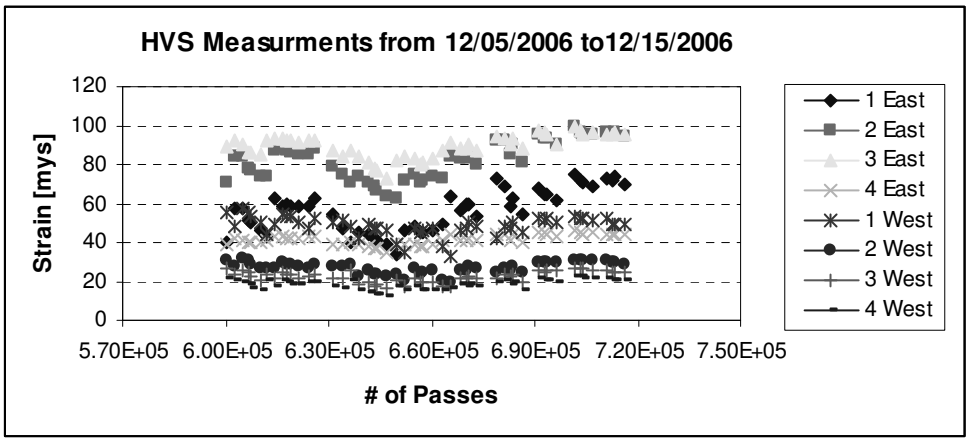


Figure 6.20 Variation of 2nd Peak Strains vs. # of Passes in Section 1B-II

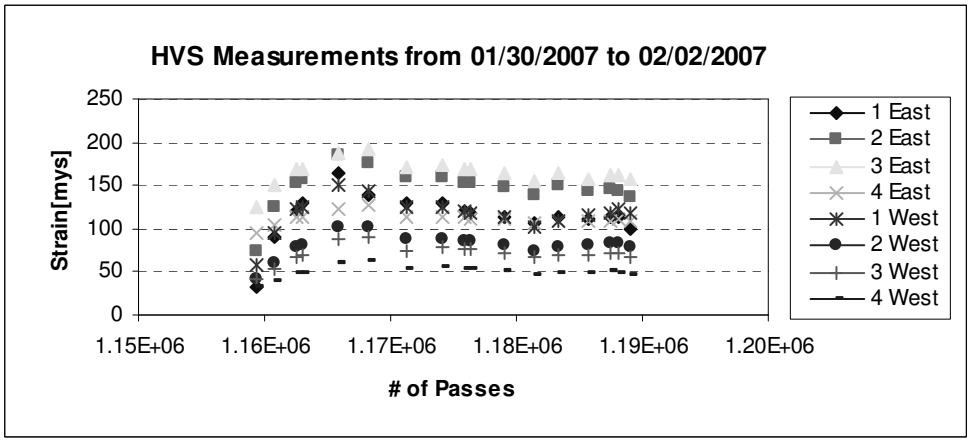


Figure 6.21 Variation of 2nd Peak Strains vs. # of Passes in Section 1B-II

### 6.1.3 Section 1A

For the mixture and pavement system at sections 1C and 1B little or no evidence of permanent (non healable) macro-damage or cracking was observed after aging with the APAS and a considerable number of load repetitions of up to 12,000 lbs were applied with and without wander. This result indirectly validated the concept that a critical condition that exceeds the energy limits of the mixture is required to cause cracking,

which is the basic premise of the HMA fracture model established by earlier FDOT research. High fracture energy and healing were likely playing a major role; therefore, section A was aged more in an attempt to minimize or eliminate healing and to reduce mixture FE. In addition, the load was increased to 18000 lb.

Loading on Section 1A at 18 kip started on February 6 and concluded on March 27 with around 488,358 passes in total. The load was near continuous with the exception of downtime for maintenance; planned and unplanned. Top down cracking was induced in the pavement where a critical combination of aging, temperature, and loading was achieved. Somewhat unexpectedly, the observed cracks were transverse in the wheelpath (Figure 6.22), which originally led to the hypothesis that thermal stresses played a major role in their development. Transverse cracks were found in the northern aged part during the coldest days of the year (February 16 to February 19 2007) at around 140,000 passes.

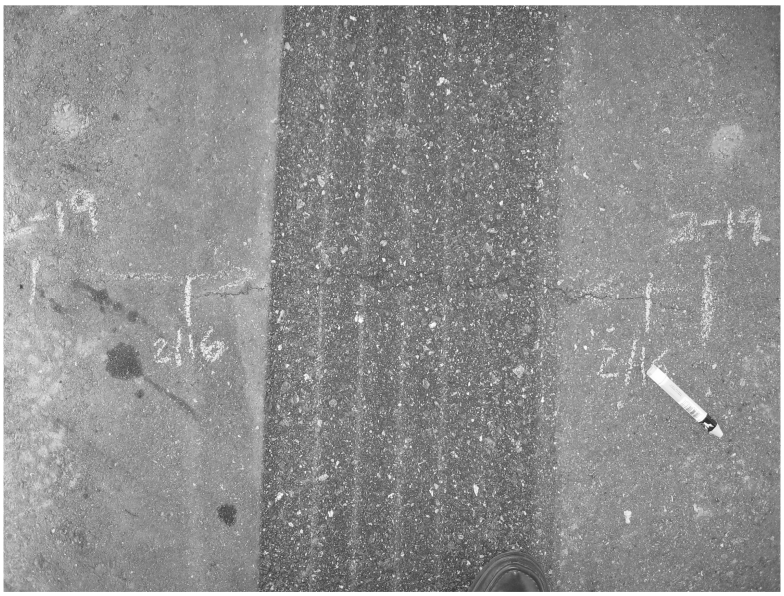

Figure 6.22 Transverse Cracking Developed in Section 1A

Interestingly, some small cracks appeared right at the edge of painted areas, Figure 6.23.

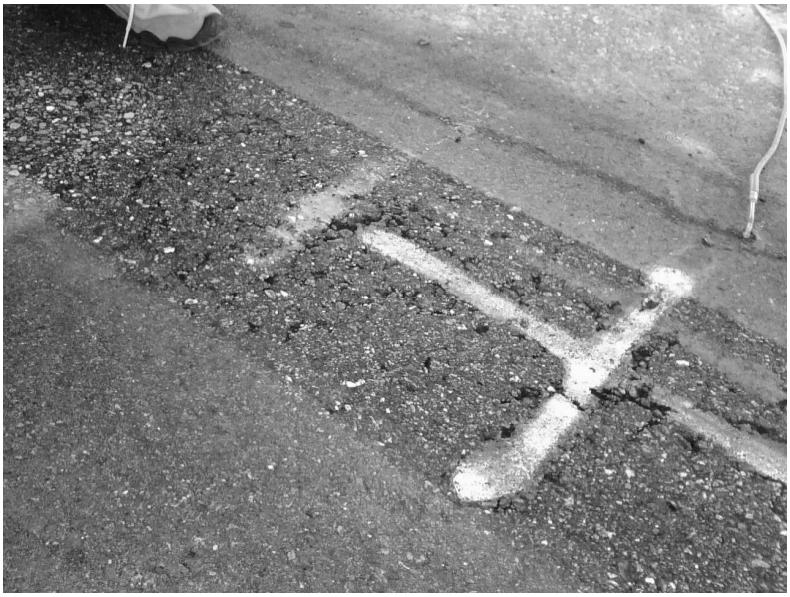

Figure 6.23 Cracking Induced at Paints in Section 1A

Only 50 mm gages were used in Section 1A. To compare strain response between aged and un-aged parts, five transverse gages were installed in each part. Those gages were used to detect potential surface cracks and installed perpendicular to the wheel path without overlap. Figure 6.24 shows the actual set-up.

To compare strain response between aged and unaged parts, five transverse gages were installed in northern and southern parts, respectively. The HVS testing started on February 6, 2007 and ended on March 27, 2007 with about 488,358 load cycles in total.

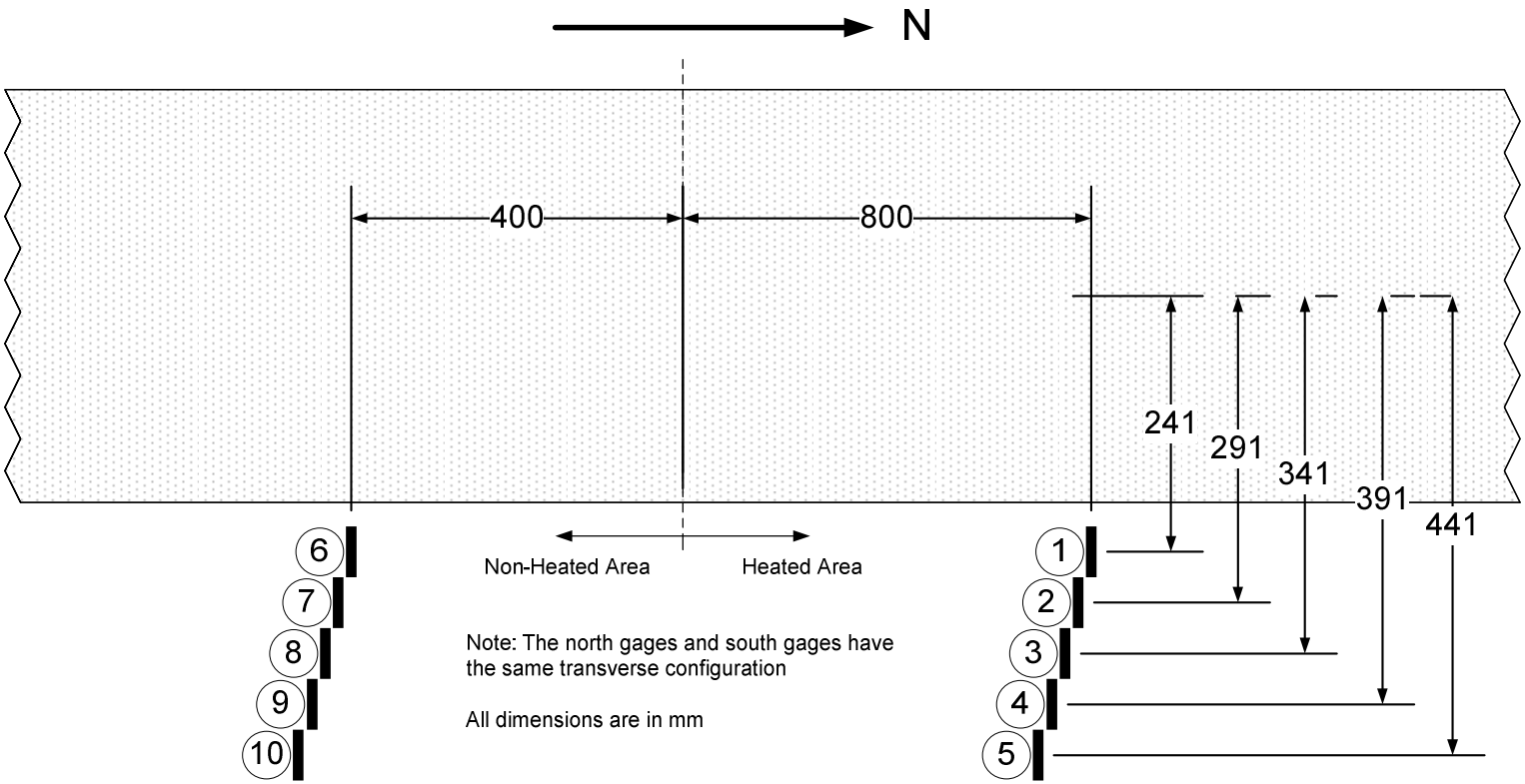


Figure 6.24 Strain Gages in Section 1A Layout

Figures 6.25 to 6.28 show how transverse strain response before/after crack developed. The temperatures showed in plots are average daily surface temperature. For both northern and southern gages, transverse strains increased as their distance to the center of wheel path increased prior to crack development, which corresponds well with strains predicted by FEM analysis for an undamaged pavement. Once the crack developed around February 18, 2007, an increase in strain was observed in northern gage 2; no such change occurred in any of the southern gages (The unaged portion).

Figure 6.26 shows that a comparable increase in strain was observed in gage 3 as loading continued after cracking was observed (2/20/2007). This was followed by a comparable increase in gages 4 and 5 on 2/21/2007, after which the time response of all gages continued to increase with continuing load repetitions from 2/21/2007 to 2/27/2007. These observations are consistent with expected changes in strain response as the crack grows.

Figures 6.27 and 6.28 show that the changes in strain response for the unaged southern section gages were modest compared to the changes observed in the aged northern section gages where cracking was observed. The fact that the general shape of the strain distribution remained the same throughout the loading period is consistent with the fact that no cracking was observed in this portion of the pavement. Also as expected, the magnitude of strains was higher in the southern section because of the lower stiffness of the unaged mixture.

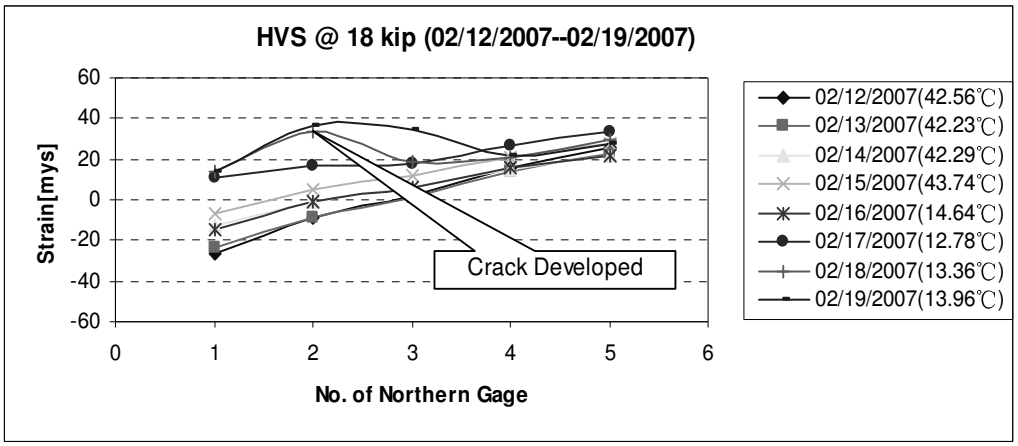


Figure 6.25 Variation of 2nd Peak Response for Northern Gages before Cracking

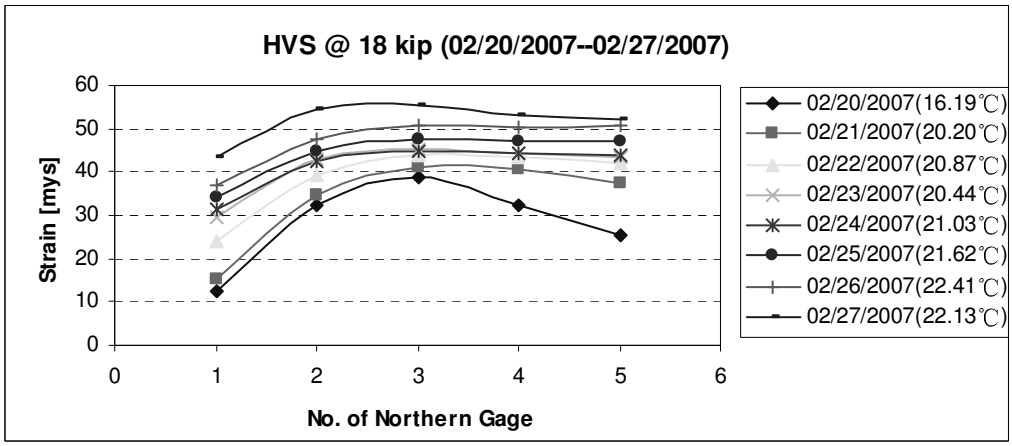


Figure 6.26 Variation of 2nd Peak Response for Northern Gages after Cracking

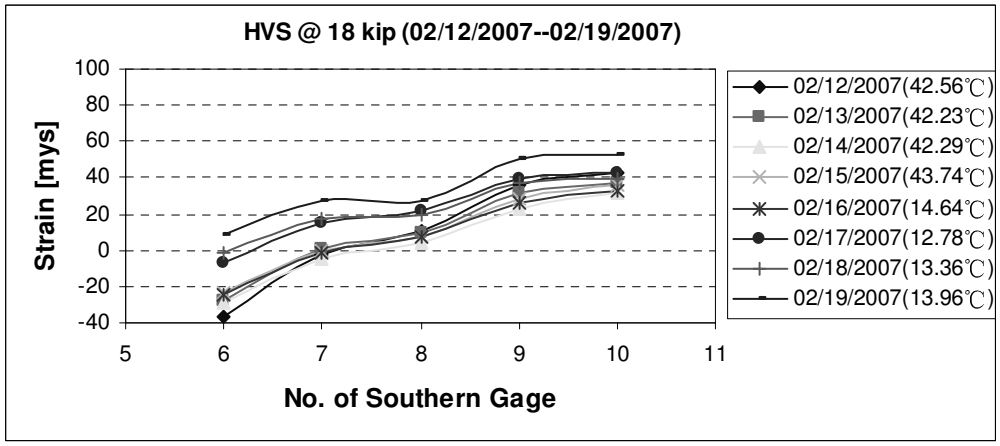


Figure 6.27 Variation of 2nd Peak Response for Southern Gages before Cracking in Northern Section

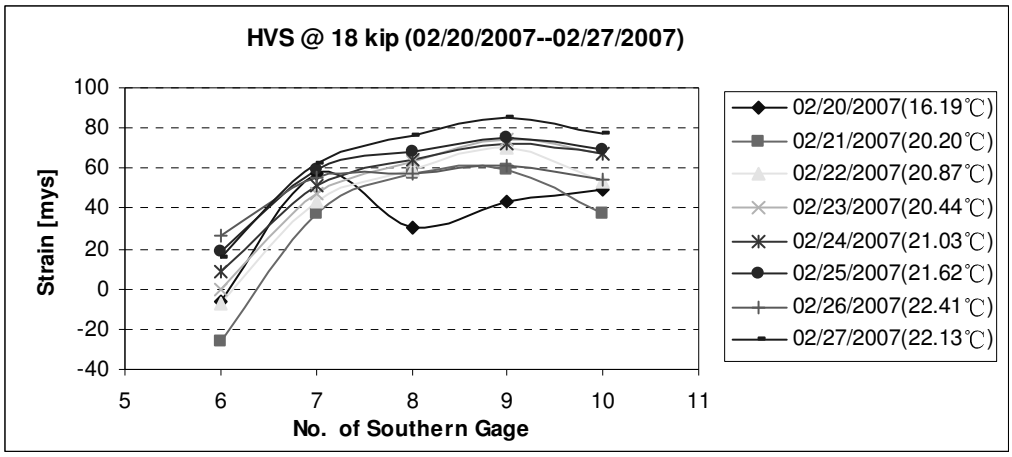


Figure 6.28 Variation of 2nd Peak Response for Southern Gages after Cracking in Northern Section

Strain variation with time can be seen in the Figures 6.29 and 6.30. It can be easily seen that strain for all gages increase with time. Once again, fatigue damage caused by load repetitions appeared to increase the strain.

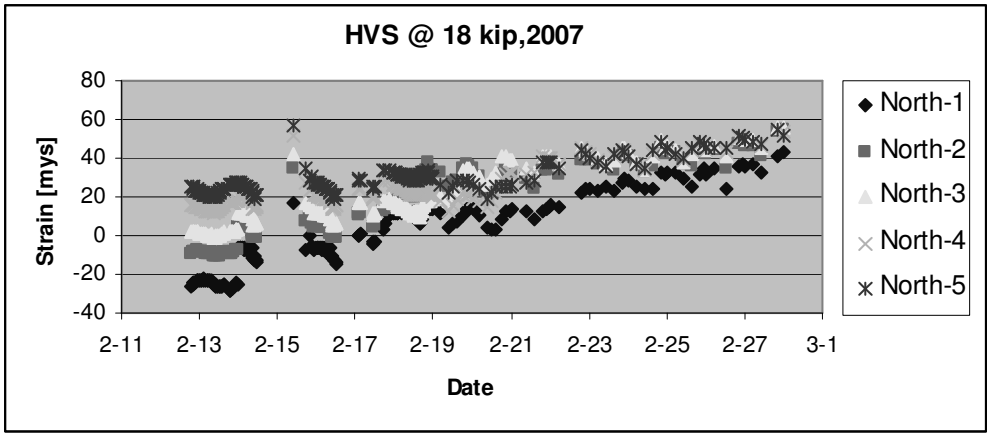


Figure 6.29 2nd Peak Responses for Northern Gages in Section 1A

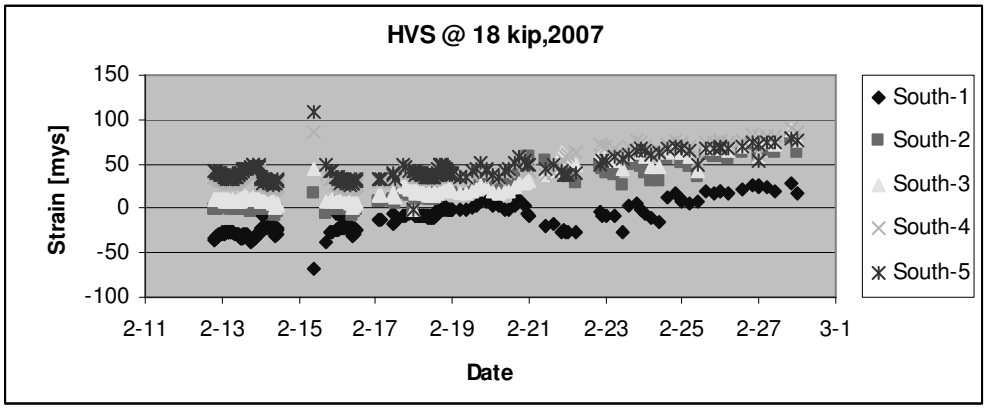


Figure 6.30 2nd Peak Responses for Southern Gages in Section 1A

## 6.2 Modeling of HVS Loading

HVS tire footprints for 6 kip, 8kip and 10 kip were obtained by FDOT, (see Figure 6.31). Based on these footprints, 6 circular loads were used for 6 kip and 8 kip loads, while 9 circular loads were needed to model the 10 kip HVS load, 2" radius each. For 12 kip and 18 kip HVS load, 30 circular loads were used, 1" radius each, (Figure 6.32). It should be noted that each circular load can be assigned with different load values based on the measured contact stress. Contact stress between tire and pavement was not measured in this project. However, previous studies by De Beer, M [1996, 1997, and 1999] and Roque successfully show how stress distributes under different tires. In this study, stress distribution was estimated based on those previous studies.

The modulus of the pavement layers were first set equal to the values from the backcalculation based on the FWD measurements a few days before the HVS loading; but the AC modulus was adjusted based on BISAR by about 20% due to some factors such as aging, fatigue and so on. The calculations were carried out at the center of the wheel at different longitudinal offsets from the transverse line of the gages, in accordance with the 7.5 mph speed of the HVS and the 0.01 s reporting rate of the data acquisition system.

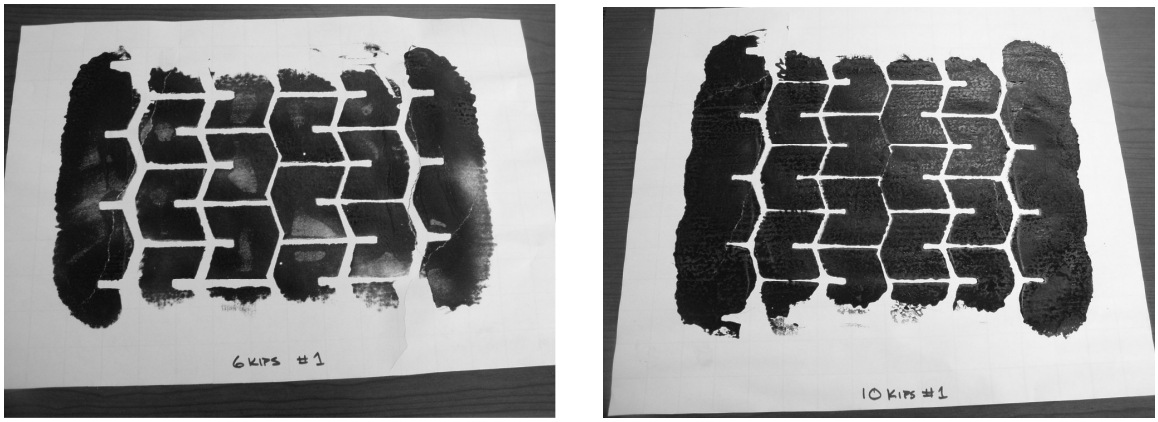


Figure 6.31 HVS Tire Footprints

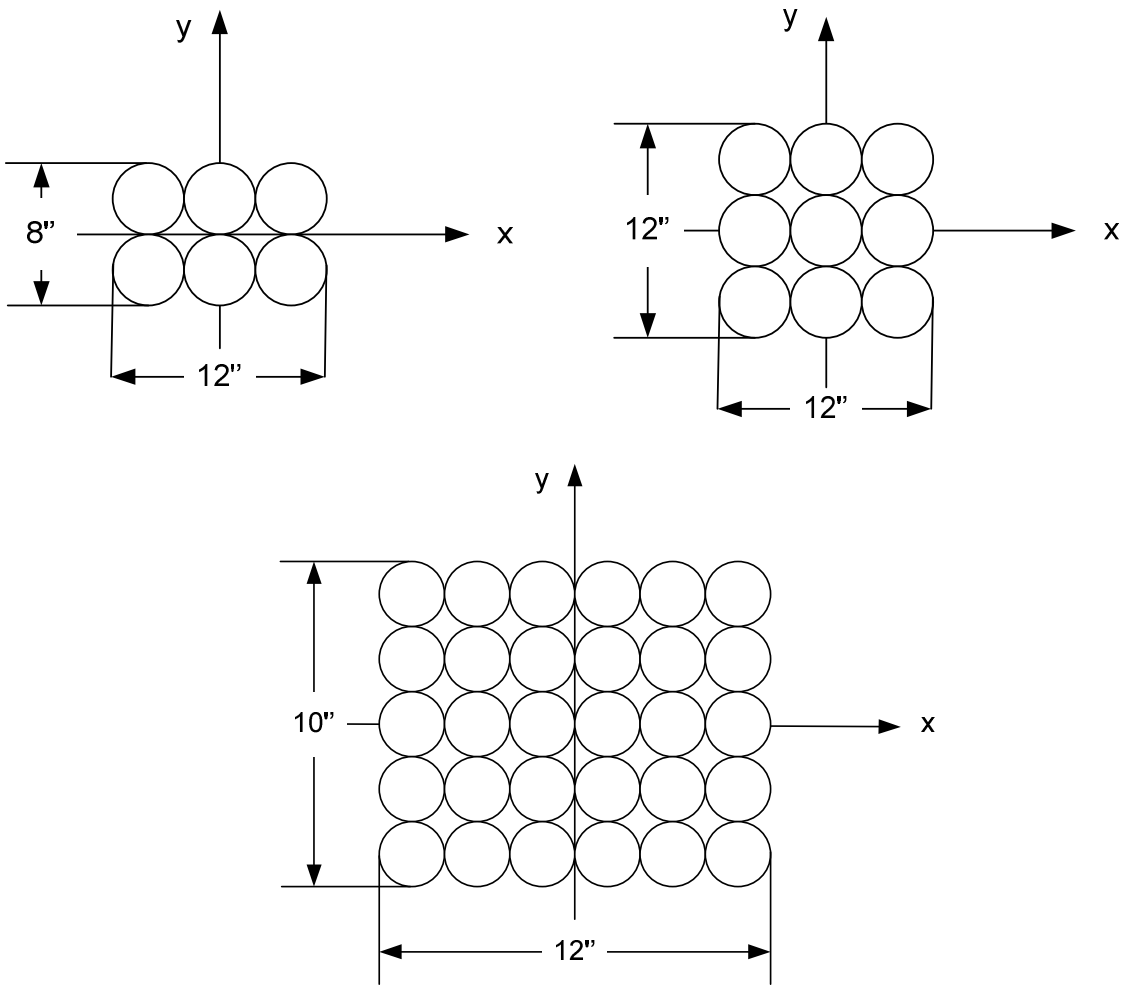


Figure 6.32 Load Configurations Used in BISAR

Figures 6.33 to 6.38 show comparisons of computed versus measured strain for various test sections and gage locations. The input data used in BISAR are also given in these figures. It can be seen that there was an excellent fit between calculated and measured strain values for both longitudinal and transverse directions, which indicates that elastic layer analysis (BISAR) can simulate HVS loading very well. Analyses with different values for the base modulus (for the entire width of the layer), shown in Figure 6.39, illustrate that a changed modulus does not affect just the calculated inner gage strain values, but also the more distant ones. A reduced base layer modulus also moves the maximum tensile value outwards.

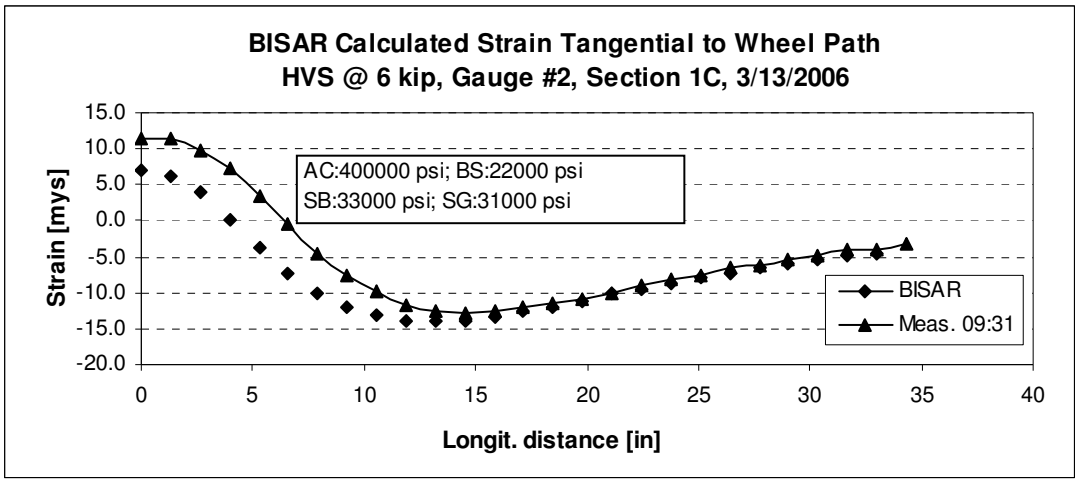


Figure 6.33 Typical Strain Comparisons at Gage 1 in Section 1C

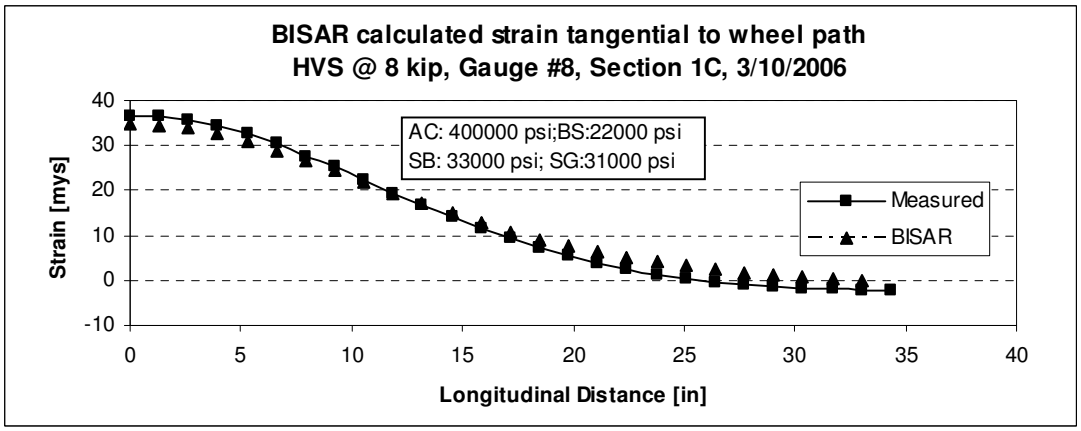


Figure 6.34 Typical Strain Comparisons at Gage 8 in Section 1C

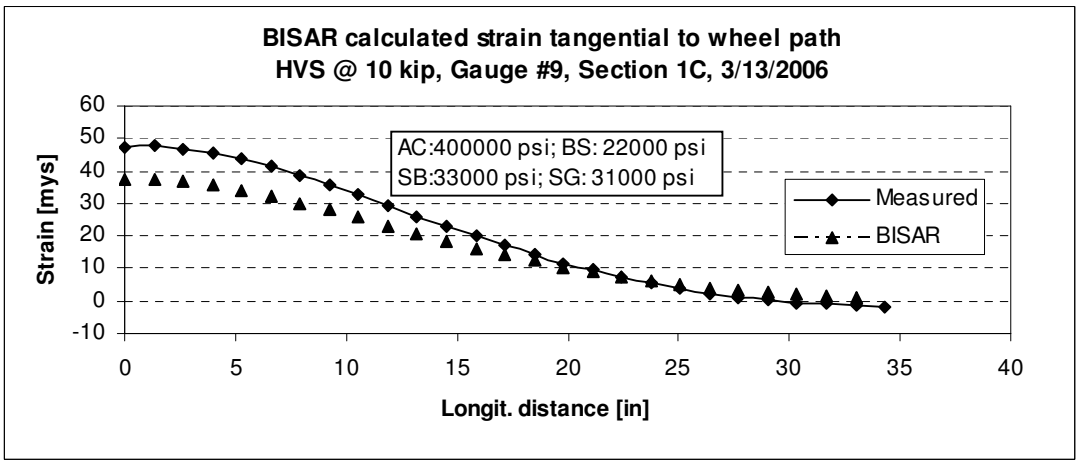


Figure 6.35 Typical Strain Comparisons at Gage 9 in Section 1C

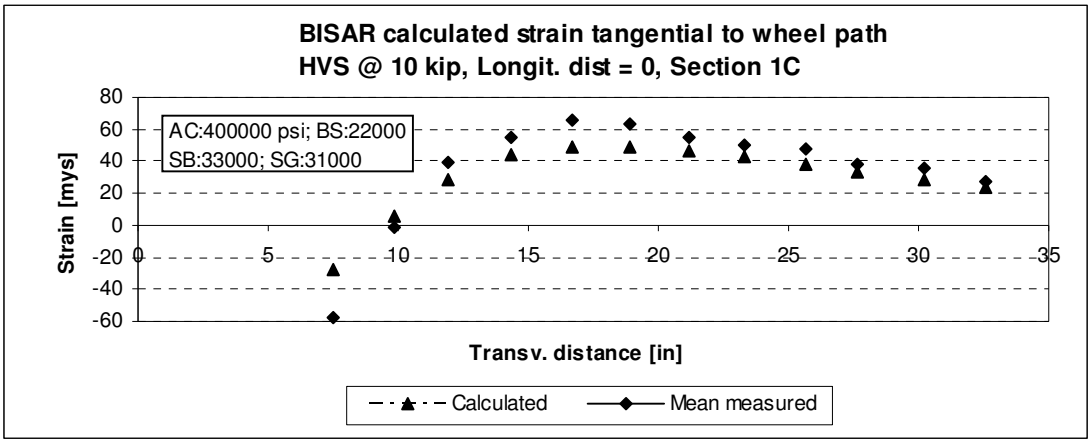


Figure 6.36 Typical Strain Comparisons at Transverse Direction in Section 1C

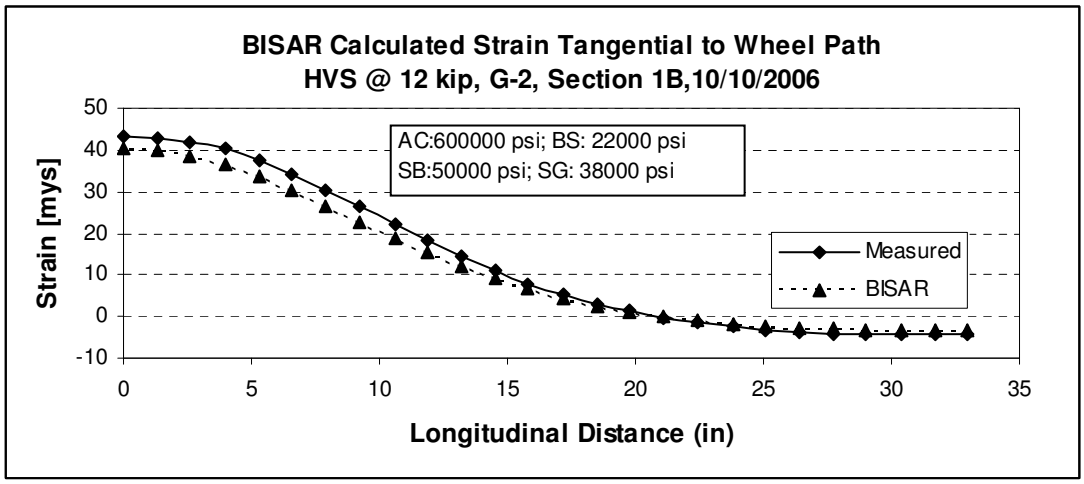


Figure 6.37 Typical Strain Comparisons at Gage 2 in Section 1B

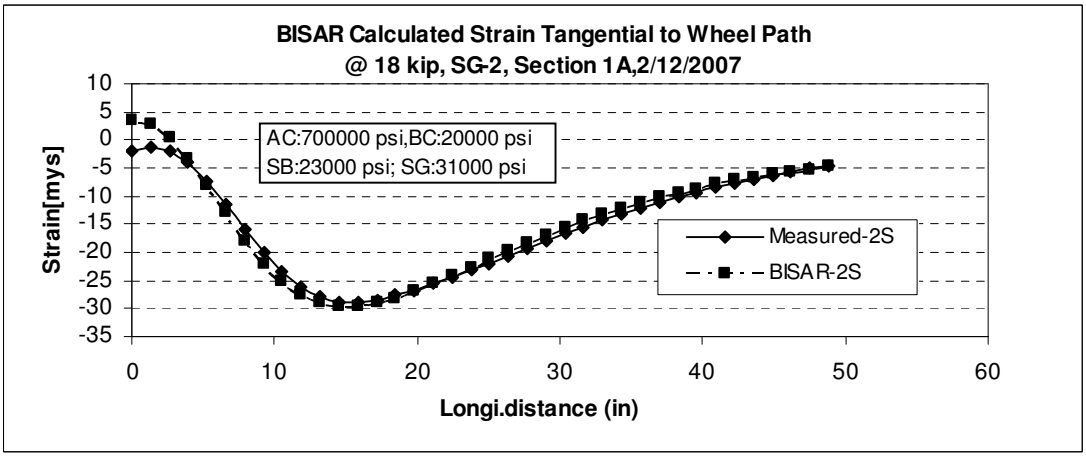


Figure 6.38 Typical Strain Comparisons at Gage 2 in Section 1A

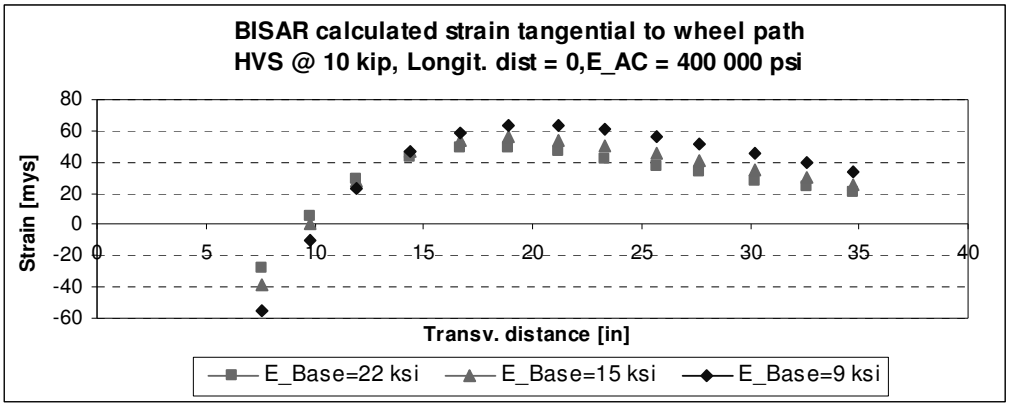


Figure 6.39 Calculated Strain Profiles for Different Base Moduli in Section 1C

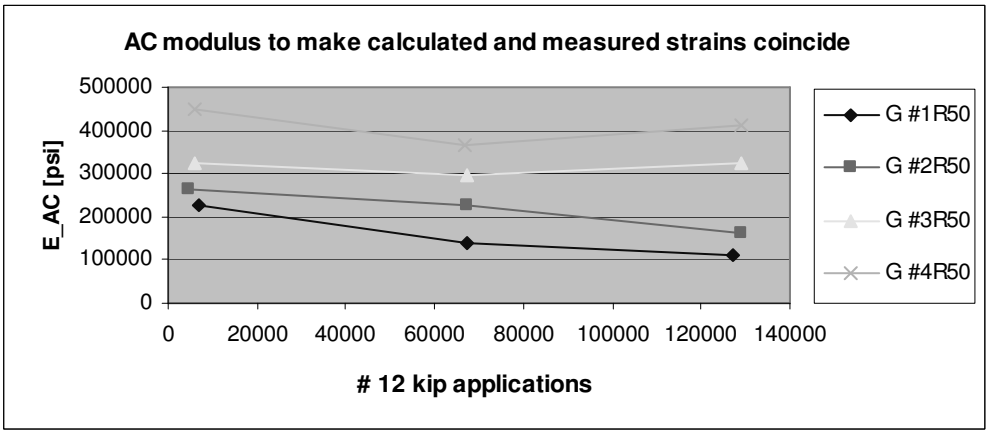


Figure 6.40 Variations of AC Modulus vs. Load Repetitions in Section 1C

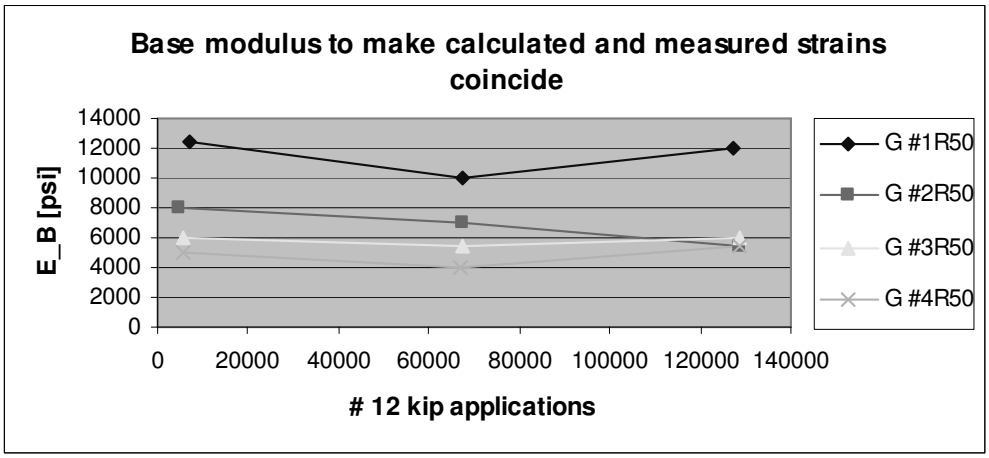


Figure 6.41 Variations of Base Modulus vs. Load Repetitions in Section 1C

It should be noted, however, that the layer moduli have to be adjusted to match the measured strains due to the increment of load cycles. Generally, only AC and base

moduli were adjusted; Figures 6.40 and 6.41 show how these parameters vary with load repetitions in section 1C. From these figures it is hard to draw a general conclusion; however, in terms of AC modulus, it was observed that the gages close to HVS wheel path seemed more affected by load cycles than those gages far from HVS, while base modulus was hardly affected by load cycles. This can be interpreted as a fatigue effect caused by load on the AC layer outweighed other environmental factors on gages near the wheel path, while temperature appeared to dominate the AC modulus on gages far from the wheel path. Groundwater level may have played a key role on base modulus.

### 6.2.1 BISAR Model

A damaged pavement was simulated in BISAR by reducing the modulus of the top third or the bottom third of the AC layer by 50 and 75 %. The effect of changing the modulus of the top part is far more pronounced than changing the modulus of the bottom part, and the effects on strains were greatest around the maximum tensile strain, (Figures 6.42 and 6.43). A reduced bottom third modulus also moved the maximum strain towards the wheel path.

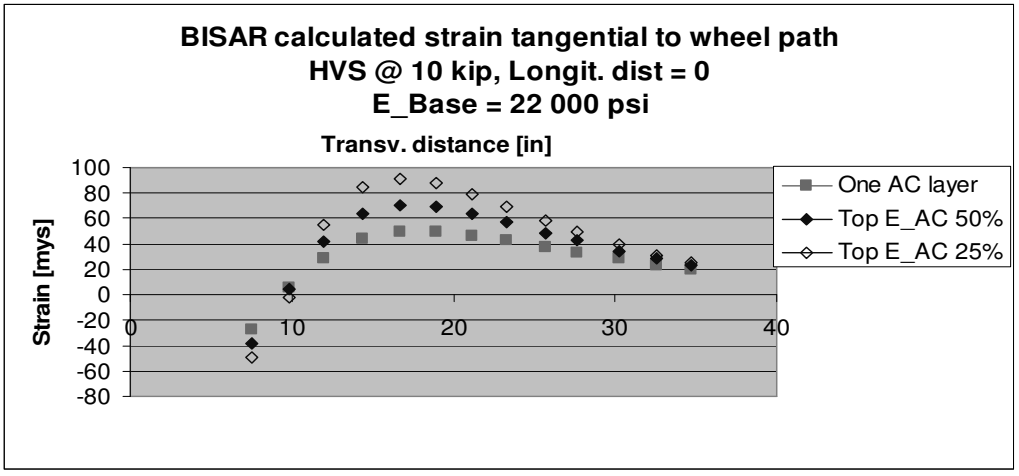


Figure 6.42 Calculated strain profiles for damaged AC layer (Top) for 10 kip HVS load

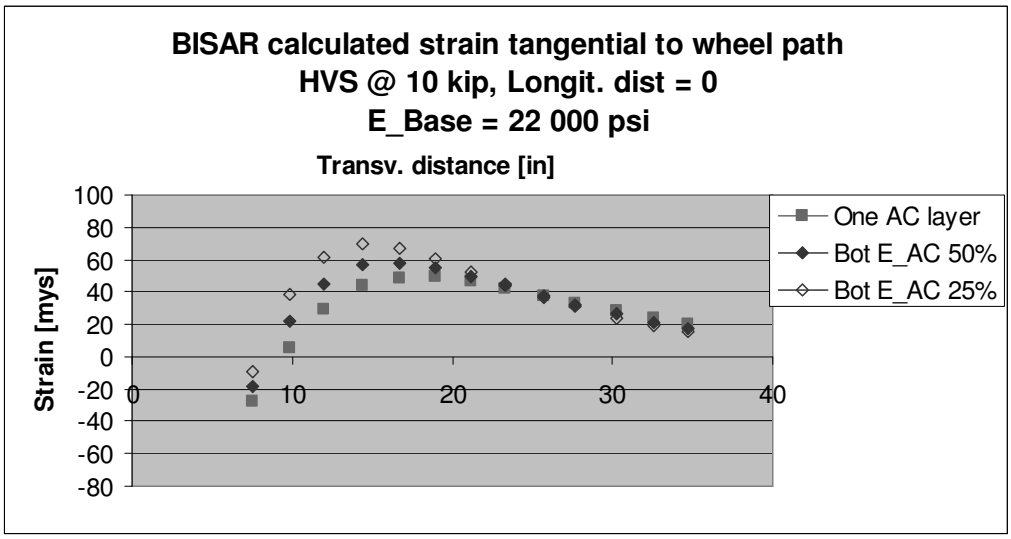


Figure 6.43 Calculated strain profiles for damaged AC layer (Bottom) for 10 kip HVS load

### 6.2.2 Axisymmetric Finite Element Model

To further evaluate how a damage zone would affect pavement stress distribution, an axisymmetric finite element model was established using the ADINA FEM computer program. The ADINA program has a very friendly user interface to build the needed models for specific applications. It can model material behavior under certain load, temperature effects and interface conditions between pavement layers. The program is able to automatically create finite element meshes based on boundary definitions and density specifications; it also has a powerful post-processor to generate results both numerically and graphically.

The 4-layer pavement structure used for the finite element analysis (FEA) is shown in Figure 6.44.

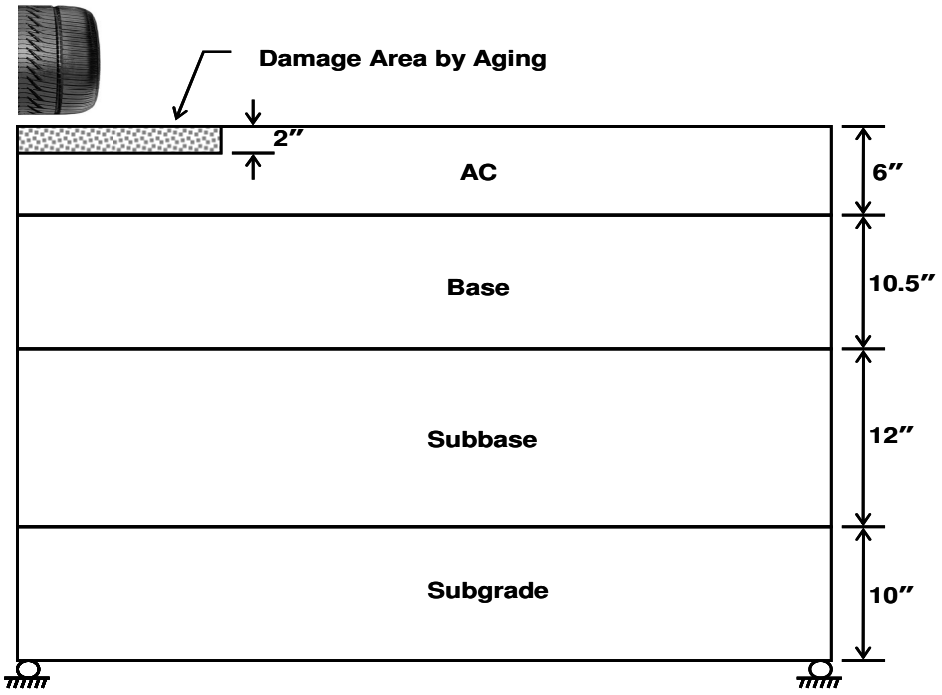


Figure 6.44 Pavement Structure for FEA

To simulate damaged properties at the top of the AC surface, a 2" thick layer was modeled for varied width from 0" to 24". In other words, the damage area in the model varied from 0" to 12" due to symmetry.

The modulus of elasticity and Poisson ratio shown in Table 6.2 were used for analysis and estimated based on the backcalculation data from FWD. For the simulated damaged area, the modulus of the AC layer was reduced by 50%; in other words, 200,000 psi was used.

Table 6.2 Material Properties for Each Layer

| Layer | AC | Base | Subbase | Subgrade |
|---|---|---|---|---|
| **Modulus, psi** | 400,000 | 22,000 | 33,000 | 31,000 |
| **Poisson ratio** | 0.40 | 0.35 | 0.35 | 0.35 |

Since Axisymmetric model elements were used, the load was circular with a radius of 6" and 120 psi pressure.

To visualize stress and strain variation after crack initiation on the surface, a 1" depth crack was modeled 16" away from the center, where the highest tensile stress was found in the model without crack. Without changes in geometry, nodes for a crack were disconnected to adjacent nodes for 1" depth from the surface downwards.

Even though there was small difference in tensile stress between peak values with and without damage, the results were generally very similar except for the center (Figure 6.45). The compressive stress for the case of no damage was larger than for the damaged condition; however, more damaged area showed the highest tension around 16" from the center, but the difference was quite small.

The strain values shown in Figure 6.46 followed the same trend as stress, but the compressive strain without damage was smaller than with damage. The tensile strain at the peak with damage was a little higher than without damage. The wider damaged area showed the highest stress and strain values as expected, but the differences were small.

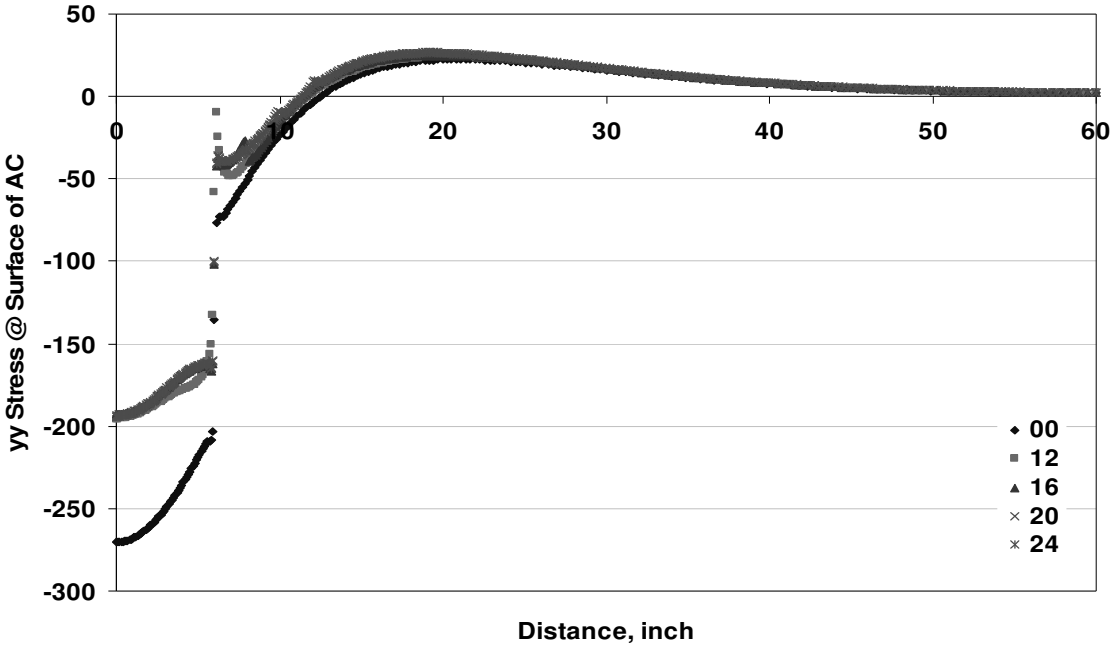


Figure 6.45 Horizontal Stress at AC Surface without Crack (+: tension, -: compression)

Figures 6.47 and 6.48 illustrate that the tensile stress around the crack on the surface was nearly zero. The strain next to the crack was also significantly reduced.

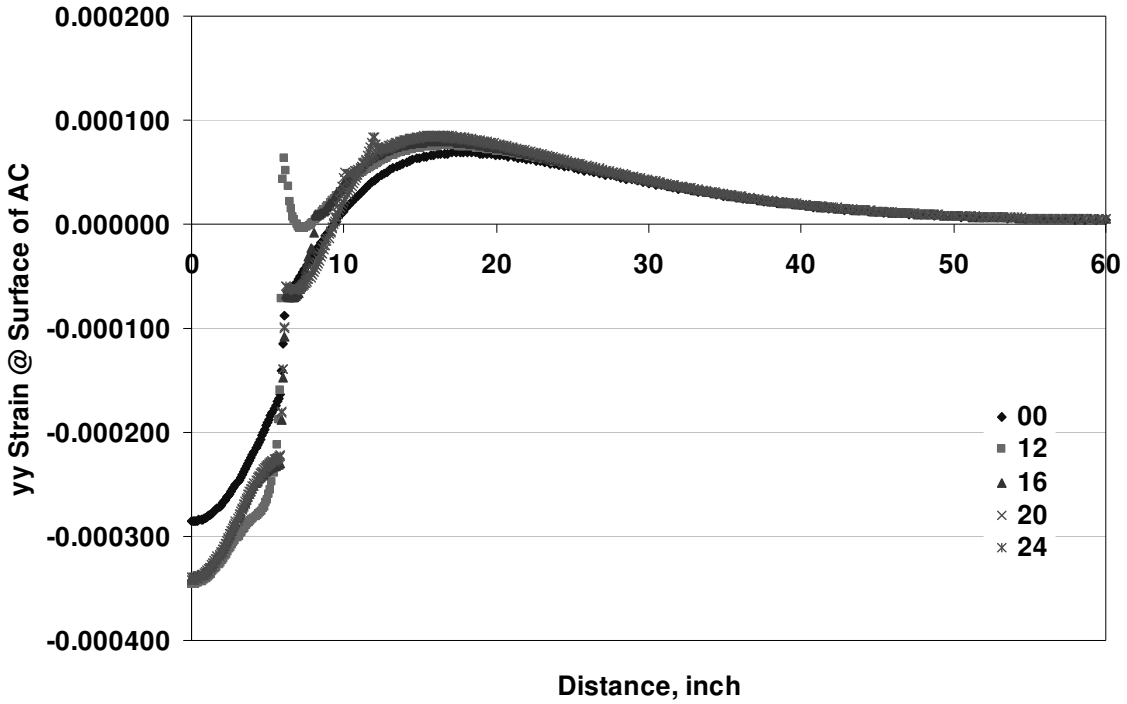


Figure 6.46 Horizontal Strain at AC Surface without Crack (+: tension, -: compression)

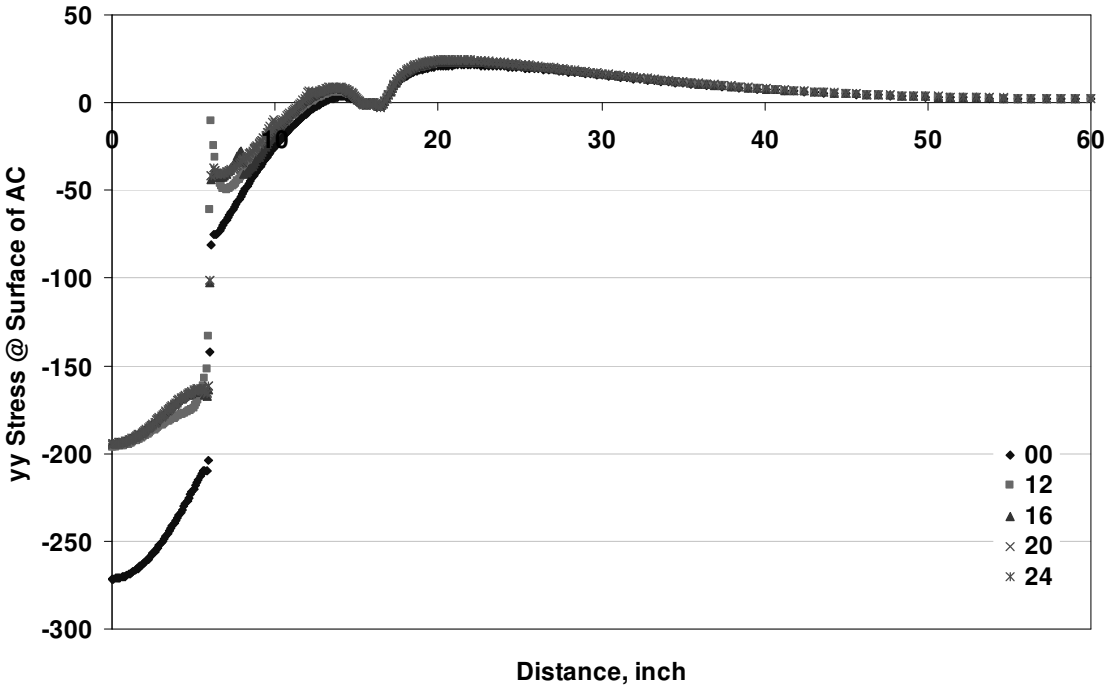


Figure 6.47 Horizontal Stress at AC Surface with crack (+: tension, -: compression)

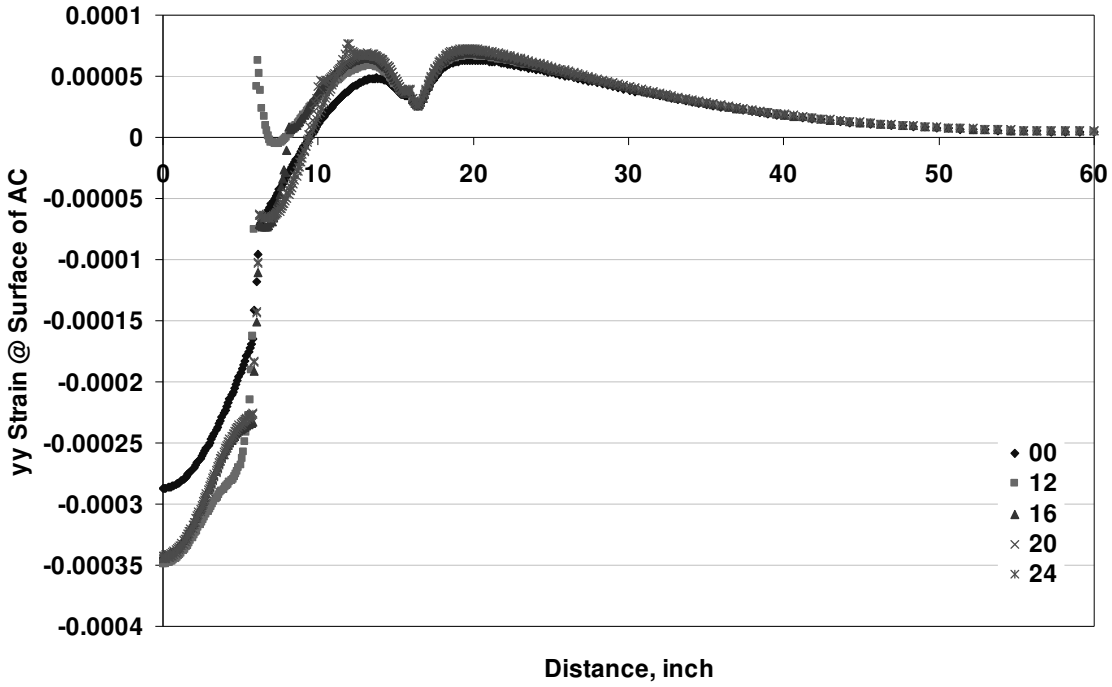


Figure 6.48 Horizontal Strain at Surface with crack (+: tension, -: compression)

In summary, both BISAR and axisymmetric finite element models show that damage would lead to increase of AC surface tensile stress/strain, but the increment is very limited. These analysis methods seem to indicate that it may be difficult to discover any developing distress area just by using surface strain gages; in addition, the FEM analyses indicate that unless a strain gage coincidentally spans across a crack, it could also be difficult to discover that a surface crack is present. Therefore, strain gages are good for response but not particularly good for crack detection.

### 6.3 Effect of consolidation rutting on stress distributions

One of the main goals of this project was to study and evaluate the mechanism of top-down cracking under APT testing. Field observations have indicated that top-down cracks are surface-initiated longitudinal wheel path cracks. Although APT testing successfully initiated several transverse wheel path cracks in section 1A, it did not initiate

longitudinal wheel path cracks successfully. One reason was that an extremely good performing AC mixture was used. It was also hypothesized that the AC surface at the APT did not induce the same stresses as in the field pavement. An AC surface in the field with cross-slope and rutting, may significantly affect surface horizontal tensile stress caused by wide-base tires, which may explain the presence of longitudinal top-down cracking. A 2D finite element model based on ADINA was established to study how the pavement surface with rutting affects the surface tensile stress distribution. Emphasis was placed on evaluation of SIGMA-3 (Minor principal stress, and therefore the highest level of tension at a given point) next to the tire. The model also studied the effects of pavement structure and material properties on the AC surface SIGMA-3 distribution.

Two wide-base tires (110 psi tire inflation pressure) were linked with an extremely stiff axle. Figure 6.49 shows the FEM mesh of the entire model. Two different surface conditions, i.e. flat surface and rutted surface, were also modeled based on ADINA, see Figure 6.50 and 6.51. Two contact surfaces were defined to model the contact conditions between tire and AC rutted surface, which is shown in Figure 6.52. Pavement structure and material properties for 4-inch AC and 8-inch AC are given in tables 6.3 and 6.4, respectively. Tire parameters for the 2D model are given in table 6.5.

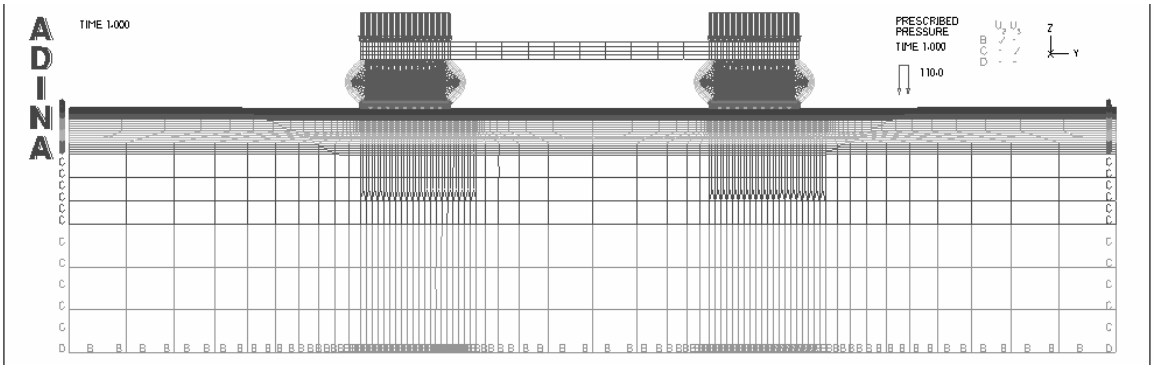


Figure 6.49 2D FEM with wide-base single tire


Figure 6.50 Pavement surface without rutting


Figure 6.51 Pavement surface with rutting

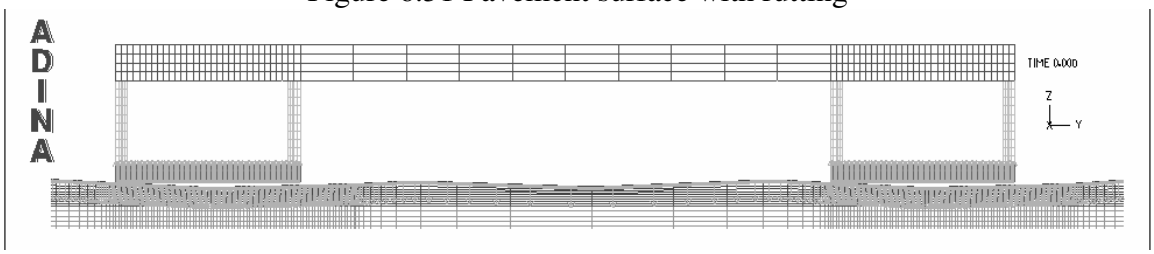


Figure 6.52 Contact conditions between tire and pavement rutting surface

Table 6.3 Pavement structure and material properties for 4-inch case

| Layer | | Thickness (in) | Modulus (psi) | | |
|---|---|---|---|---|---|
| | | | Normal | Stiffness Gradient (SG) | Poisson's Ratio |
| AC | Layer 1 | 1 | 1.00E+06 | 1.20E+06 | 0.4 |
| | Layer 2 | 1 | 1.00E+06 | 8.00E+05 | 0.4 |
| | Layer 3 | 2 | 1.00E+06 | 4.00E+05 | 0.4 |
| BS | Layer 1 | 4 | 1.00E+05 | 1.00E+05 | 0.35 |
| | Layer 2 | 12 | 4.00E+04 | 4.00E+04 | 0.35 |
| SB | | 22 | 2.00E+04 | 2.00E+04 | 0.35 |

Table 6.4 Pavement structure and material properties for 8-inch case

| Layer | | Thickness (in) | Modulus (psi) | | |
|---|---|---|---|---|---|
| | | | Normal | Stiffness Gradient (SG) | Poisson's Ratio |
| AC | Layer 1 | 1 | 1.00E+06 | 1.20E+06 | 0.4 |
| | Layer 2 | 1 | 1.00E+06 | 8.00E+05 | 0.4 |
| | Layer 3 | 2 | 1.00E+06 | 4.00E+05 | 0.4 |
| | Layer 4 | 2 | 1.00E+06 | 2.00E+05 | 0.4 |
| | Layer 5 | 2 | 1.00E+06 | 1.00E+05 | 0.4 |
| BS | | 12 | 4.00E+04 | 4.00E+04 | 0.35 |
| SB | | 22 | 2.00E+04 | 2.00E+04 | 0.35 |

Table 6.5 Material properties for tire

| | Tire Parts | | | | |
|---|---|---|---|---|---|
| | **Tire Tread (Rubber)** | **Tire Sidewall (Rubber)** | **Tire Grooves (Air)** | **Reinforcing Beads (Steel)** | **Rim (steel)** |
| **Modulus, psi** | 1160 | 5000 | 9.8E-6 | 2.9E7 | 1.0E10 |
| **Poisson ratio** | 0.48 | 0.45 | 0.499 | 0.15 | 0.10 |

Figures 6.53 to 6.55 and table 6.6 show SIGMA-3 evaluation; the main points from this analysis are summarized as follows:

- Large tensile stress (SIGMA-3) develops at the tire edge for both flat and rutted surface. The stress decreases dramatically with the increased distance from the tire edge, see Figures 6.53 and 6.54.
- Tensile stress in the rutted surface was 60% greater than in the flat surface, which clearly shows that the rutted surface had a significant effect on the surface tensile stress.
- Figure 6.55 and table 6.6 clearly indicate that pavement structure and material properties had very little effect on SIGMA-3, which indicates that initiation of top down cracking may not be strongly related with pavement structure.

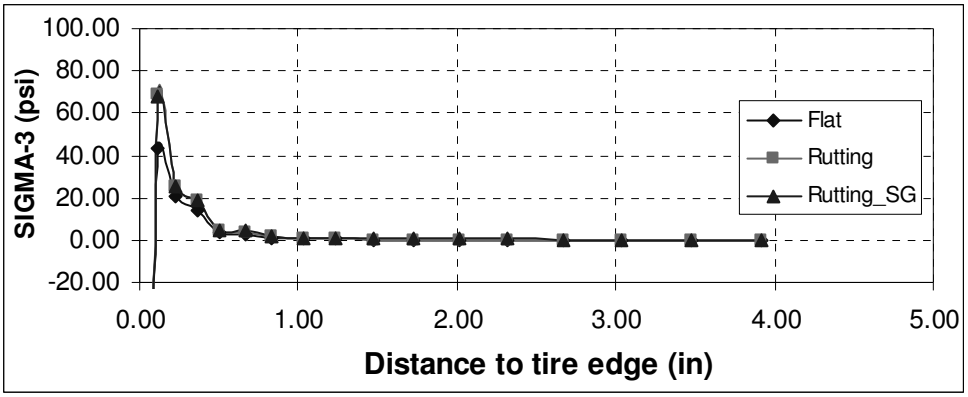


SG: Stiffness Gradient

Figure 6.53 Comparison of SIGMA-3 at AC Surface (4-inch Case)

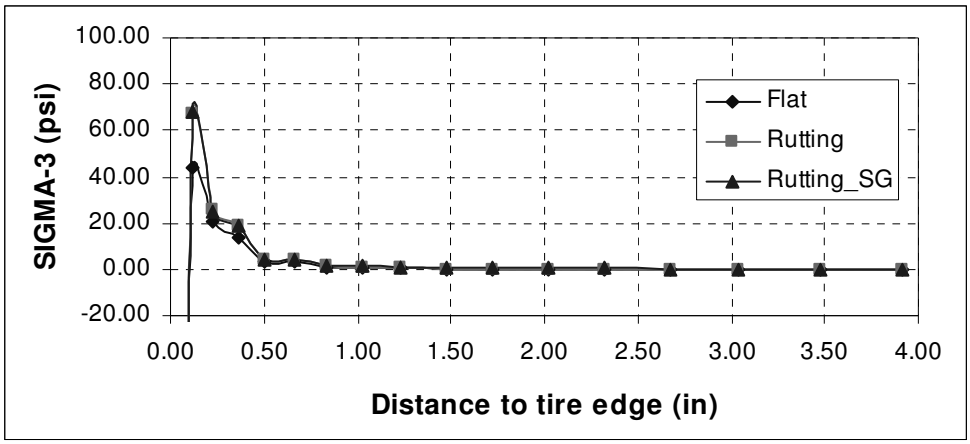


SG: Stiffness Gradient

Figure 6.54 Comparison of SIGMA-3 at AC Surface (8-inch Case)

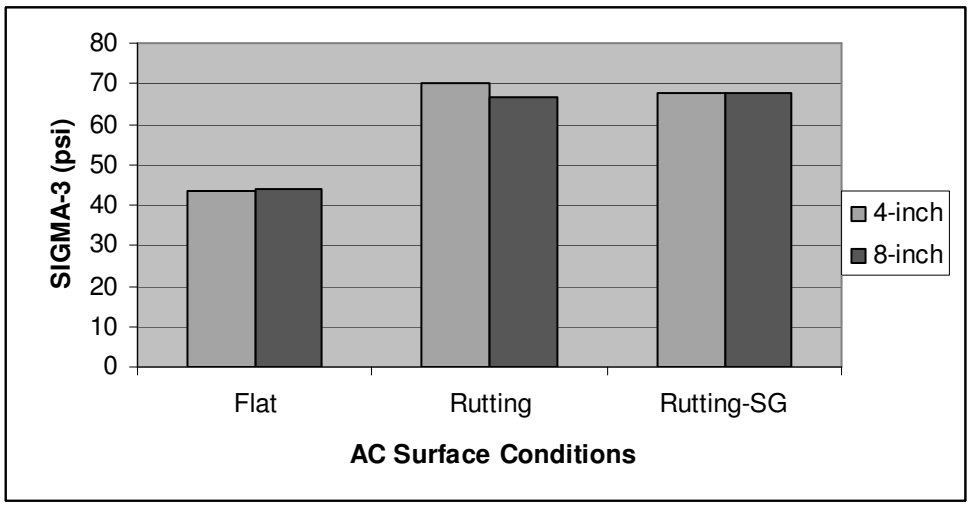


SG: Stiffness Gradient

Figure 6.55 Comparison of Maximum SIGMA-3

Table 6.6 Statistical results of 2D FEM analysis

| AC Thickness | **Flat Surface** | **Rutting Surface** | |
|---|---|---|---|
| | | **Uniform Stiffness** | **Gradient Stiffness** |
| | SIGMA-3 (psi) | SIGMA-3 (psi) | SIGMA-3 (psi) |
| 4in | 43.66 | 69.91 | 67.77 |
| 8in | 43.83 | 66.89 | 67.68 |

### 6.4 DCSE Analysis for Crack Initiation at Section 1A of HVS Project

It was recorded that HVS loading on Section 1A at 18 kip commenced on 02/06/07 and completed on 03/27/07 with around 488,358 passes in total. A transverse crack was found in the northern (aged) part of this section on 02/18/07. This observation is of great

value and was used to validate our analytical approaches on initiation of surface crack in HMA material under cyclic loading. In this part of the report, analyses based on those approaches will be performed. The primary objectives of the analysis were as follows:

- To evaluate and compare the effects on crack initiation due to load-associated stress and thermal-associated stress.
- To investigate the likelihood of transverse and longitudinal surface cracking in the APT with HVS loading.
- To assess the soundness of our approaches on prediction of crack initiation

### 6.4.1 DCSE due to load-associated stress

The approach on computation of dissipated creep strain energy (DCSE) due to load-associated stress has been well documented in HMA Fracture Mechanics developed by Zhang et al. (2001) and Roque et al. (2002). The applications of the model in this project are summarized below.

The linear elastic multi-layer analysis program LEA was used to predict the HVS load-associated stress of the asphalt pavement tested. The typical load configuration used in LEA is shown below (Figure 6.56).

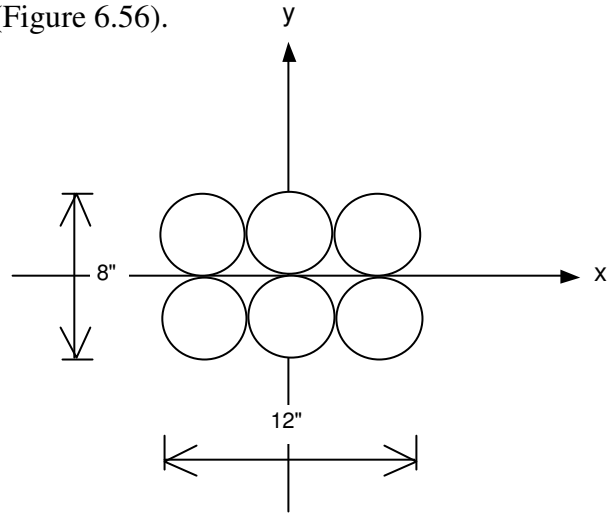


Figure 6.56. Typical load configuration used in LEA

The pavement structure modeled by LEA is shown in Table 6.7. It is noted that the AC layer was divided into three sub-layers to consider stiffness gradients in the AC layer due to aging effects.

Table 6.7. Pavement structural characteristic used by LEA

| | E | *v* | h |
|---|---|---|---|
| | (psi) | | (in) |
| AC | 1.80E+06 | 0.35 | 1.5 |
| | 1.20E+06 | 0.35 | 1.5 |
| | 6.00E+05 | 0.35 | 3.0 |
| Base | 4.00E+04 | 0.35 | 10.5 |
| Subgrade | 3.10E+04 | 0.4 | Inf. |

The 3-D view of tire load with the direction of movement is shown in Figure 6.57. It was found from LEA results that two locations exist where the load induced horizontal surface tensile stress is high. The first one is along the wheel path (around 25 in. away from the tire), where the maximum longitudinal tensile stress ocurrs. The second is in the direction perpendicular to the wheel path (about 20 in. away from the tire edge) where the maximum transverse tensile stress ocurrs. These two stresses were determined to be of similar magnitude (about 40 psi). However, as indicated earlier there is a third location with high tensile stress that LEA is not able to capture. According to the preliminary 2-D FEM analysis, the third location is found right at the tire edge subjected to a principal tensile stress $\sigma_3$. In those analyses, contact elements were defined between the tire and a rutted asphalt pavement surface. The contact effect and rutted AC surface resulted in a tensile stress of 66.9 psi for the pavement structure evaluated, which is higher than the 40 psi determined away from the tire. Further experimental evaluation of this phenomenon would require the design of a system that can reliably identify the development of damage in the pavement surface.

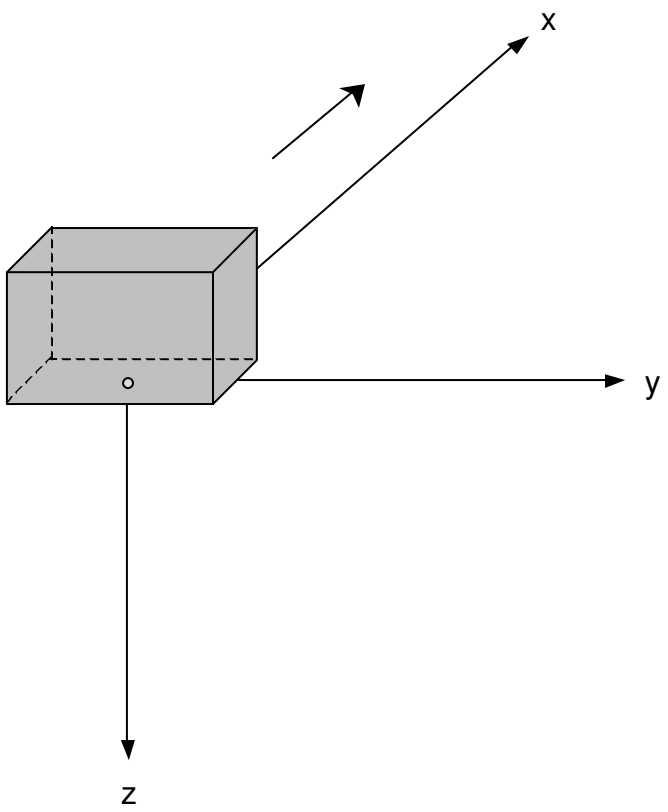


Figure 6.57 Schematic 3-D view of tire load with direction of movement

DCSE computations were performed for two typical distributions of surface tensile stress during one pass of the HVS tire load. Figure 6.58 (a) shows the longitudinal tensile stress distribution with 2 peaks corresponding to the stresses experienced at one typical location along the wheel path during one pass. Figure 6.58 (b) shows the transverse stress distribution, with only one peak (and much shorter duration), representing stresses experienced either right at the tire edge or at around 20 in. away from tire edge during one pass. It is clear from the schematic drawing that longitudinal stress had much longer duration than both the transverse maximum bending stress and principal tensile stress for one pass.

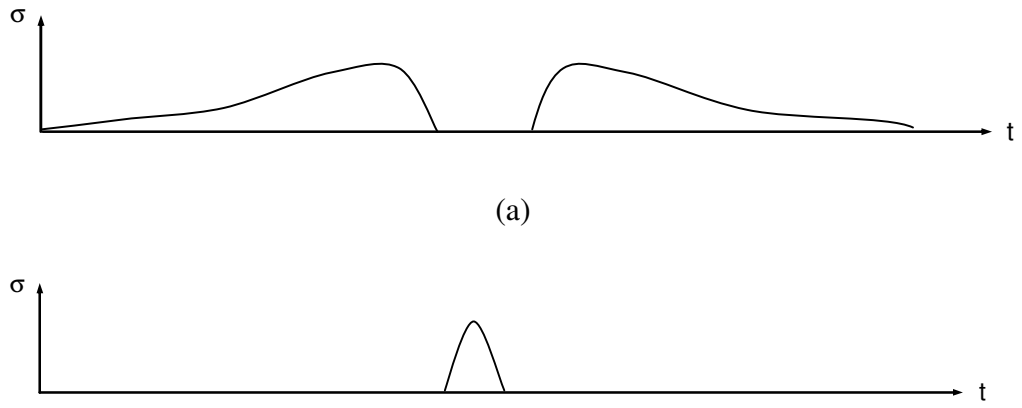


Figure 6.58 Surface tensile stress during one pass of HVS tire load

Based on HMA fracture mechanics, the DCSE due to load-associated stress can be calculated using creep compliance parameters (obtained from the SuperPave IDT creep test (Buttlar and Roque, 1994)) and the characteristics of the applied stress. The general expression for the dissipated creep strain energy per cycle is given as follows:

$$DCSE / cycle = \int_0^p \sigma(t)\dot{\varepsilon}_{cr}(t)dt \quad (1)$$

where: $\sigma(t) = \sigma_0 f(t)$, representing stress in the location of interest

$\sigma_0$ = peak value of the stress function

$\dot{\varepsilon}_{cr}(t)$ = creep strain rate

$p$ = time during of the stress

The creep strain rate can be estimated as the maximum creep strain rate from SuperPave IDT creep test at 1000 seconds. Based on the relationship between strain and creep compliance:

$$\varepsilon(t) = \sigma_0 \cdot D(t) \qquad (2)$$

where $D(t)$ = creep compliance and can be represented using the following power function:

$$D(t) = D_0 + D_1 \cdot t^m \qquad (3)$$

where $D_0$, $D_1$, and m are parameters determined from creep tests.

The rate of creep strain is thus obtained as below

$$\dot{\varepsilon}_{cr}(t) = \sigma_0 D_1 m t^{m-1} \qquad (4)$$

By substitution and simplification, one can obtain the following relationship

$$DCSE / cycle = \sigma_0^{\,2} D_1 m (1000)^{m-1} \cdot \Delta t \qquad (5)$$

where $\Delta t$ is the time duration obtained from the integral of time function.

It is noted that an average temperature of 10 $^{o}$C was adopted when applying equation (5) in this analysis. The load-associated DCSE is thus computed based on material properties at 10 $^{o}$C. A parametric study was also conducted to investigate the effect of temperature (10, 15, and 20 $^{o}$C) on DCSE. As shown in Figure 6.59, the DCSE accumulation is much faster at the temperature of 20 $^{o}$C. It is also of interest to observe that the predicted time of crack initiation based on the temperature of 15 $^{o}$C is very close to the actual time when cracking occurred. Although the precise average temperature is not known, the actual behavior of DCSE accumulation can be well bounded by the results covering a range of temperature between 10 and 20 $^{o}$C for this project.

A more rigorous approach, considering the variation of material properties with transient temperature, was also investigated. However, additional work is required to develop the models necessary to properly consider these effects. These efforts are currently underway.

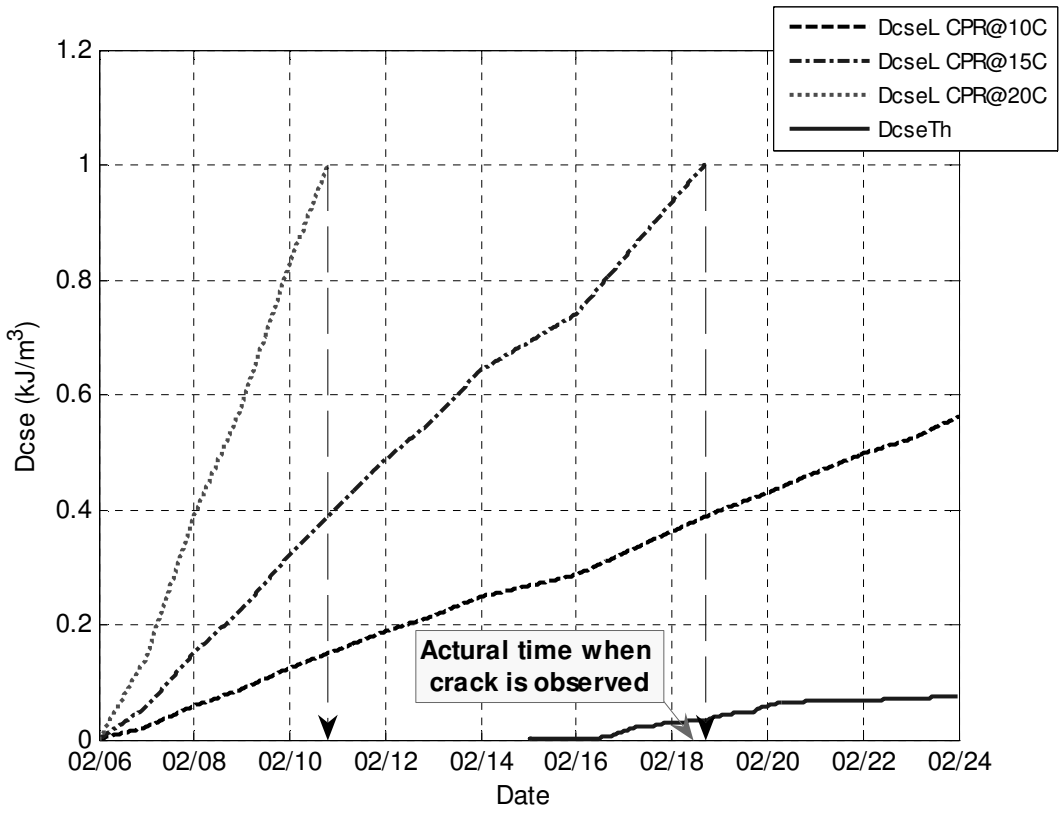


Fig 6.59 Effect on average temperature on DCSE accumuation

The accumulation of DCSE due to HVS load versus time for section 1A is presented in Figure 6.60. These results show that accumulated DCSE due to longitudinal stress along wheel path increases at a much faster rate than that due to transverse bending stress perpendicular to the wheel path. This indicates that transverse wheel path cracking is more likely to occur than longitudinal wheel path cracking for the HVS test conditions. In actual roadway environments, where rutted AC surfaces are common and the load

speed is much faster than the HVS, the principal tensile stress right at the tire edge is probably one of the main causes for longitudinal cracking.

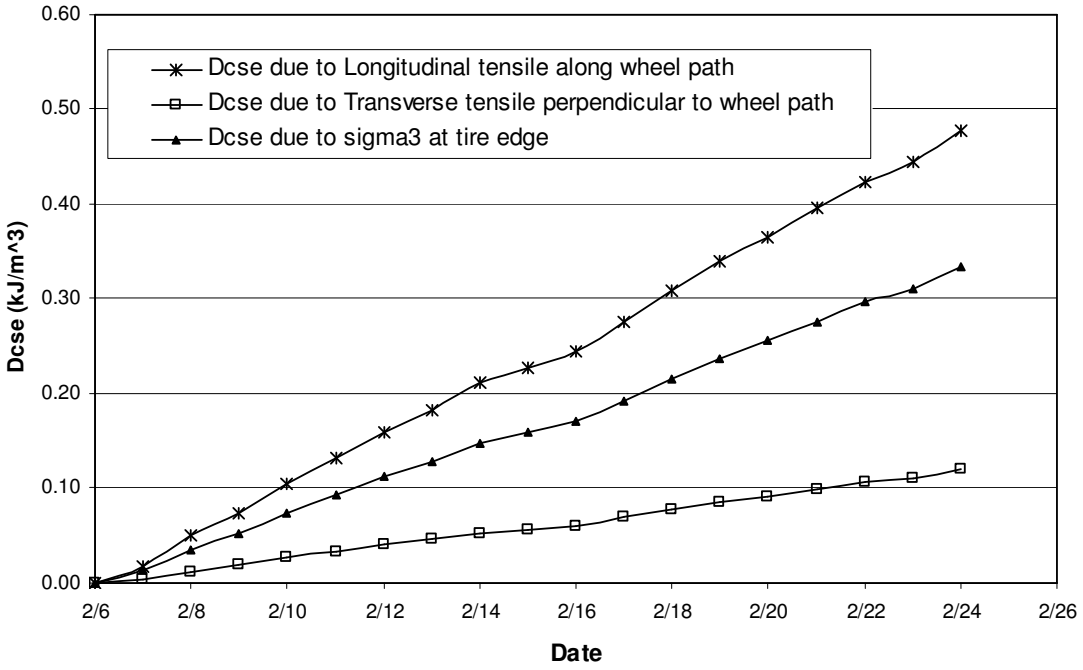


Figure 6.60. DCSE accumulation due to HVS load in Section 1A

### 6.4.2 Dissipated Creep Strain Energy (DCSE) due to thermal-associated stress

The approach for computation of dissipated creep strain energy (DCSE) due to thermal-associated stress was recently developed by Kim (2005), based on the thermal stress model developed by Hiltunen, Roque et al., (1993), and HMA Fracture Mechanics (Zhang et al., 2001 and Roque et al., 2002). The theories and the applications to this project are summarized below.

The model used here for thermal stress predictions within the asphalt layer was developed by Hiltunen, Roque et al. (1993) as part of the SHRP A-005 project. It is based

upon the following one-dimensional constitutive equation, which is Boltzmann's Superposition Principle for linear viscoelastic materials:

$$\sigma(\xi) = \int_0^{\xi} E(\xi - \xi') \frac{d\varepsilon}{d\xi'} d\xi' \qquad (6)$$

where: $\sigma(\xi)$ = stress at reduced time

$E(\xi - \xi')$ = relaxation modulus at reduced time $\xi - \xi'$

$\varepsilon$ = strain at reduced time $\xi (= \alpha(T(\xi') - T_0))$

$\alpha$ = linear coefficient of thermal contraction

$T(\xi')$ = pavement temperature at reduced time $\xi'$

$T_0$ = pavement temperature when $\sigma = 0$

$\xi'$ = variable of integration

The equation essentially models the asphalt layer as a uniaxial rod. The constitutive equation is written in terms of reduced time, $\xi$, because time-temperature superposition is being used to represent the creep compliance and relaxation modulus curves. The use of time-temperature superposition means that the asphalt mixture is modeled as a thermorheologically simple material. With a change of variables, the equation is written in terms of real time, *t*, as follows:

$$\sigma(t) = \int_0^{t} E(\xi(t) - \xi'(t)) \frac{d\varepsilon}{dt'} dt' \qquad (7)$$

Similarly,

$$\varepsilon(t) = \int_0^{t} D(\xi(t) - \xi'(t)) \frac{d\sigma}{dt'} dt' \qquad (8)$$

Using a Prony series representation of $E(\xi)$, the following finite difference solution to the above equation has been developed:

$$\sigma(t) = \sum_{i=1}^{N+1} \sigma_i(t) \qquad (9)$$

Where:

$$\sigma_i(t) = e^{-\Delta\xi/\lambda_i}\sigma_i(t-\Delta t) + \Delta\varepsilon E_i \frac{\lambda_i}{\Delta\xi}(1-e^{-\Delta\xi/\lambda_i})$$

$\Delta\varepsilon$ and $\Delta\xi$ are the changes in strain and reduced time, respectively, over time $t-\Delta t$ to $t$, $E_i$ and $\lambda_i$ are parameters for the Prony series representation of $E(\xi)$, and all other variables are as previously defined.

It should be noted that the use of a one-dimensional constitutive model was necessitated by the fact that stress predictions must be made at small time intervals over analysis periods of many years using a personal computer. Obviously, the stresses vary with depth due to a stiffness gradient within the layer and finite element modeling has confirmed this phenomenon.

In lieu of using a more sophisticated two or three-dimensional model, an approximate means has been developed to estimate this stress distribution using the one-dimensional model. Temperatures are measured or predicted at multiple depths (nodes) within the layer using the environmental effects model. Typically the nodes are located at 2-inch intervals. For each of these temperature nodes, stresses are predicted using the one dimensional model, thus establishing an approximate stress distribution with depth.

The temperature at the surface of Section 1A monitored at 5-minute intervals (between 02/15/07 00:00 and 02/24/07 00:00) is shown in Figure 6.61

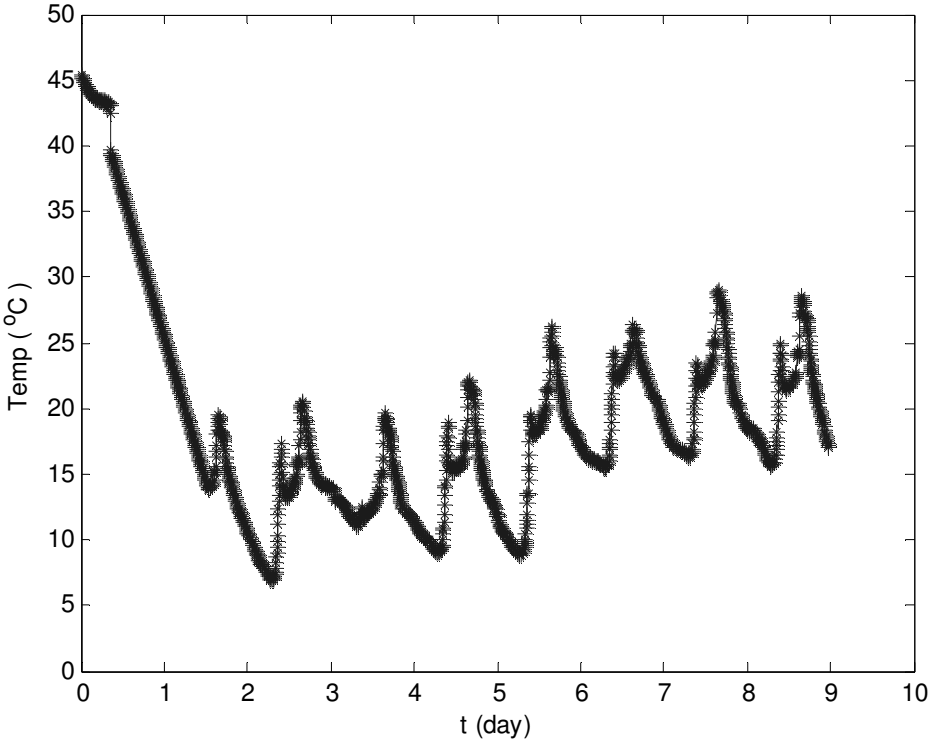


Figure 6.61. Surface temperature (02/15/07 00:00 To 02/24/07 00:00) at Section 1A from Site Monitoring

According to the record, the temperature reached the lowest value of this period (6.92 $^{o}$C) in the morning of February 17. The creep compliance values at 0, 10 and 20 $^{o}$C obtained from SuperPave IDT creep tests are shown in Table 6.8. They were adopted to compute shift factors and Prony Series coefficients, which were used together with the temperature data to predict thermal stress. The coefficient of thermal contraction was assumed to be 2.5E-6 1/$^{o}$C in this study.

The resulting thermal stress during the nine-day monitoring period is given in Figure 6.62. The maximum thermal stress of 31.9 psi occurred in the morning of Feb.17, corresponding to the lowest temperature recorded. As expected the overall thermal stress during the period is not high because the maximum temperature drop is less than 15 $^{o}$C within the temperature range of 0 to 20 $^{o}$C.

Table 6.8. Creep compliance from IDT test in section 1A

| Creep Compliance (1/psi) | | | |
|---|---|---|---|
| Time (sec.) | 0°C | 10°C | 20°C |
| 1 | 3.73E-07 | 4.76E-07 | 8.90E-07 |
| 2 | 4.07E-07 | 5.18E-07 | 1.05E-06 |
| 5 | 3.93E-07 | 5.80E-07 | 1.17E-06 |
| 10 | 4.07E-07 | 6.62E-07 | 1.35E-06 |
| 20 | 4.49E-07 | 7.87E-07 | 1.81E-06 |
| 50 | 5.87E-07 | 8.69E-07 | 2.26E-06 |
| 100 | 6.35E-07 | 1.02E-06 | 2.93E-06 |
| 200 | 6.56E-07 | 1.21E-06 | 4.12E-06 |
| 500 | 7.52E-07 | 1.64E-06 | 6.02E-06 |
| 1000 | 7.59E-07 | 1.95E-06 | 8.06E-06 |

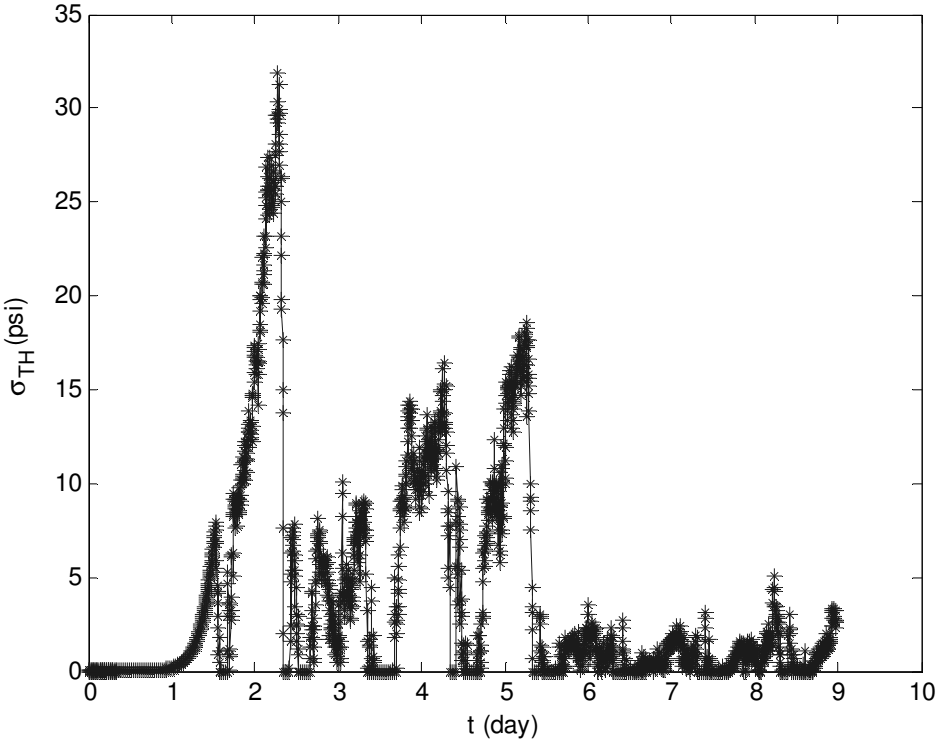


Figure 6.62 Thermal stress in Section 1A From 02/15 To 02/24/07 00:00 (at 5-min interval)

A thermal DCSE calculation procedure was developed by Kim (2005) in the development of HMA thermal fracture model. As the first step, the thermal creep strain equation was constructed with the substitution of creep compliance function in equation

(3) by only the viscous component representing the rate of damage of a viscoelastic media, i.e. $D[\xi(t)] = \xi(t)/\eta$ (10)

Following several steps of derivation, the resulting thermal creep strain can be shown as

$$\varepsilon_{cr}(t) = \varepsilon_{cr}(t-\Delta t) + \frac{1}{\eta}\left[\xi(t)\sigma(t) - \xi(t-\Delta t)\sigma(t-\Delta t) - \frac{\sigma(t)-\sigma(t-\Delta t)}{\Delta t}\int_{t-\Delta t}^{t}\xi(t')dt'\right] \quad (11)$$

The above equation can be solved using a finite difference procedure similar to that used in the thermal stress prediction.

Once the thermal stress and thermal creep strain are known, the thermal DCSE at each time step can be obtained based on the stress-strain relationship. For a small time increment Δt, the incremental thermal DCSE has the following form:

$$DCSE(\Delta t) = [\sigma(t) + \sigma(t-\Delta t)]\cdot[\varepsilon_{cr}(t) - \varepsilon_{cr}(t-\Delta t)]/2 \quad (12)$$

The thermal DCSE accumulation in Section 1A during the 9-day period (starting from 02/15/07 00:00) is shown in Figure 6.63. It is clear that the rate of thermal DCSE accumulation is corresponding to the rate of thermal stress increase, i.e., DCSE accumulation is at a high rate when thermal stress is building-up quickly.

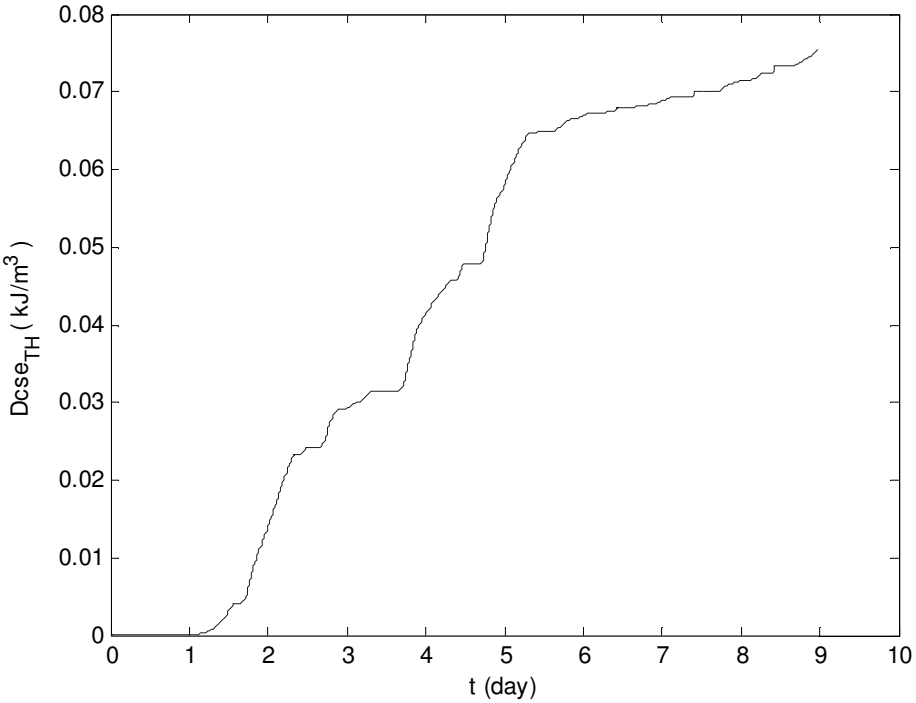


Figure 6.63. Thermal DCSE in Sec.1A From 02/15 To 02/24/07 00:00 (at 5-min interval)

### 6.4.3 Combined DCSE and crack initiation

The load DCSE and thermal DCSE were combined to represent the amount of micro-damage in the HMA material. According to HMA fracture mechanics (Zhang et al., 2001 and Roque et al., 2002), crack initiation (or growth) will occur once the accumulated DCSE exceeds a threshold. For generalized loading condition, the DCSE limit has been identified as a suitable threshold for crack initiation (and propagation as well). It can be determined from SuperPave IDT resilient modulus and tensile strength tests (Roque et al., 1997).

The combined DCSE, together with Load DCSE (at critical location) and Thermal DCSE versus time at Section 1A are shown in Figure 6.64. The magnitude of combined DCSE by the end of Feb.18 was 0.42 kJ/m$^3$. This value is about half of the average DCSE limit obtained from SuperPave IDT tests for Section 1A. Due to variance of properties in a real pavement surface, it is likely that certain weak locations with low DCSE limit

around 0.5 kJ/m$^3$ do exist. Therefore, it is believed the theoretical approach adopted here has provided a reasonable prediction on the time of crack initiation.

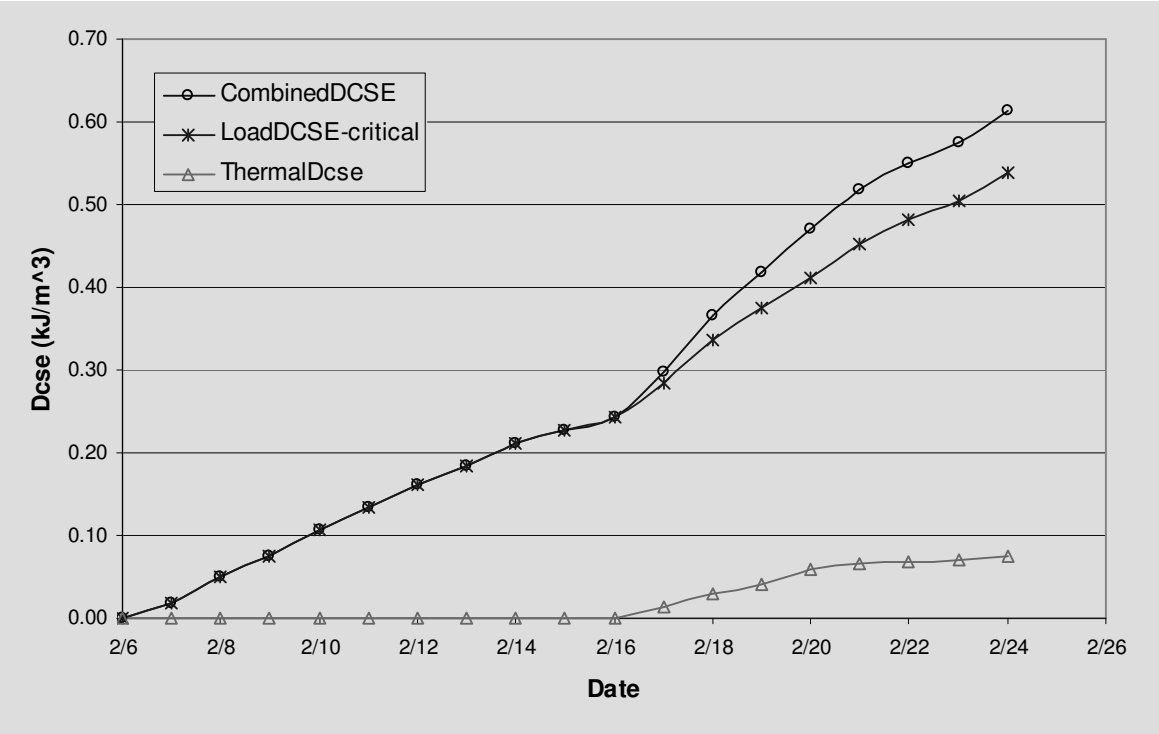


Figure 6.64. Accumulation of combined DCSE at Section 1A of HVS tests

The main findings from this analysis can be summarized as follows:

- Load induced stress had much more effect on crack initiation than thermal stress in section 1A.
- Transverse crack is more likely to occur than longitudinal crack under the given test conditions, which agreed with observations.
- The occurrence of longitudinal crack would require consideration of the effect of non-uniform contact and perhaps a faster speed of loading.
- Our model resulted in reasonable prediction of time (load cycles) to initiate cracking.

# CHAPTER 7
# CLOSURE

## 7.1 Conclusions

The following conclusions were derived from the findings of this study:

- APAS equipment is able to create substantial aging, and it is also considered proven that the procedure used creates and maintains an aging gradient over the asphalt thickness.
- According to the lessons learned from the aging experiment in Sections 1C, 1B, and 1A; between two and three day heating cycles resulted in aging levels comparable to those observed in 10 to 20 year-old pavements in Florida. This is consistent with the Superpave LTOA protocol which uses 5 days of heating at 85˚C to achieve aging levels comparable to 5 to 10 years in the field.
- Mixture properties of pavements subjected to extensive aging with the APAS did not result in reduction in tensile failure limits (e.g. fracture energy) consistent with field observations. This implies that factors others than oxidative aging and binder stiffening affect the failure of field pavements but are not replicated by APAS aging (or LTOA). For example, the effects of moisture, contaminant debris, and loads on micro-damage; healing and other effects that occur over long periods of time may play a significant role in reducing fracture energy in the field. However, these effects are clearly not in play when subjecting the pavement to heating alone.

- Properties determined from both FWD and Superpave IDT tests resulted in excellent predictions of stresses, strains, and energies due to applied wheel loads. This implies that our model's predictions of stresses and energies are also good.
- Strains measured using gages epoxied to the surface of the pavement are excellent tools for pavement load response measurement, but are not good indicators of damage development in the asphalt pavement.
- Test results indirectly validated the concept that a critical condition that exceeds the energy limits of the mixture is required to cause cracking, which is the basic premise of the HMA fracture model established by earlier FDOT research.
- Reasonable predictions of number of cycles to cracking were obtained using HMA fracture mechanics with mixture properties from Superpave IDT tests performed on cores from section 1A. These results indicated that there must be significant differences between loading conditions in the field, where top down cracks are generally longitudinal, and the loading condition applied in this HVS experiment.
- Impact-echo, SASW, and electrical resistivity methods do have potential for crack and damage detection but additional work is required to optimize these systems for this purpose.

## 7.2 Recommendations

Research should continue to further develop and refine the following areas:

- Evaluation of the effects of a rutted pavement surface on near surface stress distribution indicated that tire contact on a rutted pavement surface results in critical transverse stresses that would explain longitudinal cracking. This effect

was more pronounced for dual tires than for super-single tires. Therefore it is recommended that loading conditions for HVS testing be modified such that tires contact the pavement in a manner similar to the field where the pavement surface is not typically level. This may be achieved in one of two ways:

a) Tilt the HVS so the load is not applied along a path normal to the pavement surface.

b) Create a non-level surface by pre-loading the pavement to consolidate a portion of the cross section.

- A cooling unit is recommended to maintain higher stresses and minimize healing potential of the mixture.

# LIST OF REFERENCES

Roque, Reynaldo; Birgisson, Bjorn; Kim, Sungho; Guarin, Alvaro; "Development of mix design guidelines for improved performance of asphalt mixtures" Florida Department of Transportation Contract No.: BD545 (RPWO#16), Gainesville, Florida, 2005

Buttlar WG, Roque R. 1994. Development and Evaluation of the Strategic Highway Research Program (SHRP) Measurement and Analysis System for Indirect Tensile Testing at Low Temperature. *Transportation Research Record 1454*, pp. 163-171.

Jaeseung Kim. 2005. "Accurate Determination of Dissipated Creep Strain Energy and its Effect on Load- and Temperature-induced Cracking of Asphalt Pavement." Ph.D. dissertation, Department of Civil Engineering, University of Florida.

Hiltunen, D. R. and Roque, R. 1994. A mechanics-based prediction model for thermal cracking of asphaltic concrete pavements. *Journal of the Association of Asphalt Paving Technologists*, vol. 63, p. 81-117.

Z. Zhang, R. Roque, B. Birgisson, and B. Sangpetngam. 2001. Identification and Verification of a Suitable Crack Growth Law. *Journal of the Association of Asphalt Paving Technologists*, vol. 70, p. 206-241.

R. Roque, B. Birgisson, B. Sangpetngam and Z. Zhang. 2002. Hot Mix Asphalt Fracture Mechanics: A Fundamental Crack Growth Law for Asphalt Mixtures. *Journal of the Association of Asphalt Paving Technologists*, vol. 71, p. 816-828.

Roque, R., W. G. Buttlar, BE. Ruth, M. Tia, S. W. Dickison and B. Reid. Evaluation of SHRP Indirect Tension Tester to Mitigate Cracking in Asphalt Pavements and Overlays. Final Report to the Florida Department of Transportation, August 1997, 346p.

Lytton, R. L., J. Uzan, E. G. Fernando, R. Roque, D. Hiltunen, and S. Stoffels, "Development and Validation of Performance Prediction Models and Specifications for Asphalt Binders and Paving Mixtures," Report SHRP-A-357, Washington D.C.: Strategic Highway Research Program, National Research Council,1993.

Buttlar, W. G., and R. Roque, "Development and Evaluation of the Strategic Highway Research Program Measurement and Analysis System for Indirect Tensile Testing at Low Temperature," Transportation Research Record No. 1454: Asphalt Concrete Mixture Design and Performance, Washington, D.C.: National Academy Press, 1994, pp. 163-171.

Joh, S.H. 1992. User's guide to WinSASW, a program for data reduction and analysis of SASW measurements. The University of Texas at Austin, Austin, Tex.

Joh, S.H. 1996. Advances in interpretation and analysis techniques for spectral-analysis-of-surface-waves (SASW) measurements. Ph.D. Dissertation, The University of Texas at Austin, Austin, Tex.

L.A. Myers, R. Roque, and B. Ruth, "Mechanisms of Surface-Initiated Longitudinal Wheel Path Cracks in High-Type Bituminous Pavements," *Journal of the Asphalt Paving Technologists*, vol. 67 (1998), 401-432.

M. DeBeer, C. Fisher, and F.J. Jooste, "Determination of Pneumatic Tyre/Pavement Interface Contacts Stresses Under Moving Loads and Some Effects on Pavements with Thin Asphalt Surfacing Layers," *Proceeding of the 8th International Conference on Asphalt Pavements*, vol. 1 (1997), 179-227.

De Beer M, Groenendijk J., Fisher C., (1996).Three-Dimensional Contact Stresses under the LINTRACK Wide Base Single Tyres, measured with the Vehicle-Road Pressure Transducer Array (VRSPTA) System in South Africa, Confidential Contract Report CR-961056, July, 1996.

De Beer, M., Kannemeyer, L. and Fisher, C. 1999. Towards improved mechanistic design of thin asphalt layer surfacings based on actual type/pavement contact stress-in-motion data in South Africa. Seventh Conference on Asphalt Pavements for Southern Africa, 1999.

Drakos, C., R. Roque, and B. Birgisson, "Effects of Measured Tire Contact Stresses on Near Surface Rutting," Transportation Research Record No. 1764, Transportation Research Board, Washington, DC, 2001, pp. 59-69.

Bush, A. J., III, and Alexander, D. R. (1985). ''Pavement evaluation using deflection basin measurements and layered theory.'' Transportation Research Record 1022, Transportation Research Board, Washington,D.C.

Roque, R., Romero, P., and Hiltunen, D. R.(1997). ''The use of linear elastic analysis to predict the nonlinear response of pavements.'' Proc., 7th Int. Conf. on Asphalt Pavements, 1–13.

Roque, R., Romero, P., Shen, X., and Ruth, B. (1992). ''Prediction by asphalt pavement structural layer moduli using optimized FWD configuration.'' J. Assoc. Asphalt Paving Technol., 64, 278–305.

Yusuf Mehta and Roque, R. "Evaluation of FWD Data for Determination of Layer Moduli of Pavements." Journal of Materials in Civil Engineering, Vol. 15, No. 1, February 1, 2003.